Spectral Wave Dissipation by Vegetation

A new frequency distributed dissipation model in SWAN

J. A. Ascencio Ascencio

TUDelft

Deltares

The front cover image, obtained from WWF, shows the leaves of seagrass, a crucial ecosystem for healthy seas and climate. Seagrass captures carbon 35 times faster than the tropical rainforest and absorbs 10% of the ocean's carbon each year even though they are only 0.2% of the sea bottom [WWF]. Aquatic vegetation is crucial for marine biodiversity by providing food and habitat. Also, it stabilizes sediments, maintains the water quality, supports local economies, and mitigates flood hazards by reducing the incoming wave energy. The modeling of wave components being damped and transformed through emergent and submerged vegetation is the core of the present thesis. Despite the benefits of these ecosystems, we have been losing them at high rates (e.g., a soccer field of seagrass every 30 minutes since 1980) [Waycott et al., 2009]. Improving the understanding, quantification, and modeling of nature's benefits could contribute to the protection and restoration of marine habitats.

Spectral Wave Dissipation by Vegetation

A new frequency distributed dissipation model in SWAN

by

J. A. Ascencio Ascencio

to obtain the degree of Master of Science
at the Delft University of Technology,
to be defended publicly on Friday July 17, 2020 at 15:00 h.

An electronic version of this thesis is available at http://repository.tudelft.nl/.

TUDelft

Preface

I have been passionate about the ocean and marine life my whole life. I discovered coastal engineering recently when working in other cities after my bachelor's degree. Professionals were studying the waves, their impact on the shoreline, and even shaping interventions that significantly impacted the ecosystem. I wanted to be one of them, and TU Delft was my first choice. I am incredibly grateful to CONACYT-FiiDEM by awarding me a scholarship that covered a large part of the tuition fee and living expenses. During this experience in The Netherlands, I have grown significantly as a professional and person.

For my thesis research, I was determined to study and contribute to Nature-based solutions. Coral reefs, seagrasses, and many more beautiful ecosystems protect our shorelines, host marine biodiversity, and store large amounts of carbon. Despite their immense social, economic, and environmental value, we are losing them at increasing rates. Improving our quantification of nature benefits will facilitate decision-makers to see that working with nature is our best option.

This thesis completes my master's degree in Hydraulic Engineering with a specialization in Coastal Engineering at the Delft University of Technology. In addition to my technical studies, I followed the Entrepreneurship Annotation because I firmly believe that innovation could create a huge positive impact. The target group of this report is students and professionals interested in wave modeling over vegetation. The report describes the physical processes between waves and vegetation, and how dissipation models capture them in SWAN. During these last nine months, I have worked hard, aiming to make a useful report. I hope this document makes the way into that objective. Enjoy reading.

All my committee supported me since the beginning of the project. They gave me the confidence to go outside of my comfort zone, were emphatic during the extra challenges related to the COVID-19 crisis, and provided me with excellent feedback during this journey. I want to thank them individually. Ad Reniers for believing in me and introducing the opportunity to work on wave dissipation by vegetation. Jacco Groeneweg for opening the doors and welcoming me to a company I admire: Deltares. Niels Jacobsen for the weekly conversations, where he pushed me to grow professionally and helped me to solve essential pieces of the puzzle. Vincent Vuik for all the discussions on the field measurements and recommendations. And Marcel Zijlema for the fruitful conversations about the SWAN code and settings of the models. The achievements of all of you have been an inspiration towards giving my best in this project. An honor to have worked with you in this project. Also, I want to thank other members of TU Delft, who encouraged me with their passion and provided counseling during these years.

My friends have been an essential part of my life and a great energy source. My entrepreneurship friend Daniel for supporting my dreams to boost nature-based solutions. My volleyball friends from 'Punch', who always helped to restart my mind after a day of work. Mexidelftianos for the dinners and awesome support. My friends from Guadalajara who has been always there despite the distance and time difference. My friends from Cancun for introducing me to the awesome world of coastal engineering. Latitud members and friends after an intense year of working. The 'Familyship' for being a family after so many years. My TU Delft friends with which I shared study time at the library and beers afterward. Finally, all other friends with which I have crossed paths and that make life even better. Special thanks to my friends that welcomed me in their house for regular and special dinners like Christmas and New Years, when I was far from home.

Finalmente, quiero dedicar este logro y agradecer con todo mi corazón a mi familia. Gracias papá y mamá por el apoyo incondicional, creer en mis metas, y transmitir fuerza cuando sacrificios fueron necesarios. Las llamadas recurrentes y palabras de aliento me dan energía para seguir luchando por mis objetivos. Sin ustedes, esto no hubiera sido posible. Gracias Sandy, Vale y Alvaro por hacerme sentir en casa con los mensajes y llamadas, y hacer inolvidables momentos cuando estuve de visita. Gracias padrinos, Nena y Mauricio, por estar pendientes y siempre mandar cariño a pesar de la distancia. Gracias a mis tíos, primos, y abuelas quienes siempre crean momentos felices cuando nos vemos. Espero pronto abrazarlos a todos.

Jaime Alejandro Ascencio Ascencio
Delft, July 2020

Contents

List of symbols

Symbol	Description	Units
α_n	Velocity attenuation factor from Jadhav et al. [2013]	-
α_u	Velocity (in-canopy) reduction factor from Jacobsen et al. [2019]	-
α_v	Dissipation reduction factor	-
a	Wave amplitude (1/2 H)	m
A_b	Near bottom excursion amplitude	m
b_v	Stem thickness (diameter)	m
C_b	Bed friction coefficient	-
C_f = [cfw]	Collins friction coefficient	-
C_D = [CD]	Drag coefficient	-
DBM	Vegetation dry bio-mass	g / m^2
ε_v	Time-averaged rate of dissipation by vegetation	kg / s^3
E_{tot}	Total variance density	m^2
$E(f)$	Variance density 1D spectrum (= S_n)	m^2 s
$E(\sigma,\theta)$	Variance density 2D spectrum	m^2 s
f	Frequency = 1 / T	1 / s (= Hz)
f_p	Peak frequency	1 / s
f_w	Madsen friction coefficient	-
F_x	Horizontal canopy drag force	kg / (m^2 s^2)
g	Gravitational acceleration	m^2 / s
γ	Peak enhancement factor JONSWAP spectra	-
$h = d$	Water depth	m
$h_v = \alpha h$	Vegetation (or canopy) height	m
h_v/d	Vegetation relative submergence	-
H	Wave height	m
H_{m0}	Significant wave height	m
H_{rms}	Root mean square wave height	m
k	Wave number	rad / m
$\widetilde{k}$	Mean wave number	rad / m
k_p	Wave number at f_p	rad / m
k_N = [kn]	Nikuradse bottom roughness length	m

KC	Keulegan-Carpenter number	-
$m_{u,0}$	Zeroth moment of S_u	m^2 / s^2
$N(\sigma,\theta)$	Action density spectrum	m^2
N_{Ursell}	Ursell number	-
N_v	Vegetation density	stems / m^2
L	Wave length	m
Q	Modified Keulegan Carpenter number	-
ρ	Water density	kg / m^3
σ	Intrinsic wave frequency	rad / s
$\tilde{\sigma}$	Mean intrinsic wave frequency	rad / s
σ_p	Intrinsic wave frequency at peak frequenc	rad / s
$S_{ds,bot}$	Bottom friction energy source term	m^2 s
S_n	Surface elevation spectrum (= $E(f)$)	m^2 s
S_{tot}	Energy source tem	m^2 s
S_u	Velocity spectrum	m^2 / s
T_m	Mean wave period	s
T_p	Period at f_p	s
θ	Wave directions	°
u	Orbital velocity	m / s
u_{rms}	Root mean square of bottom orbital motion	m / s
V_f	Flexible vegetation factor (for effective length)	-
ω	Radian frequency	rad / s

Abstract

Climate change puts under pressure existing and future coastal interventions. Growing threats like sea-level rise and intensity of storms require solutions to be adaptable and resilient. Nature-based solutions have shown to tackle these challenges while providing social, environmental, and economic benefits. The role of vegetation in coastal protection is increasingly recognized. Aquatic vegetation reduces erosion, storm surge, and incoming wave height. Vegetation alone or in combination with engineered structures have proven to be cost-effective coastal defenses.

Large-scale modeling of waves with spectral wave models such as SWAN is indispensable for the design of coastal structures and the assessment of flood risk. Wave dissipation due to vegetation can be modeled in SWAN as increased bottom friction (implicit modeling) or as an additional dissipation function (explicit modeling). The second assumes that vegetation can be represented as rigid cylinders or plates (canopies) with different properties. While some studies concluded that implicit modeling reproduces the spectral evolution of field measurements more closely, others concluded the opposite.

Within the BE-SAFE project, field campaigns measured the spectral energy distribution over salt marshes in the Dutch Wadden Sea during several winter storms. The vegetated foreshore in front of the coastal dike got submerged over 2 m of water during high tide and storm surge. The measurements deployed wave gauges over the study transect, which was defined between the pioneer zone marsh edge and the near-dike location (300 m behind the salt marsh). Calibrating the implicit and explicit models in SWAN brought the modeled total wave energy decay closer to the measurement. Nevertheless, the spectral shape, which describes the energy distribution over frequencies, still showed significant and not yet understood differences near the dike.

A methodology was executed to investigate the mechanisms that could reduce the spectral mismatch between the SWAN wave model and measurements over vegetation. First, the literature highlighted possible mechanisms that could be incorporated for this purpose. Next, a new frequency-distributed explicit dissipation model of Jacobsen et al. [2019] was implemented in SWAN and compared to implicit and explicit models using lab and field measurements.

The results showed that the newly implemented model accurately captures the physics and the change of spectral shapes for all experimentally tested wave conditions and submergences. In contrast, the existing implicit and explicit dissipation models in SWAN reproduce the spectral evolution only under certain circumstances. In the validation and comparison to the field measurements with a much larger water depth than the vegetation height, the model of Jacobsen et al. [2019] correctly captured the vegetation's physical representation and the dissipation on the wind-sea frequencies. Nevertheless, the amount of energy on low frequencies was largely underpredicted by all frequency-distributed models. Therefore, the model of Jacobsen et al. [2019] was modified to include flexibility in a frequency-dependent reduction factor that reproduced the energy decay of the measurements in all frequency regions. Other mechanisms that could be responsible for the mismatch before and over the marsh are the redistribution of energy by non-linear triad interactions, generation of infra-gravity waves, and near-shore currents caused by horizontal variations on the vegetation properties.

The present research provides the range of conditions in which the tested explicit and implicit energy dissipation functions in SWAN are able to simulate the spectral evolution over rigid canopies and flexible salt-marsh vegetation. A new version of SWAN includes a new frequency-distributed explicit model that performed more accurately than existing models for rigid canopies. The physical insights from the research contributed to developing additional versions of SWAN, which performed closely to the energy distribution of the measurements over deeply submerged and flexible salt marsh vegetation species.

1

Introduction

Increasing frequency and intensity of hazards such as storms and sea-level rise have been predicted due to climate change [Knutson et al., 2019], requiring a resilient and upgrading coastal protection. Hard and grey solutions such as dikes and seawalls reduce the flood risk. Nevertheless, uncertainties about future scenarios increase the probabilities of failure and the costs of these interventions. The design, construction, and maintenance should be cost-effective. For this, an intervention must adapt to growing threats like climate change. Besides, traditional solutions have unforeseen negative impacts on local and large scale systems [Borsje et al., 2011]. On the other hand, Nature-Based Solutions (NBS) attention and momentum has been increasing due to their additional contribution to reach environmental, societal, and climate objectives. For example, submerged vegetation (like seagrasses) are often referred to as Blue Forest due to their significant contribution in carbon storage.
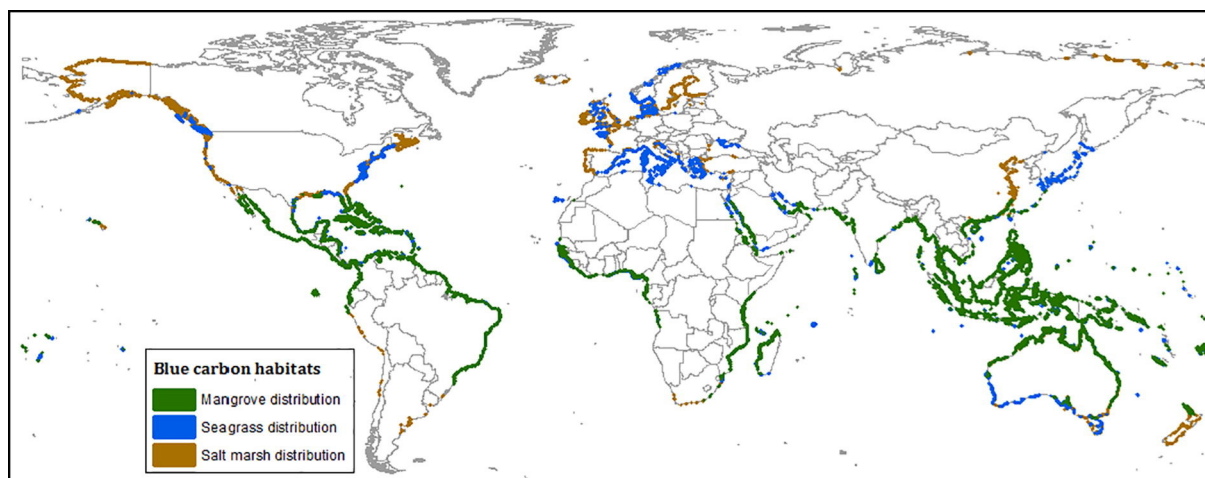

Figure 1.1: Global Distribution of seagrass, salt marsh and mangrove habitats. (From ?)

Aquatic vegetation occupies a significant part of the global coastlines, rivers, and lakes. These vegetated habitats include some of the most productive ecosystems in the world, like salt marshes, mangroves, and seagrasses. Despite their value and extension, we have lost 50% of salt marshes, 35% of mangroves, and 29% of seagrasses during the last 20-50 years [Barbier, 2011]. The known global distribution of these ecosystems is displayed in Figure 1.1. According to data collected by Himes-Cornell et al. [2018], the regions with the most significant distribution by extension per ecosystem are Europe with 46.5% of salt marshes, North America with 69.6% of seagrasses, and Central and South America with 26.1% of mangroves. The global presence of vegetation and their effect on the hydrodynamics already makes them an important consideration for the coastal engineering community.

The benefits that nature provides to humans are known as ecosystem services. These are valued in economic terms to provide information to decision-makers that could change the conservation, restoration, or

enhancement of these ecosystems. Eco-services are divided into four categories according to Kumar [2010]: Provisioning (e.g., food, water, and raw materials), Regulating (e.g., air and water quality, climate regulation, natural hazard regulation), Habitat (e.g., fish nurseries, primary production), and Cultural (e.g., recreation, eco-tourism). In the hydraulic engineering community, the importance of the vegetation regulating services for shoreline protection and sediment retention has been widely acknowledged (e.g. Costanza et al., 2008, Borsje et al., 2011, Gedan et al., 2011). As described in Fig 1.2, vegetation in foreshores acts as a natural coastal defense, reducing the risk and damages from flooding and erosion. If these natural barriers are removed where existent, damages to low-lying areas will increase. Recent studies have determined the economic feasibility of these ecosystems, concluding that vegetation can pay itself as coastal protection [Cruz, 2020]. Nevertheless, the uncertainty around the quantitative benefits of these complex environments remains, particularly in large scale (time and spatial) applications [Bouma et al., 2014].

Figure 1.2: Impact of storm surge on coastal infrastructure and people with and without vegetated foreshores. (From Cruz, 2020)

1.1. Problem Description

The simplification and reproduction of the interaction between these natural elements with their system are referred to as models. These tools allow the scientific and engineering community to understand the importance of different processes and provide predictions for future scenarios. Nowadays, computational models are practical tools to evaluate interventions in the coastal zone. Their use has been increasing together with computational power and accessibility. The existing differences between the computational models' output and measurements, hereafter named as a mismatch, could be reduced if additional processes are also included in existing models. Present technological developments could cope with increasing complexity while remaining practical engineering tools, providing a window of opportunity to improve our modeling accuracy and capabilities.

Wave dissipation over vegetation has been measured at numerous locations all over the world (Table 2.2), providing insight into the physical process and validation material for models. Wave dissipation due to vegetation can be modeled as bottom friction (implicit modeling) or as an additional dissipation function (explicit modeling). The second assumes that vegetation can be represented as cylinders or plates (canopies) with different properties. The dissipation mechanisms behind these two approaches are described below.

Vegetation Modeling	Dissipation mechanism	Input variables
Implicit Modeling	Bottom friction	Bottom roughness length
Explicit Modeling	Rigid cylinders drag	Stem height, diameter, density, and drag coefficient.

Table 1.1: Types of vegetation schematization for wave modeling in SWAN with the dissipation mechanism represented in the formulation and the input variables used to implement the stem characteristics.

Previous studies have already developed formulations to quantify the overall decay in total wave height across vegetation with good results, some of them empirically (e.g., Yin et al., 2017 , He et al., 2019) and others analytically (e.g., Dalrymple et al., 1984, Kobayashi et al., 1993, Mendez and Losada, 2004, Chen and Zhao, 2012, Losada et al., 2016). Very few studies have focused on the wave energy distribution across frequencies (Lowe et al., 2007, Jadhav et al., 2013, Nowacki et al., 2017). Some developed formulations, like Mendez and Losada [2004], have been implemented in phase averaged (SWAN) and phase-resolving numerical models for wave propagation. Besides, numerous studies have focused on low energy environments [Anderson et al., 2011], while the application for flood safety focuses on extremes [Vuik et al., 2016]. This has resulted in large scale coastal models that, if calibrated properly, can reproduce the overall energy total decay but not the physical processes that may affect different wave components of the spectra.

SWAN is a widely used model for large scale coastal applications. It is described as a third-generation computational model for coastal regions capable of computing the generation, transformation, and dissipation of short crested random waves [Booij et al., 1999]. SWAN is a phase-averaged model in continuous development by the Delft University of Technology and other partners like Deltares. The worldwide use of this tool as a stand-alone model or as Delft3D suite [Deltares, 2014] has converted it in one of the most important large scale computational models for coastal regions. As an important computational model in the coastal engineering community, vegetation modeling is included implicitly and explicitly. The explicit dissipation model implementation has been validated against experimental and field data [Suzuki et al., 2011]. Other studies have also compared the performance of implicit models to the explicit formulation using field measurements (Nowacki et al., 2017 and Baron-Hyppolite et al., 2019).

The model SWAN is used in The Netherlands to assess flooding safety and evaluate the effectiveness of possible implementations. Within the *BE-SAFE* project (Bio-Engineering for safety using vegetated foreshores) and the *"POV Waddenzeedijken HR Effectiviteit Voorlanden"* project, wave measurements over salt marshes were carried out during several storms in The Netherlands (e.g., Vuik et al., 2016, Vuik et al., 2019). Both programs investigate the effectivity of vegetated foreshores in providing coastal protection, especially in front of existing barriers as dikes. In front of the coasts from Friesland and Groningen, implicit and explicit model outputs from SWAN showed significant and not yet understood differences when looking at the measured spectral energy distribution [Steetzel et al., 2018]. An example of this mismatch is shared in Figure 1.3.
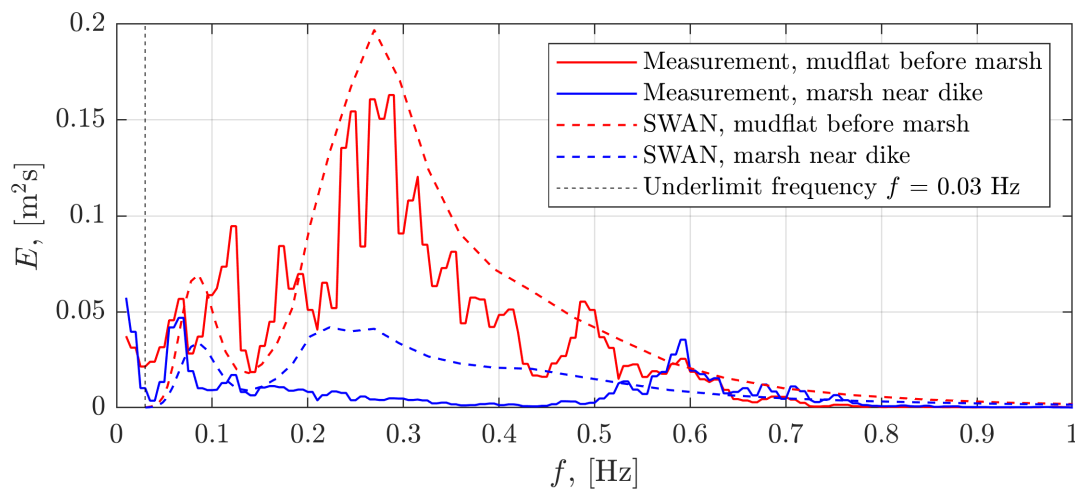

Figure 1.3: Example of mismatch between measured and explicit modelled wave spectra with SWAN over a submerged salt marsh during a winter storm in 2015 at Groningen, The Netherlands. (Made with data from Steetzel et al., 2018)

The field campaign from Figure 1.3 collected wave data at the site of study, located west of Eemshaven in Groningen, The Netherlands [Zhu et al., 2020b] during the winters of 2015 and 2017. Two storms with significant surge (an increase of water level by storm effects) were captured with the deployed wave gauges. These measurements were compared to computed values coming from the transformation of offshore wave data to the site with SWAN. Information related to wind speeds, water levels, and currents was provided to the model for specific moments of the storm. During these events, the water level experienced a level increase

of more than 3 m, covering the marshes zone with water and storm waves, which were able to reach the dike over more than 1 m of clear submergence. If the differences between measurements at the edge of the salt marsh (red) and the dike (blue) are observed in Figure 1.3, it is clear that a dissipation mechanism is missing to reduce the energy around the peak frequency and that energy on low and high frequencies should be conserved. Explicit and implicit dissipation models available in SWAN were tested, and none could reproduce the spectra's qualitative evolution at the measurement near the dike. More information and analysis around this case are explained in Chapter 5.

Moreover, this spectral behavior was not found in other measurements from the *BE-SAFE* project in the Western Scheldt [Vuik et al., 2016]. Dense vegetation (dominant in the overall dissipation) in the Western Scheldt, versus low, patchy and highly flexible vegetation in the Wadden Sea (adding importance to other mechanisms and their interaction) could explain part of the differences between the two sites. Hydraulic conditions also differ, the Western Scheldt can be represented by a 1D model with local waves while Groningen shows a 2D complex mix of waves generated in the Wadden Sea and the North Sea. Considering these factors could contribute towards an understanding of the physical processes that could drive the spectral mismatch with existing or recently developed dissipation models.

1.2. Research Framework

Recently, a new frequency-dependent explicit dissipation model for waves propagating over canopies was published [Jacobsen et al., 2019]. The development shows larger improvements when the vegetation is submerged, condition present during the storm of Figure 1.3. The objectives of the graduation project are to understand the mismatch of wave modeling over vegetation and to improve the presently available vegetation module in SWAN [Suzuki et al., 2011] by implementing the formulation of Jacobsen et al., 2019. In order to improve large scale modeling over vegetation and to understand if Figure 1.3 is an exceptional case due to physical processes or measurements, a research methodology was executed following the research question:

> *"What are the possible missing mechanisms in the dissipation function that could reduce the wave spectral mismatch between SWAN model outputs and (lab and field) measurements over vegetation?"*

The following sub-questions investigate the main research question objective:

1. *What are the spectral differences between the dissipation functions for vegetation in SWAN?*

   1.a. What are the performance differences between the explicit and implicit modeling approach if compared to the energy distribution of measurements?

   1.b. If implemented in SWAN, could the new model [Jacobsen et al., 2019] be an improvement for spectral wave modeling over vegetation?

2. *If the new model's possible improvements in the dissipation function are not the answer to the wave modeling over vegetation spectral mismatch, which other processes could be responsible, and what are the recommendations for further research?*

The research sub-questions imply specific tasks towards understanding and reaching the objectives behind the main research question. The first sub-question includes modifying the source code from SWAN to implement the new formulation. The implementation is verified by testing it with regular and irregular waves. Once implemented and tested, this new model performance is compared to explicit and implicit vegetation models in SWAN. For this purpose, a recent experimental campaign and field measurements are used. The model comparison to these data will help understand the differences between explicit and implicit modeling and the condition on which these increase. If a significant improvement by the new model implementation is shown, this could lead to a new version of the model for large scale coastal modeling. The second sub-question objective aims to broaden the picture in case the present vegetation functions are not the mismatch answer. More mechanisms and interactions are present in the field than in the experiments. Each modeling approach is based on different dissipation processes, the findings from previous studies, and their output will guide the possible missing mechanisms in the dissipation function of SWAN. The physical understanding gained through the project provides recommendations and direction towards further research on this line of research that will continue in the years to come.

The aim of the project is not only to improve our understanding of the shared topics but also to contribute to the practical modeling capabilities in the engineering community. Therefore, for large scale applications, some choices are made and explained during the project. This research only considers the range of wind-generated waves for coastal applications from all the frequencies and periods of the vertical motions of the ocean surface. The recommended spectral range for storms modeling starts in 0.03 Hz as recommended by the The SWAN team [2019a], and ends in observed practical limits between 1.0 and 2.0 Hz. The typical spatial scales for modeling waves approaching the coast are on the range of m to km with a resolution between 10 to 100 m. Nevertheless, the spatial and spectral resolution for the models' comparison in the implementation tests and experimental data validation was increased. This was done to capture small differences between the models at no high additional computational cost.

A methodology, hereafter explained, was implemented to approach the proposed research sub-questions. Initially, a literature review on the effect of vegetation to wave transformation was performed. During this phase, the existing dissipation functions to reproduce wave dissipation by vegetation in SWAN were consulted. Particular importance was set to understand the comparison and expected differences between the existing formulation by Suzuki et al. [2011] and the newly developed formula by Jacobsen et al. [2019]. With this base, the new formulation was implemented as a new subroutine in the coastal wave model SWAN. As described in Figure 1.4, this was an iterative process up until the end of the present document because applying the model to different settings or conditions revealed possible continuous improvements. In the present report, the last developed version based on Jacobsen et al. [2019] was used to update all the results and conclusions. If more than one version is used, it is mentioned otherwise. Suggestions are made at the end of the document for future research and improvements.
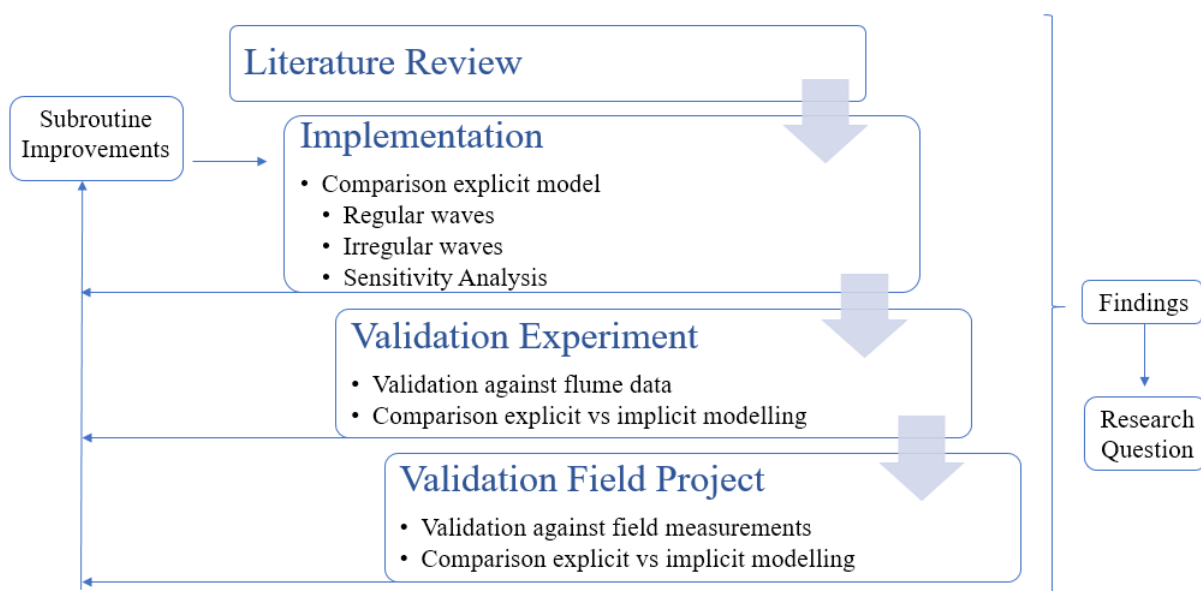

Figure 1.4: Interaction between the main components of the research methodology, subroutine development, and research question.

Once the model was successfully implemented, the new subroutine was compared to the previous explicit formulation using regular and irregular waves. From the variables during this analysis, physical and numerical parameters were changed to understand the differences between the models. The investigation involved modifying the vegetation height, water depth, wave periods, wave heights, and spectral shapes. A sensitivity analysis included in the Appendix investigated the effect of choices made during the model implementation in the SWAN's source code.

The experimental measurements were selected from other available data sets due to a broader range of frequencies and submergences that could help identify differences between the models. The field data used for the project comes from the campaign measurements of the example in Fig 1.3. From this field campaign, two large storms were recorded. The peak moment of each storm (where the largest water depths and wave heights were recorded) are used for the validation. The temporal and spatial scale of this data is on the range of hours and meters to kilometers.

Finally, the findings from these computational experiments and data comparison aim to provide a possible answer to the research question and sub-questions. The implemented model was tested under a wide range of conditions, resulting in a robust and stable computational model under the conditions of the present research. New versions with additional mechanisms like flexibility were tested to provide direction towards future research.

1.3. Outline

The outline of the report follows the described methodology and an increasing level of complexity. The report was written not only as an academic requirement but as a study useful for future research. Therefore, the extension of the document was designed to include the main findings for the academic discussion in a concise manner. The introduction to the present challenges and motivation for the present report are addressed in Chapter 1. Next, the theoretical background in Chapter 2 explains the existing research conclusions and knowledge gaps. Some of the most referred dissipation models in the literature (both implicit and explicit) are described and compared to the new formulation. Other processes that play a role in the spectral transformation over vegetation are also considered as possible answers for the mismatch.

In Chapter 3, the implementation procedure of the new formula in the wave model SWAN is included. Here, the assumptions and choices made during the implementation process are described and analyzed. In the same Chapter but section 3.2, a comparison of the actual explicit version of SWAN with the newly developed explicit subroutine is made. For this comparison, computational tests have been developed following a 1D representation with a constant slope. Both regular and irregular waves are tested in this phase. A sensitivity analysis with different vegetation and forcing conditions provides insight into the parameters that lead to more significant differences between the models. For further use of the newly developed model version, a brief user guide on how to activate the new subroutine is shared in Appendix A.

The validation with experimental measurements is performed in Chapters 4. The explicit and implicit models are compared to the wave flume experiments performed at the U.S. Army Engineer Research and Development Center from the *USACE* (U.S. Army Corps of Engineers). In this extensive campaign, both regular and irregular waves were studied over wooden dowels. For the present research in which spectral differences are investigated, only irregular waves are used. During the experimental validation, the first implicit and explicit vegetation modeling comparison is executed. Calibrating each case and model was required because the friction and drag coefficients depend on not only the physical characteristics of the object but also on the flow characteristics.

The validation with field measurements is described in Chapter 5. Data collected from the *BE-SAFE* and *POV Voorlanden* projects are used to study the performance of the models on field measurements. As the core of these measurements, two storms are used to validate and compare the models. In this last phase of the project and due to the site complexity, other wave mechanisms and interactions are also considered. To investigate if additional processes could reduce the spectral mismatch, these are integrated into new versions of the model and compared to both storm peaks. Finally, the findings and further recommendations are shared in Chapter 6. In this part of the report, a discussion over the obtained results takes place. As the core of the conclusion, the answers to the research question and sub-questions are included.

2

Theoretical background

This second chapter includes concepts from the literature study that could contribute to understanding and to possible help answering the research question. After briefly introducing the wave spectrum, an extensive list of studies that measured the interaction of waves and vegetations appear in section 2.2. Other relevant studies that investigate the topic, but that did not measure data themselves, are not enlisted but included in the discussion. The discussion encloses the main findings that could influence the answer to the research question. Some of them are the influence of vegetation flexibility and the velocity profile on the spectral distribution of energy. Important to mention is the need to understand the assumptions and neglected processes behind each model or experiment.

Next, the two approaches to represent vegetation in large scale modeling (explicit and implicit) are described. While explicit modeling includes physical properties of the stem (e.g., height and diameter), implicit modeling represents it as an increased bed roughness. Models from both approaches are available in SWAN. These are selected based on support from previous studies and then described. Next, the new formulation by Jacobsen et al. [2019] is introduced. The expected differences between the existing explicit model in SWAN and the newly implemented subroutine are highlighted to be a reference for the implementation validation in Chapter 3.

2.1. Wave Spectrum

The spectral mismatch is an essential concept of the present investigation and is caused by differences between measured and modeled wave spectrums. The wave spectrum represents the waves at one location at a specific moment in time. The waves in oceanic and coastal waters are disturbances on the interactive layer between the seawater and air (water surface). Different sources might cause the vertical motion on the water surface, but here we limit the discussion on wind-generated waves. As its name shows, wind waves receive energy from the wind, which holds a random character. Several researchers (e.g., Cavaleri and Rizzoli, 1981 Janssen, 1991) have studied the energy transfer from the wind to waves. The result is a random water surface with waves of different heights and lengths, traveling with diverse phases and directions.

The water surface can be decomposed with the Fourier series of the random-phase/amplitude model. In this model, the surface elevation is considered to be the sum of a large number of harmonic waves, as represented in Figure 2.1 (either in one or multiple directions). All these harmonic components can be assembled in the amplitude spectrum in which each frequency (horizontal axis) is assigned a discrete value of its amplitude (vertical axis). The variance ($\frac{1}{2} \overline{a_i^2}$) is more relevant than the amplitude (a_i) because the sum of each component's variance is equal to the variance of the sum of the components (and not valid for the amplitudes). Therefore, the variance replaces the amplitude. Because a continuous spectrum is present in nature, the energy of this discrete spectrum is filled first by distributing the variance over frequency intervals. Now, to make it continuous, we let the frequencies interval width to approach 0 ($\Delta f \rightarrow 0$), as shown in Figure 2.2. The result is the variance density spectrum hereafter named as the wave spectrum.

The waves at the ocean can keep growing if the wind is present, but other mechanisms avoid unrealistic huge waves to develop. An example of them is wave breaking, which at the ocean is determined by the wave
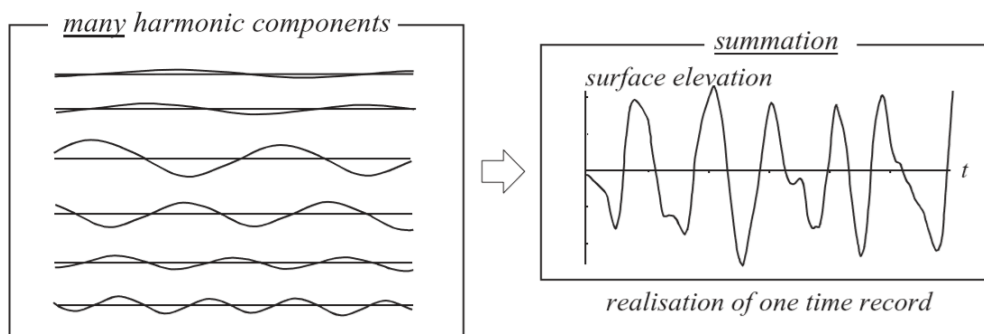
Figure 2.1: The random sea surface can be described as the summation of many harmonic (regular) waves, with constant but randomly chosen amplitudes and phases. (From Holthuijsen, 2007)
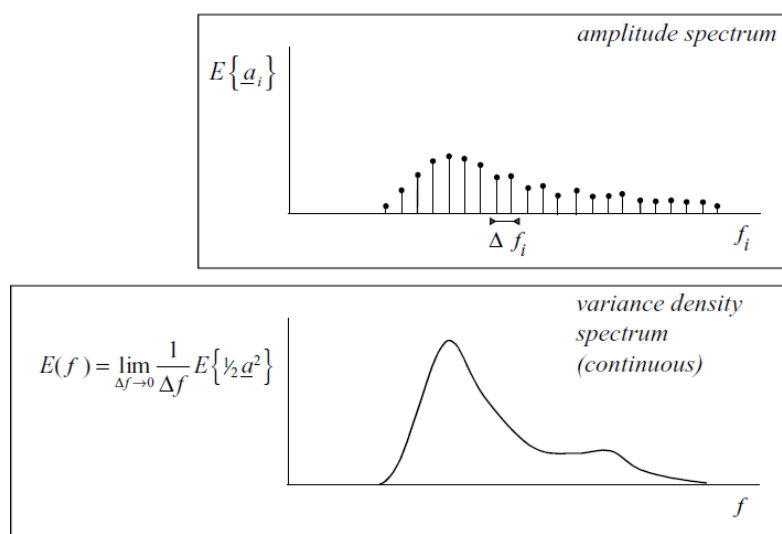

Figure 2.2: Use of the random-phase/amplitude model to describe waves at one location and moment on time into the discrete amplitude spectrum that is further transformed into the continuous variance density spectrum. (From Holthuijsen, 2007)

steepness (the ratio between wave height and length). A very steep wave will eventually be unstable, leading to the process known as white capping. This can be observed as the white foam on top of the ocean waves, allowing energy to be dissipated. Other mechanisms contributing to the evolution of the spectra on deep water are the non-linear interactions named quadruplets. Quadruplet interactions are caused by the resonance between two pairs of waves that transfer energy to lower or higher frequencies.

Eventually, waves at the ocean will reach a coastline. Other processes can play a role in the spectral transformation over shallower waters. The water regime is the concept used to determine if a wave component is present in deep, intermediate, or shallow water. The regime is subjective to each frequency component, and not equally to all the spectra's waves. While some very short waves will not be affected by a decrease in the water depth, longer waves (lower frequencies) will transform as the sea-bed changes. This is related to the orbital velocity of the waves, which are present at the water surface and under it. The velocity at which water particles rotate decreases exponentially on deep waters. The magnitude of this velocity is linked to the wave at the water surface. Longer waves make water particles move in longer diameters, reaching deeper waters than shorter waves. Some of the processes present on shallow waters are surf breaking, bottom friction, and non-linear triad interactions (similar to quadruplets but allowing now only two waves to interact and shift energy to higher frequencies).

Another process that influences many nearshore processes is the presence of infra-gravity (IG) waves. Two identified processes generate these. The first is the interaction of two wave trains with similar length and frequency, which will cause a group structure characterized by low frequencies. This mechanism can grow by receiving the energy of high frequencies in shallow waters due to near-resonance. The longer the wave prop-

agates over a gentle slope, the more energy that is transferred [de Bakker et al., 2016]. The second is related to the different breakpoints of the waves, in which larger waves break at deeper waters than smaller waves, resulting in variations of the radiation stress, set-up, and water level transferring energy at infra-gravity frequencies. The second mechanism is dominant in steeper slopes while the first on gentle foreshores [Battjes, 2004].
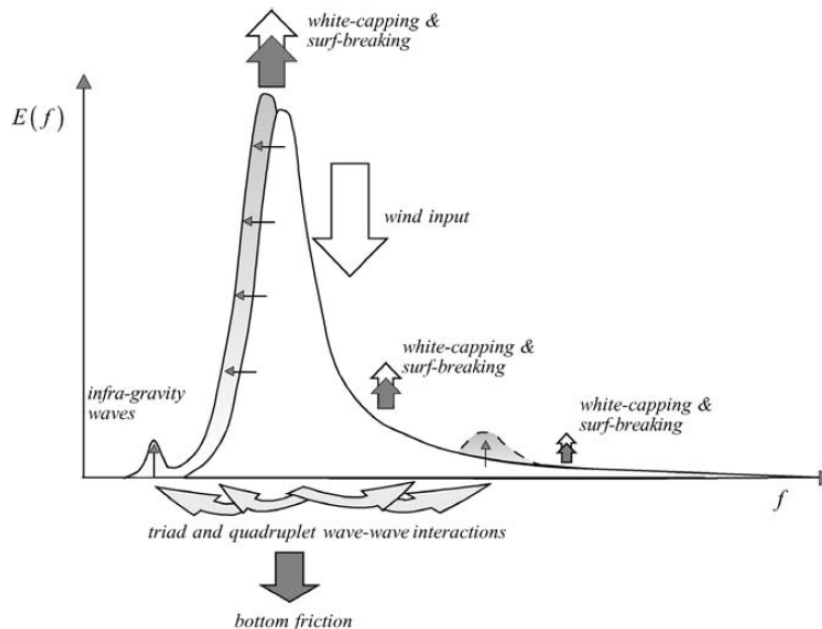

Figure 2.3: Flow of energy through different mechanisms in shallow waters, allowing changes on the spectral shape and/or the total amount of energy. (From Holthuijsen, 2007)

These and other processes affect differently the spectra as described in Figure 2.3. The magnitude and interaction of these mechanisms depend on the site (e.g., bathymetry) and the boundary conditions (e.g., wind, waves, currents), causing each wave spectrum to evolve differently. Even though the total amount of energy can be conserved in some cases, the distribution of energy might differ. The spectral mismatch is the difference between the energy distribution on a spectral comparison (usually a measurement and a model output). This is one of the core concepts of the present research.

2.2. Vegetation and Waves

The interaction between vegetation and waves has been studied in different parts of the world with different approaches. This line of research has been reported from publications of Keulegan [1958] with theoretical canopies studies over forces on cylinders, up until recently (e.g., van Rooijen et al., 2020, Zhu et al., 2020a). To provide an overview of most of the data generated and measured by studies related to wave dissipation by vegetation, summarizing Table 2.1 and 2.2 have been created. Information over the measurements is included in both tables. If the conditions were not found, the cell is kept without data. More studies over the interaction between vegetation and steady-flow have been identified but have not been included in the tables as they do not include waves.

Flume experiments help to isolate and simplify the mechanisms that are researched. Validating and understanding the individual processes of a complex situation is the first step in increasing the knowledge around it. Each campaign might have collected various water levels, wave conditions, interaction with currents, 3D effects, or others. Considering the specific information of each measurement contributes to following the reasoning behind certain conclusions. Consulting the references is further recommended if additional information is required over the experimental or field campaign.

The information in Table 2.1 is organized in columns. Initially, the author(s) and year of the reference are shared. Secondly, the type of vegetation investigated during the experimental campaign is categorized in

one of the enlisted options. Even though categories have been created, artificial representations of vegetation might differ per study (e.g., flexibility, density). More variables like the diameter and submergence are also an essential consideration for specific findings. Some studies have even collected pieces of real vegetation to be tested in wave flumes. Others have developed artificial models that could facilitate the understanding of variations like density and flexibility. In the third column, the generated waves during the study are mentioned. If both regular (harmonic wave, monochromatic, one frequency) and irregular waves (random spectra) have been generated during the experiment, 'irregular waves' is mentioned in the cell. Finally, the wave heights and periods used during the study are shared (if explicitly found in their publications) to provide the reader with an idea of the conditions studied.

In Table 2.2, the identified field campaigns that measured waves in vegetated environments are summarized. The referenced study, vegetation type, and hydrodynamic conditions of the measurements (duration and event measured) are enlisted in four columns. The duration of the measurements is mentioned to provide an idea of the range of measured conditions. The category '> year' is used on the list for campaigns that measured data over periods longer than a year. The type of events observed was categorized by looking at the reported values and authors' descriptions. If a storm or extreme tide is mentioned, the conditions are categorized as 'High.' The storm's return periods should also be considered when trying to discuss the effect of vegetation in extreme circumstances. The conditions are described as 'Moderate' if waves higher than 0.4 m are reported. Finally, the category 'Low' is used for the rest of the studies (daily conditions or low energy events). Important to mention is that the relative change of conditions on that site affects the category definition. At specific locations, large waves could be the norm, while in others, moderate disturbances are already extreme events.

Wave Flume Experiments				
Reference	**Model Configuration**	**Waves**	H_{m0} [m]	T_p [s]
Keulegan [1958]	Rigid cylinders and plates	Regular	NF	NF
Asano et al. [1988]	Flexible artificial seaweed	Regular	0.036-0.194	0.7-2.0
Fonseca et al. [1992]	Natural seagrass	Irregular	>0.09 m	1.4-2.5
Dubi and Tørum [1995]	Flexible artificial kelp	Irregular	0.08-0.17*	1.9-4.5*
Løvås and Tørum [2000]	Flexible artificial kelp	Irregular	0.08-0.17*	2.5-4.5*
Tschirky et al. [2001]	Natural marsh	Irregular	NF	NF
Bouma et al. [2005]	Natural and artificial marsh grass	Regular	0.05	1
Lima et al. [2007]	Flexible nylon ropes (grass)	NF	NF	NF
Lowe et al. [2007]	Rigid cylinders	Irregular	NF	NF
Augustin et al. [2009]	Rigid cylinders / flex. tube	Irregular	0.085	1.5-2.0
Penning et al. [2009]	Natural macrophyte	Regular	0.035-0.040**	0.5-2.0
Cavallaro et al. [2010]	Flexible artificial seagrass	Regular	0.045	0.74
Luhar et al. [2010]	Flexible artificial seagrass	Regular	0.16-0.39	0.9-2.0
Huang et al. [2011]	Rigid cylinders	Solitary	0.02-0.06	NF
Sánchez-González et al. [2011]	Flexible artificial seagrass	Irregular	0.03-0.13	1.25-2.50
Stratigaki et al. [2011]	Flexible artificial seagrass	Irregular	0.39-0.43***	2.3-3.5
Manca et al. [2012]	Flexible artificial seagrass	Irregular	0.21-0.34	1.97-4.27
Paul et al. [2012]	Flexible artificial seagrass	Regular	0.1	1.0
Koftis et al. [2013]	Flexible artificial seagrass	Irregular	0.28-0.40	2.0-4.5
Anderson and Smith [2014]	Flexible tubing	Irregular	0.05-0.19	1.25-2.25
Hu et al. [2014]	Rigid cylinders	Regular	0.04-0.20	1.0-2.5
Möller et al. [2014]	Natural marsh	Irregular	0.10-0.90	1.4-5.1
Ozeren et al. [2014]	Natural and artificial marsh	Irregular	0.03-0.10	0.7-1.8
Ni [2014]	Rigid cylinders	Regular	0.04-0.20	1.0-2.5
Maza et al. [2015]	Natural marsh	Irregular	0.12-0.60	1.7-3.0
van Rooijen et al. [2016a]	Rigid cylinders	Regular	0.047-0.204	3.0-7.0
Rupprecht et al. [2017]	Natural marsh	Regular	0.10-0.90	1.5-5.1
Yin et al. [2017]	Flexible artificial seagrass	Regular	0.10	1.5
John et al. [2018]	Flex. and rigid artificial seagrass	Regular	0.08-0.16	1.8-2.0
He et al. [2019]	Flexible plastic blades	Regular	0.03-0.12	1.0
Lei and Nepf [2019]	Flexible artificial seagrass	Regular	0.016-0.010	1.0-2.0
Jacobsen et al. [2019]	Rigid cylinders	Irregular	0.04-0.16	1.0-3.5
van Rooijen et al. [2020]	Rigid cylinders	Regular	0.09-0.14	2.0-5.0

Table 2.1: Table summarizing experimental campaigns over wave dissipation by vegetation (NF: not found).
* Target conditions reported in full scale, scaling factor obtained from own calculations based on one example shared in the study.
** Mean wave height ***H_{rms}

Field Measurements			
Reference	**Vegetation**	**Duration Campaign**	**Conditions**
Wayne [1976]	Marsh	NF	NF
Knutson et al. [1982]	Marsh	Experimental vessel waves	
Möller et al. [1999]	Marsh	> year	Moderate-High
Granata et al. [2001]	Seagrass	4 days	Moderate-High
Möller and Spencer [2002]	Marsh	10 months	Moderate-High
Cooper [2005]	Marsh	12 months	High
Möller [2006]	Marsh	12 months	Moderate
Phuoc and Massel [2006]	Mangroves	16 days	Moderate
Quartel et al. [2007]	Mangroves	2 months	High
Bradley and Houser [2009]	Seagrass	day(s)	Low
Dijkstra [2009]	Seagrass	7 days	Moderate
Lövstedt and Larson [2010]	Reed	4 days	Low
Paul and Amos [2011]	Seagrass	13 months	Low
Riffe et al. [2011]	Marsh	15 days	Low
Tschirky et al. [2001]	Marsh	> year	Low
Hansen and Reidenbach [2012]	Seagrass	3 weeks	Low
Infantes et al. [2012]	Seagrass	2 days	High
Yang et al. [2012]	Marsh	3 tides	Moderate
Jadhav et al. [2013]	Marsh	2 days	High
Serrano [2016]	Seagrass	16 days	High
Vuik et al. [2016]	Marsh	> year	High
Mullarney et al. [2017]	Mangroves	2 seasons	Moderate
Nowacki et al. [2017]	Seagrass	3 months	Moderate
Vuik et al. [2018a]	Marsh	> year	Moderate-High
Baron-hyppolite [2018]	Marsh	7 days	Moderate
Zhu et al. [2020b]	Marsh	> year	High

Table 2.2: Table summarizing field campaigns over wave dissipation by vegetation (NF: not found).

As mentioned in the description of the wave spectrum, each harmonic component has a unique frequency. The submergence ratio of vegetation (h_v/d) will determine the regime (deep, intermediate, or shallow waters) in which the stems interact with each wave, as displayed in Figure 2.4. The magnitude of the orbital velocity in the presence of vegetation is related to the dissipation each wave component could experience. This would assume that longer-period (low frequency) components in the spectrum are more attenuated than shorter-period (high frequency) components when traveling through submerged vegetation. This has been confirmed by the experimental campaign of Lowe et al. [2007], who concludes that the energy dissipation rate in canopies is greater for longer wave components. Nevertheless, other experimental studies (e.g. Bradley and Houser, 2009, Hansen and Reidenbach, 2012, Zhu and Chen, 2018) found that vegetation acts as a 'low-pass' filter removing high frequency motion and having little effect on longer components. From the full-scale experiments of Stratigaki et al. [2011] continued by Manca et al. [2012], larger dissipation was reported at the peak frequency and a less efficient dissipation for large waves. In the field, larger energy reduction to mid-range wave frequencies was also measured by Nowacki et al. [2017].
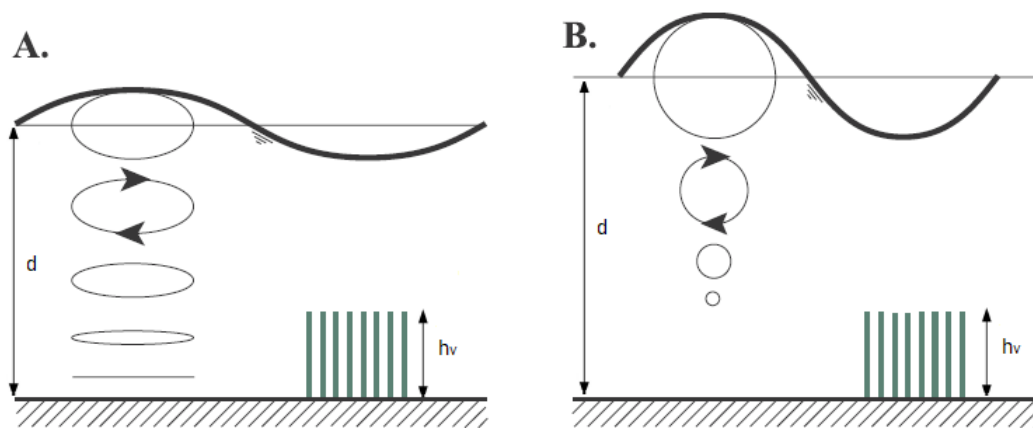

Figure 2.4: Wave interaction with submerged vegetation in **A.** shallow and **B.** deep water regimes. (Modified from Jacobsen et al., 2019)

The differences between the effect of dissipation on specific frequencies could be explained by looking at the measurements, highlighting the importance of Table 2.1 and 2.2. While Lowe et al. [2007] based the conclusions on an experimental campaign over rigid cylinders, the others are provided by measurements where flexibility is present. Flexibility is inherent for natural vegetation and variable between species and seasons. Studies have reported that flexibility causes the geometry of the plant to change with the wave period, altering the drag and inertial forces in the element (e.g., Lowe et al., 2007, Bradley and Houser, 2009, Beudin et al., 2017). The reduction of dissipation caused by flexibility has been indicated by Riffe et al. [2011], who concluded that dissipation through a natural salt marsh was about half of the expected dissipation for rigid vegetation. In the experimental campaign of Ozeren et al. [2014], flexible artificial stems had a smaller drag comparing it to artificial rigid elements, but it was also reported that live vegetation had more drag than both rigid and flexible artificial models. This shows that other effects in natural vegetation also contribute to the dissipation. The complexity of these processes was included by tuning the drag coefficient (CD) in the explicit model of Dalrymple et al. [1984].

Nowadays, it has been confirmed that wave modeling over flexible stems (e.g. salt-marshes) is improved by considering the stem motion [Riffe et al., 2011]. The reduction of drag due to flexibility is accounted for with the general approach of Luhar and Nepf [2011] and Dijkstra [2008]. These steady flow models estimate the theoretical posture of the plant and effective blade length, which can be used instead of the total measured vegetation height. The impact of flexibility is related to the stem height, stiffness, degrees of motion, and the orbital velocities of the incident forcing [Luhar and Nepf, 2016]. The frequency-dependent analysis of Bradley and Houser [2009] reported that the seagrass blade movement was out of phase to the peak frequency (0.67 Hz) while near to a 0 phase relationship for low frequencies (0.38 Hz). This causes the grass to move with the flow and longer wave components but not with other frequencies, which is consistent with the measured reduced dissipation at low frequencies. Nevertheless, the field measurements from Nowacki et al. [2017] reported a different pattern of preferential lower-frequency dissipation than other field studies (e.g., Bradley

and Houser, 2009, Hansen and Reidenbach, 2012). This is explained by the complicated interaction of non-linear processes, wind, and bathymetry on the field. The vegetation height and density are also affected by stem breakage during energetic events. This was studied and solved by Vuik et al. [2018a], who created a model in which critical orbital velocities can be implemented in the wave energy balance to include this effect. Applying the model to a salt-marsh project concluded that the bulk dissipation was similar before and after breakage.

Dissipation models (e.g., Dalrymple et al., 1984, Mendez and Losada, 2004) have assumed that the linear wave theory holds within the vegetation. This decision has been supported by Luhar et al. [2010], who reported the velocity profile not to be significantly modified by vegetation and to be a function of the orbital excursion and blade spacing. Measurements report reduced near-bottom mean velocities by 70-90% [Hansen and Reidenbach, 2012] and a 15% reduction on bed wave stress [Nowacki et al., 2017]. The assumption of linear wave theory has been proven to not be valid within the canopies (e.g., Lowe et al., 2005, Jacobsen et al., 2019). Nevertheless, the use of linear wave theory for canopies can be assumed if an in-canopy velocity reduction factor (α_u) is accounted for, providing accurate results for the canopies experiments of van Rooijen et al. [2016a] and Jacobsen et al. [2019]. The velocity profile is modified by vegetation within and above the canopies, depending on the conditions. Large values of vegetation density (N_v) on submerged cases cause a drag discontinuity at the top of the canopy generating a shear layer with vortices [Nepf, 2012]. Supporting this finding, van Rooijen et al. [2020] determined that the mean canopy flow is related to the turbulent Reynolds stresses and the wave vorticity by the canopy influence. This highlights the importance of non-linear processes (as vorticity) in the flow and dissipation when submerged vegetation is present. According to Zhu and Chen [2017], linear-based theoretical models remain valid for emergent cases and submerged cases with a Ursell number ≤ 30 ($N_{Ursell} = HL^2/d^3$). For the other cases, the inability to simulate the in-canopy velocity reduction and the non-linear triad interactions contributes to the large mismatch in submerged cases.

The velocity profile assumption has a significant impact on the drag coefficient (CD), which represents the vegetation's opposition to the flow. This depends not only on the vegetation characteristics (skin friction and form drag) but also on the flow properties. Orbital velocities change between wave components and frequencies, resulting in many studies investigating an accurate model for its prediction. The drag coefficient has been estimated through the Keulegan-Carpenter (KC) number (e.g. Mendez and Losada, 2004, Sánchez-González et al., 2011, Suzuki et al., 2011, Jadhav et al., 2013, Ozeren et al., 2014) and Reynolds number (Re) (e.g.Bradley and Houser, 2009, Koftis et al., 2013, Anderson and Smith, 2014, Hu et al., 2014). Important to highlight is that bulk drag coefficients derived from other models like Mendez and Losada [2004] cannot be universally applied to an energy spectral dissipation model such as Suzuki et al. [2011]. Drag coefficients have been proven to be different by a factor 3 between Mendez and Losada [2004] and Suzuki et al. [2011] to obtain the same bulk dissipation at $k_p d = 1.5$ [Jacobsen et al., 2019]. Other studies have investigated the dependence of the drag coefficient per frequencies. The experimental results from van Rooijen et al. [2016a] concluded that a constant drag coefficient could be applied if the velocity reduction factor (α_u) is included. The frequency dependence of the drag coefficient has also been demonstrated on the field by other studies (e.g., Bradley and Houser, 2009, Jadhav et al., 2013, Nowacki et al., 2017) who report that a spectral drag coefficient outperforms an integral value. The variation of the drag coefficient per frequencies shows differences between the measurements, and there is no model yet to predict velocity reduction and flexibility factors per frequencies.

Vegetation can affect important parameters for coastal risk assessments like IG waves and the wave set-up, according to van Rooijen et al. [2016b]. The measurements of Bradley and Houser [2009] and Koftis et al. [2013] display a possible presence of IG waves by an increase of energy below 0.05 Hz. Wave-wave and wave-bathymetry interactions might cause not only IG waves but also a redistribution of energy in all frequencies. The increase in non-linearity has been reported to cause more dissipation by vegetation [Wu and Cox, 2015]. Non-linear processes interacting with the bathymetry were critical for the spectral evolution in the measurements of Nowacki et al. [2017] in which quadruplets were more significant than triads in a vegetated shallow open water environment. The importance of near resonance triad interactions has been studied by Zhu and Chen [2018], who found that neglecting them could lead to underestimating damping rates. Triad interactions shift energy to higher frequencies, which are more dissipated.

Horizontal variations on the vegetated field might also interact with the spectral evolution. If the vegetation is emergent, the reduced resistance in unvegetated areas causes a stronger return flow, which explains the morphological development and maintenance of channels in vegetated foreshores. This effect is reduced

for submerged conditions, resulting in a more homogeneous flow [Temmerman et al., 2005]. Nevertheless, for submergences of h_v/d = 0.2-0.5, Ma et al. [2013] concluded that an onshore mean flow occurs in the unvegetated area and offshore return flow in the submerged patchy vegetated zone by pressure gradients and large-scale vortices. This finding is in agreement with Luhar et al. [2010], who reported a strong mean current near the top of the canopy due to nonzero wave stresses. This onshore mass flow is compensated with a strong return flow on top of the canopies. These studies show the presence of currents on top and around vegetation fields, which might influence wave transformation. Currents can either increase or decrease the wave dissipation according to studies. The interaction between flow and waves has been importantly indicated by Paul et al. [2012], who mentions a possible overestimation of the wave attenuation for tidal environments if the currents are not considered. Others [Maza et al., 2015] reported lower damping rates when waves and currents travel in the same direction and the inverse for opposite directions. According to the findings of Hu et al. [2014], this behavior is linked to the velocity ratio between waves and currents.

2.3. Explicit and Implicit Wave Modeling over Vegetation

Many dissipation models have been proposed in the literature to reproduce the dissipation of wave energy by vegetation (e.g. Knutson et al., 1982, Dalrymple et al., 1984, Madsen et al., 1988, Kobayashi et al., 1993, Mendez and Losada, 2004, He et al., 2019, Jacobsen et al., 2019). While some of these models focus on the overall total wave height decay, others consider the spectral distribution of the dissipation. Most reproduce wave dissipation by implementing vegetation explicitly, including physical representations of the stems. Some of the parameters to describe vegetation explicitly are the vegetation height (h_v), stem diameter (b_v), the density of stems per area unit (N_v), and the drag coefficient (CD). This last coefficient represents the opposition of vegetation against the water motion and highly depends on vegetation's biomass and flexibility. Implicit modeling, on the other hand, includes vegetation as an equivalent large bed roughness value (friction). Within implicit modeling, most dissipation models were developed for another purpose and lack of a physical link to the vegetation characteristics. Nevertheless, formulations can keep physical relevance by representing it as roughness length [Madsen et al., 1988].
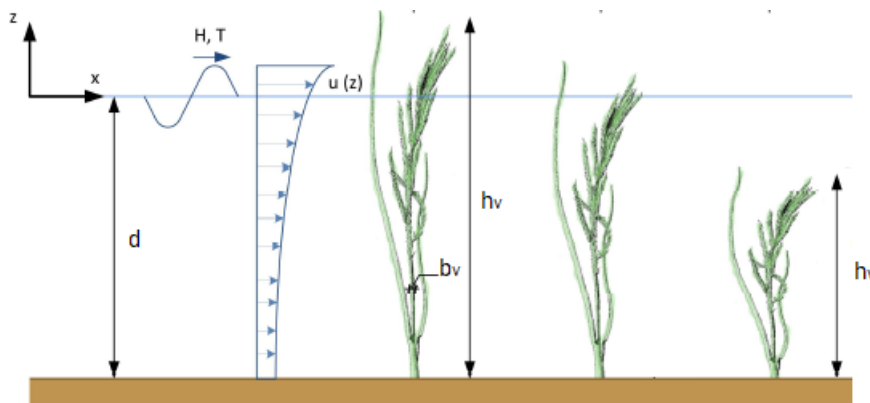

Figure 2.5: Some vegetation parameters representing physical properties of the stem in explicit modeling. (Modified from van Zelst, 2018)

Explicit models that are based on canopies assume a rigid approximation representing vegetation with cylinders or plates. In this representation, flexibility is accounted up until certain valid regions. According to Mendez and Losada [2004], species like L. hyperborea kelp beds, P. oceanica seagrass meadows, and Spartina marshes have the properties to be included in this approach. The rigid canopies approach is valid if the stem is:

- Subsurface, short, or if its stiffness in the lower part is strong.

- Has a small number of degrees of freedom

Previous studies (e.g., Quartel et al., 2007, Baron-Hyppolite et al., 2019, Nowacki et al., 2017, Samiksha, Vethamony, Bhaskaran, Pednekar, Jishad, 2019) have investigated the accuracy of implicit and explicit models

for predicting the wave spectral dissipation by vegetation. The vegetation characteristics (density, flexibility, and structure) have been identified as an essential factor in the conclusions. The vegetation trunks, leaves, and roots seem to dominate the dissipation process in vegetated areas, as reported by Quartel et al. [2007], who concludes that the friction by clay particles was very low compared to the drag and inertial forces of the vegetation.

The implicit method under-represents the complexity of wave-vegetation interaction, according to both Baron-Hyppolite et al. [2019] and Nowacki et al. [2017]. Including the stems' physical representation better reflect the physics and could reduce model over-tuning [Nowacki et al., 2017]. In agreement with these statements, the measurements of Baron-Hyppolite et al. [2019] reported a dissipation error higher than 30% for implicit modeling compared to the 20% from explicit modeling. Despite the previous agreement, implicit modeling agree with the spectral measurements of Nowacki et al. [2017] while the explicit model over-predicted the low-frequency energy. The differences between studies provide clear reasoning behind the findings, Nowacki et al. [2017] measured submerged seagrass while Baron-Hyppolite et al. [2019] did it for emergent marshes. The good performance of implicit modeling for submerged vegetation is caused by its capability to assign more dissipation to lower frequencies depending on the submergence, while the explicit model depends on one characteristic frequency [Nowacki et al., 2017]. The model of [Suzuki et al., 2011] uses mean wave parameters ($\tilde{k}$ and $\tilde{\sigma}$) applying a single multiplicative constant across frequencies. This assumption in the model agrees for emergent vegetation (as Baron-Hyppolite et al. [2019]) and to previous field campaigns which reported peak dissipation at f_p for values of $k_p h < 1$ [Jacobsen et al., 2019].

2.4. Models for Comparison with SWAN

The SWAN model is a Eulerian model based on the action density spectrum $N(\sigma,\theta)$ with the independent variables the wave direction θ and the relative frequency σ, as observed from a frame of reference moving with the current velocity.

$$N(\sigma,\theta) = \frac{E(\sigma,\theta)}{\sigma} \qquad \text{[m}^2\text{ s}^2\text{]} \quad (2.1)$$

The spectral action balance equation describes the rate of change of the action density N at a single point in space($\vec{x}$, σ, θ), that defined for Cartesian coordinates is given by equation 2.2 (e.g., Hasselmann et al., 1973, Komen et al., 1994). The ambient current is assumed to be uniform over the vertical co-ordinate and is therefore denoted as $\vec{U}$ [The SWAN team, 2019d].

$$\frac{\partial N}{\partial t} + \nabla_{\vec{x}} \cdot [(\vec{c_g} + \vec{U})N] + \frac{\partial c_\sigma N}{\partial \sigma} + \frac{\partial c_\theta N}{\partial \theta} = \frac{S_{tot}}{\sigma} \qquad \text{[m}^2\text{ s]} \quad (2.2)$$

The first term describes the kinematic part of the equation. The second denotes the propagation of energy in the two-dimensional geographical $\vec{x}$-space, including wave shoaling following the dispersion relation of linear wave theory. The third and fourth terms include the shift of frequencies and refraction by the depth and current variations. The last term at the right hand is the energy source term (S_{tot}), which accounts for the physical processes responsible for the dissipation, generation, and redistribution of energy between waves [Booij et al., 1999]. The source term includes mechanisms like wave-growth due to wind (S_{in}), white capping ($S_{ds,wc}$), depth-induced breaking ($S_{ds,br}$), energy transfer due to quadruplets (S_{nl4}) and triads (S_{nl3}), bottom friction ($S_{ds,bot}$), dissipation due to vegetation ($S_{ds,veg}$), fluid mud-induced wave dissipation ($S_{ds,m}$), dissipation due to turbulent viscosity ($S_{ds,t}$), and dissipation by sea ice ($S_{ds,ice}$) [The SWAN team, 2019d].

$$S_{tot} = S_{in} + S_{ds,wc} + S_{ds,br} + S_{nl4} + S_{nl3} + S_{ds,bot} + S_{ds,veg} + S_{ds,m} + S_{ds,t} + S_{ds,ice} \quad \text{[m}^2\text{/s]} \quad (2.3)$$

Explicit and Implicit modeling are two approaches for vegetation modeling that are based on different dissipation mechanisms. The bottom friction term $S_{ds,bot}$ refers to implicit modeling while $S_{ds,veg}$ to the explicit model. In the present version, the options to activate these two physical processes are described in the SWAN documentation (The SWAN team, 2019a; The SWAN team, 2019d;). The source term for bottom friction dissipation in SWAN uses the bed friction coefficient (C_b) in the general form:

$$S_{ds,bot}(\sigma,\theta) = -C_b \frac{\sigma^2}{g^2 \sinh^2 kd} E(\sigma,\theta) \qquad \text{[m}^2\text{]} \quad (2.4)$$

Bottom friction available models in SWAN are Hasselmann et al. [1973] , Collins [1972], Madsen et al. [1988], and Smith et al. [2011]. Previous studies (e.g., Nowacki et al., 2017, Baron-Hyppolite et al., 2019, Samiksha, Vethamony, Bhaskaran, Pednekar, Jishad, 2019) used Madsen et al. [1988] and Collins [1972]. The friction coefficient C_b is obtained for Collins [1972] through the user input C_f (default value in SWAN [cfw] = 0.015) and the near-bed velocity u_{rms} is computed at each location.

$$C_b = C_f g u_{rms} \qquad \text{[m}^2\text{/s}^3\text{]} \quad (2.5)$$

Madsen et al. [1988] in SWAN iterates the friction coefficient f_w solving the formulation of [Jonsson, 1966], which uses the near-bottom excursion amplitude (A_b) and the Nikuradse bottom roughness length (k_N) (default value in SWAN [kn] = 0.05).

$$C_b = f_w \frac{g}{\sqrt{2}} u_{rms} \qquad \text{[m}^2\text{/s}^3\text{]} \quad (2.6)$$

with

$$\frac{1}{4\sqrt{f_w}} + log\frac{1}{4\sqrt{f_w}} = -0.08 + log\frac{A_b}{k_N} \qquad \text{[–]} \quad (2.7)$$

For values of A_b/k_N smaller than 1.57, the friction factor f_w is 0.3 [Jonsson, 1966]. This upper limit reduces its applicability and physical relevance to vegetation heights larger than its limit. From previous tests, Nowacki et al. [2017] evaluated a roughness length of 0.01, which produced values already outside of the limit. Modifications to this formulation have been developed to increase the upper limit but are not yet available in SWAN. A comparison of both implicit models has reported differences in their spectral dissipation.

The explicit vegetation modeling option in SWAN is based on Dalrymple et al. [1984], who defined the time-average rate of energy dissipation per unit horizontal area induced by vegetation as described in Equation 2.8. Here, we assume the flow direction in the x direction. The forces in the vertical are assumed to be negligible compared to the horizontal force (F_x) for vegetation fields. The vegetation (either submerged or emergent) only interacts with the waves in the submerged section. Therefore, the value of h_v should be limited to be equal or smaller than the local water depth (d).

$$\frac{\partial E c_g}{\partial x} = -\varepsilon_v = -\overline{\int_{-d}^{-d+h_v} F_x u dz} \qquad \text{[kg/s}^3\text{]} \quad (2.8)$$

For a vegetation field, the time average stands for a wave period, F_x for the force on the vegetation per unit volume, and u for the fluid velocity. The forces are expressed in terms of a Morrison-type equation neglecting swaying motion and inertial forces as described in Equation 2.9.

$$F_x = \frac{1}{2}\rho C_D b_v N_v u|u| \qquad \text{[kg/(m}^2\text{ s}^2\text{)]} \quad (2.9)$$

Assuming linear wave theory for regular waves traveling over an impermeable bottom, the model of Dalrymple et al. [1984] is given by:

$$\varepsilon_{v,D} = \frac{2}{3\pi}\rho C_D b_v N_v \left(\frac{gk}{2\sigma}\right)^3 \frac{\sinh^3 kh_v + 3\sinh kh_v}{3k\cosh^3 kd} H^3 \qquad \text{[kg/s}^3\text{]} \quad (2.10)$$

The model from Dalrymple et al. [1984] was extended by Mendez and Losada [2004] to cope with irregular waves. For this purpose, a very narrow banded spectrum in frequencies and directions (invariant Rayleigh distribution) was assumed to substitute the regular wave height H for its irregular equivalent H_{rms}. The evolution of the wave height in the model is related to the peak period and mean direction.

$$D_{veg_{ML,tot}} = \varepsilon_{v,ML} = \frac{1}{2\sqrt{\pi}}\rho C_D b_v N_v \left(\frac{gk_p}{2\sigma_p}\right)^3 \frac{\sinh^3 k_p h_v + 3\sinh k_p h_v}{3k_p\cosh^3 k_p d} H_{rms}^3 \qquad \text{[kg/s}^3\text{]} \quad (2.11)$$

The model was later modified by Suzuki et al. [2011] relating the velocity profile (therefore the dissipation) to mean spectral characteristics ($\tilde{\sigma}, \tilde{k}$) as defined in WAMDI Group [1988].

$$D_{veg*_{S,tot}} = \frac{1}{\rho g} D_{veg_{S,tot}} \qquad\qquad \text{[m}^2\text{/s]} \quad (2.12)$$

with

$$D_{veg_{S,tot}} = \frac{1}{2\sqrt{\pi}} \rho C_D b_v N_v \left(\frac{g\widetilde{k}}{2\widetilde{\sigma}}\right)^3 \frac{\sinh^3 \widetilde{k}h_v + 3\sinh \widetilde{k}h_v}{3\widetilde{k}\cosh^3 \widetilde{k}d} H_{rms}^3 \qquad \text{[kg/s}^3\text{]} \quad (2.13)$$

Distributing the dissipation equally to all frequencies and directions and substituting $H_{rms}^2 = 8E_{tot}$, the formulation implemented in SWAN by Suzuki et al. [2011] is given by:

$$S_{ds,veg_S}(\sigma,\theta) = -\frac{D_{veg*_{S,tot}}}{E_{tot}} E(\sigma,\theta) \qquad\qquad \text{[m}^2\text{]} \quad (2.14)$$

in which final form is:

$$S_{ds,veg_S}(\sigma,\theta) = -\sqrt{\frac{2}{\pi}} g^2 C_D b_v N_v \left(\frac{\widetilde{k}}{\widetilde{\sigma}}\right)^3 \frac{\sinh^3 \widetilde{k}h_v + 3\sinh \widetilde{k}h_v}{3\widetilde{k}\cosh^3 \widetilde{k}d} \sqrt{E_{tot}} E(\sigma,\theta) \qquad \text{[m}^2\text{]} \quad (2.15)$$

where

$$
\begin{aligned}
g &= \text{gravitational acceleration}\\
C_D &= \text{drag coefficient}\\
b_v &= \text{canopy diameter}\\
N_v &= \text{canopies density}\\
\widetilde{k} &= \text{mean wave number}\\
\widetilde{\sigma} &= \text{mean wave intrinsic frequency}\\
h_v &= \text{canopy height}\\
d &= \text{water depth}\\
E_{tot} &= \text{total variance density}\\
E(\sigma,\theta) &= \text{wave variance density with directional and frequency information}
\end{aligned}
$$

The model of Suzuki et al. [2011] included in SWAN the possibility to define different vegetation variables over the vertical axis. Significant biomass differences exist between the roots, stems, and leaves of vegetation like mangroves or willow trees that interact with waves during floods. The importance of including this vertical variation in wave modeling has been validated [Wu et al., 2016]. Also, the possibility to change and define different vegetation densities is possible in the model.

The model has been validated against experimental and field measurements. The bulk dissipation and overall wave decay have shown good results by calibrating the CD. During the model development and validation, the spectral shape was not included in the investigation [Suzuki et al., 2011]. The model assumes that the dissipation on a given frequency is related to the energy density content on that particular frequency. The effects of choices made for this model on the bulk and frequency-dependent dissipation are discussed in the upcoming section.

2.4.1. New Dissipation Model

The new frequency distributed dissipation model for canopies calculates the orbital velocities per component at a given vertical elevation in which the velocity contributions from all frequencies are linearly superpositioned. The model uses a Morrison type formulation to represent the drag forces, which neglects added mass inertia and swaying. If vegetation is partially present in the water column, each component's velocity at a given elevation will experience an energy reduction by the canopy at that vertical point. For submerged

canopies, this naturally adds a cut-off frequency above which dissipation vanishes (similar to the bottom friction term). The work of Jacobsen et al. [2019] defines the frequency cut-off by the linear wave theory. This represents the frequency at which the orbital velocities are negligible at the top of the canopies, given as:

$$f_{\text{cut-off}}^2 = \frac{1}{2(d - h_v)} \frac{g}{2\pi} \qquad [\text{Hz}^2] \quad (2.16)$$

The velocity spectrum has been associated with the surface elevation by the linear wave theory. This assumes the velocity profile is not affected by the canopies, which has been proven not to be true [Lowe et al., 2005]. The influence of canopies on the velocity profile and added inertia is done via the in-canopy reduction factor (α_u). Due to the lack of a suitable formulation, both CD and α_u are included as frequency-independent. Next, the dissipation per frequency is numerically integrated over the height of the canopy, assigning the experienced dissipation to each component of the surface elevation spectrum (variance density spectrum), which results in the depth-integrated formulation of Jacobsen et al. [2019]:

$$D_{veg_J}(\omega,\theta) = \int_{-d}^{-d+h_v} 2\Gamma S_u(\omega,\theta) \sqrt{\frac{2m_{u,0}}{\pi}} dz \qquad [\text{kg/s}^2] \quad (2.17)$$

with

$$\Gamma = \frac{1}{2} \rho \alpha_u^3 C_D b_v N_v \qquad [\text{kg/m}^4] \quad (2.18)$$

$$S_u(\omega,\theta) = \left(\frac{\omega \cosh k(z+d)}{\sinh(kd)} \right)^2 S_n(\omega,\theta) \qquad [\text{m}^2/\text{s}] \quad (2.19)$$

where

$$
\begin{aligned}
d &= \text{water depth} \\
h_v &= \text{canopy height} \\
\rho &= \text{water density} \\
\alpha_u &= \text{in-canopy velocity reduction factor} \\
C_D &= \text{drag coefficient} \\
b_v &= \text{canopy diameter} \\
N_v &= \text{canopies density} \\
\omega &= \text{wave absolute frequency per component} \\
k &= \text{wave number per component} \\
z &= \text{elevation with zero at the water surface and -depth at the bottom} \\
S_n(\omega,\theta) &= \text{surface elevation spectrum} = E(\sigma,\theta) \text{ wave variance density} \\
m_u &= \text{first order moment of the velocity spectrum } (S_u)
\end{aligned}
$$

The vertical integration is solved through numerical integration, as no closed form for the integration was found. The Simpson rule numerical method is used for this purpose. The use of 21 points is sufficient to keep the error of this approximation below 0.1% for most cases, which increases with $k_p h$ and h_v/d. In the comparison from Jacobsen et al. [2019], 501 points were used, which are well beyond the minimum requirements. This is investigated during the implementation of the model in the present report.

The new model was compared with implicit modeling [Madsen et al., 1988]. The analysis for bottom friction (not canopies), wherein the new model $\Gamma_b = \frac{1}{2}\rho f_w$, shown that both models have an identical dissipation spectral shapes. Nevertheless, the two expressions are equivalent but do not match perfectly. The main difference is caused by the evaluation of u_{rms} as a constant scaling by Madsen et al. [1988]. This resulted in ignoring the cross-terms, which introduces a difference of factor two, according to [Jacobsen et al., 2019].

The bulk dissipation of the new model was compared to the explicit models of Mendez and Losada [2004] and Suzuki et al. [2011], as differences exist between them. The bulk dissipation is calculated as:

$$D_{veg_J,tot} = \int_0^{2\pi} \int_0^\infty D_{veg_J}(\omega,\theta) d\omega d\theta \qquad [\text{kg/s}^3] \quad (2.20)$$

This term is comparable to the equation 2.11 for the model of Mendez and Losada [2004] and equation 2.13 for the model of Suzuki et al. [2011]. For the comparison, the use of the bulk dissipation ratio of each model over the bulk dissipation of Jacobsen et al. [2019] is used to identify the conditions where bulk differences are the highest. Four values of vegetation submergence are tested (h_v/d = 0.25, 0.50, 0.75, 1.00) and three JONSWAP peak enhancement factors (γ = 1.0, 3.3, 10.0). For the comparison and to be consistent, the velocity reduction factor is not included (α_u = 1.0) as the other models do not consider it. Also, no currents are included for the comparison in Jacobsen et al. [2019] and all frequencies in Mendez and Losada [2004] and Suzuki et al. [2011] were switched for their absolute value ω. Neglecting directional differences by a 1D comparison and defining x as the model to compare, the ratio is defined as:

$$\text{Ratio}_x = \frac{D_{veg_x,tot}}{D_{veg_J,tot}} \qquad [-] \quad (2.21)$$

which for the model of Mendez and Losada [2004] is given as:

$$\text{Ratio}_{ML} = \frac{\frac{1}{2\sqrt{\pi}} \rho C_D b_v N_v \left(\frac{gk_p}{2\omega_p}\right)^3 \frac{\sinh^3 k_p h_v + 3\sinh k_p h_v}{3k_p \cosh^3 k_p d} H_{rms}^3}{\int_0^\infty \int_{-d}^{-d+h_v} \rho C_D b_v N_v \left(\frac{\omega \cosh k(z+d)}{\sinh(kd)}\right)^2 S_n(\omega)\sqrt{\frac{2m_{u,0}}{\pi}} dz d\omega} \qquad [-] \quad (2.22)$$

The bulk dissipation of the new model compared to the bulk dissipation of Mendez and Losada [2004] shows larger differences for lower γ and h_v/d values, as described in Figure 2.6. The relation between depth and wave periods, which indicate the water regime, are included with $k_p h$ ($k_p d$).
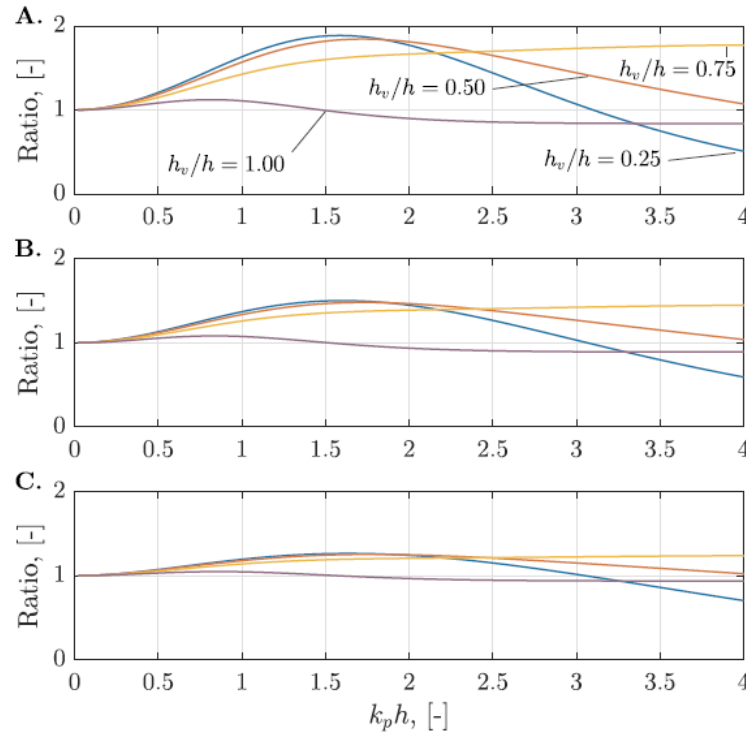

Figure 2.6: The ratio of the bulk dissipation from Mendez and Losada [2004] over Jacobsen et al. [2019] as a function of the height of the vegetation for **A.** γ = 1.0 ; **B.** γ = 3.3, **C:**; and γ = 10.0. (From Jacobsen et al., 2019)

The Ratio between both models' bulk dissipation reaches the unity for shallow water because the velocity profile is uniform of the height for all components [Jacobsen et al., 2019]. The dissipation of Mendez and Losada [2004] is stronger compared to the new model for $k_p d < 3.0$ with $h_v/d \leq 0.75$, and $k_p d < 1.5$ for

h_v/d = 1.00. The velocity profile's definition with the peak period will assign more dissipation to the peak (where most energy is present). Nevertheless, once shorter wave components characterize the spectra, the wave components that decrease exponentially might not experience submerged vegetation, allowing only long components to do it. In those cases, the new model assigns more dissipation. The bulk dissipation differences imply that different drag coefficients are required for each model. The C_D from Mendez and Losada [2004] depends on the properties of the canopies, submergence, and wave conditions. Therefore, drag coefficients between models are not exchangeable.

The differences between models are reduced for increasing values of the JONSWAP spectrum enhancement factor γ, leading to a narrower distribution of energy. Storm waves are often represented by a broad spectrum, a condition in which the Rayleigh distribution may be violated [Chen and Zhao, 2012]. The new model is not restricted to the assumption of a narrow-banded spectrum (Rayleigh distribution) as assumed in Mendez and Losada [2004], increasing the range of wave conditions for its applicability.

The implemented explicit model of Suzuki et al. [2011] in SWAN is defined in source term units (m^2), which cannot be compared to the bulk or spectral dissipation of the new model. Therefore, Jacobsen et al. [2019] used the bulk dissipation from equation 2.13. The spectral properties in this comparison ($H_{rms} = 8\,E$) follow from the assumption of a Rayleigh distribution. The bulk dissipation ratio is given as:

$$\text{Ratio}_S = \frac{\frac{1}{2\sqrt{\pi}}\rho C_D b_v N_v \left(\frac{g\widetilde{k}}{2\widetilde{\sigma}}\right)^3 \frac{\sinh^3 \widetilde{k}h_v + 3\sinh \widetilde{k}h_v}{3\widetilde{k}\cosh^3 \widetilde{k}d} H_{rms}^3}{\int_0^\infty \int_{-d}^{-d+h_v} \rho C_D b_v N_v \left(\frac{\omega \cosh k(z+d)}{\sinh(kd)}\right)^2 S_n(\omega)\sqrt{\frac{2m_{u,0}}{\pi}}\,dz\,d\omega} \qquad [-] \quad (2.23)$$

The comparison to the dissipation model of Suzuki et al. [2011] shows larger differences for increasing $k_p d$ and decreasing of h_v/d, as displayed in Figure 2.7. The dissipation of Suzuki et al. [2011] remains smaller for these conditions. The significant lower dissipation in Suzuki et al. [2011] compared to Jacobsen et al. [2019] for submerged vegetation with $k_p d > 1.5$ is attributed to the distribution of energy in the spectra. In a JONSWAP spectra, the mean frequency is higher than the peak. If the velocity profile is characterized by the mean frequency, the relative submergence in which dissipation vanishes is higher than a dissipation model defined by the peak or frequency-dependent. Long waves will still experience the dissipation at those elevation points which are neglected in Suzuki et al. [2011]. The bulk dissipation ratio for submergence vegetation reaches the unity between 1.0 and 2.5 of $k_p d$ depending on the submergence level. This translates into certain combination of conditions where calibration coefficients are equal for both models. Nevertheless, as these are highly sensitive to changes in the wavefield and submergence, C_D are neither exchangeable.

If emergent vegetation is present, all frequencies are affected by the presence of vegetation reducing the differences between the models. Nevertheless, these differences are present as frequencies in shallow conditions have stronger orbital velocities in the water column and are more affected in the model of Jacobsen et al. [2019]. The spectral shape's influence is investigated by modifying the enhancement factor (γ) for the JONSWAP spectra. Small enhancement peak factors (γ) and smaller vegetation heights relative to the water depth (h_v/d) amplify the Ratio between the model's solution for the bulk dissipation.

The comparison to the available explicit model in SWAN Suzuki et al. [2011] not only contributed to understanding the differences to the new model but also to the model of Mendez and Losada [2004]. The ratio show a stronger decay in Suzuki et al. [2011] for larger values of $k_p d$, having values close to zero for large submergences ($hv/h = 0.25$). The maximum value of the ratio comparison to Mendez and Losada [2004] reached values close to 2.0, while in Suzuki et al. [2011], do not exceed 1.3. Besides, the Ratio of small values of $k_p d$ does not reach the unity for shallow water conditions. These observations are likely explained to the choice of representative frequency and wavenumber ($\omega_{m,0} > \omega_p$). The following hypotheses are made in the analysis of Jacobsen et al. [2019]:

- A velocity profile represented by the peak characteristic has a faster decay towards the bed than one represented by mean characteristics.

- The use of the mean frequency by Mendez and Losada [2004] is a good representation of the velocity profile for the shallow waters and vegetation close to the water surface.

- The set $\{\widetilde{k}, \widetilde{\sigma}\}$ in Suzuki et al. [2011] does not fulfil the linear dispersion.
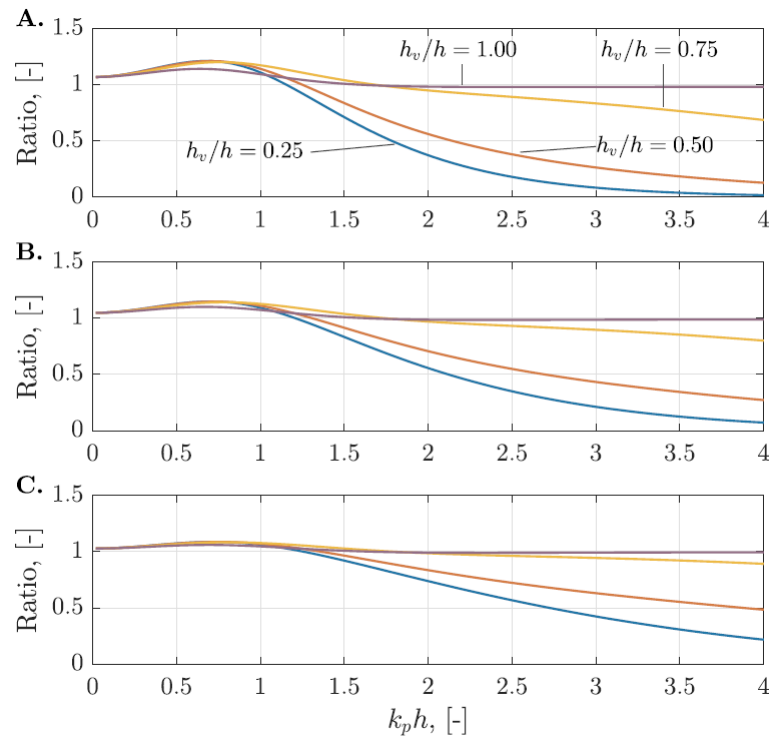
Figure 2.7: The ratio of the bulk dissipation from Suzuki et al. [2011] over Jacobsen et al. [2019] as a function the height of the vegetation for **A.** $\gamma = 1.0$; **B.** $\gamma = 3.3$, **C:**; and $\gamma = 10.0$. (From Jacobsen et al., 2019)

The dissipation shape of each model investigates the differences of each model in the spectral evolution by submerged vegetation ($h_v/d = 0.5$). This comparison to the model of Suzuki et al. [2011] uses four different values of $k_p d$ and two of γ. The sensitivity to these changing variables are displayed in Figure 2.8, which show larger differences for a wider spectra ($\gamma = 1.0$) and increasing values of $k_p d$. The comparison with the largest visual difference (**D.**) shows that the new model (in blue) assigns more dissipation to lower frequencies and less to high frequencies compared to Suzuki et al. [2011]. The new model dissipation cut-off for submerged vegetation allows small waves under the deeper relative conditions to not be as affected as it is in the equally distributed model of Suzuki et al. [2011].

The bulk dissipation ratio as seen in Figure 2.7 show that Suzuki et al. [2011] dissipation is stronger for $k_p d = 0.5$, which explains the differences at the peak and high frequencies in Figure 2.8. Nevertheless, for these conditions, no visible dissipation differences are observed for low frequencies. If equal bulk dissipation is achieved by calibrating the CD, small differences might be observable in low frequencies. The peak dissipation of the new model is shifted to lower frequencies when compared to Suzuki et al. [2011], which is clearly visible for the comparison with $\gamma = 1.0$ and $k_p d = 3.0$.

The new model was validated with an experimental campaign over irregular waves. The experimental setup described in Jacobsen et al. [2019] consisted of artificial blades with different lengths ($h_v/d = 0.38$, 0.67, 0.96) and thicknesses (which also modify the flexibility). The generated waves had two significant wave heights (3.7 and 6.8 cm) based on a JONSWAP spectrum with $\gamma = 3.3$ and $T_p = 1.15$ s. The normalized dissipation in Figure 2.9 displays a spectral shape almost identical to the measurements above the peak frequency but with a weak overprediction below the peak frequency. This is later investigated in the present report. In the validation, the model of Suzuki et al. [2011] was also tested and compared to the new model. The comparison at the wave gauges dissipation ranged between 0.74 and 0.87, which are close to the reported values in Figure 2.7. The spectral shape evaluation for Suzuki et al. [2011] shows a large overprediction of dissipation for frequencies over the f_p and an underprediction below f_p.

The work from Jacobsen et al. [2019] discusses and suggests that $\alpha^3 CD$ was fairly independent of the tested conditions. Nevertheless, the reduction factor's value could not be determined as no velocity measurements were performed within the canopies. The values of $\alpha^3 CD$ used for $h_v/d = \{0.38, 0.67, 0.96\}$ were
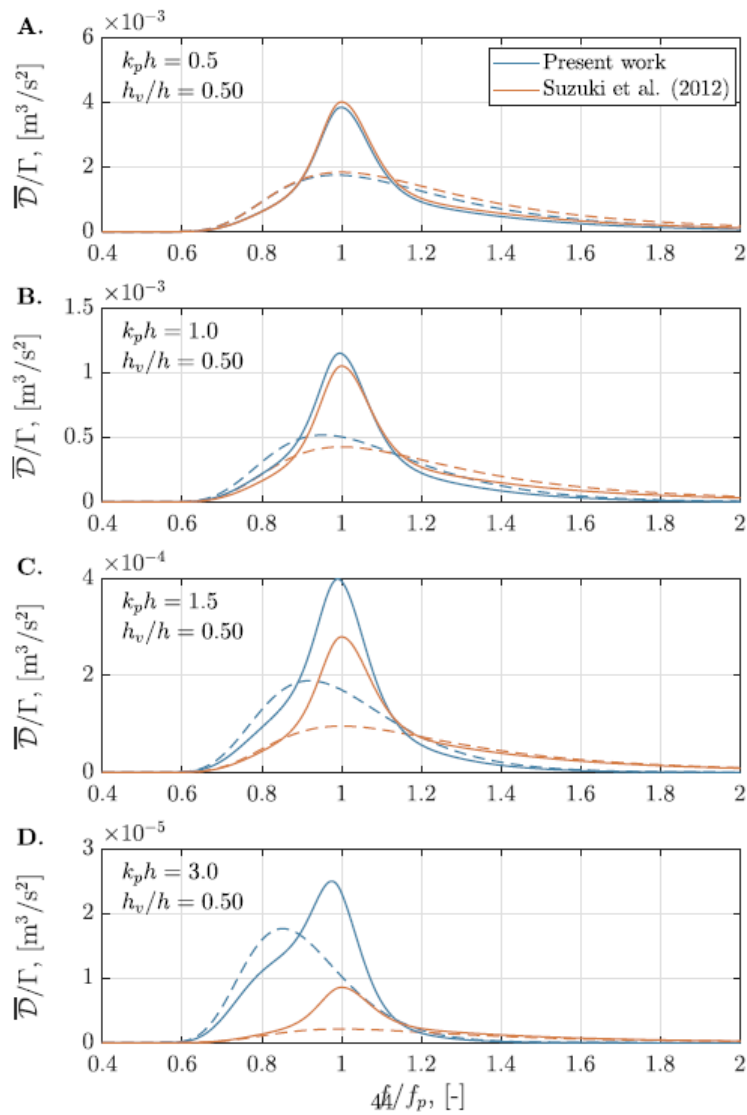
Figure 2.8: The frequency-distribution of the energy dissipation between Suzuki et al. [2011] (red) and Jacobsen et al. [2019] model (blue) for $\gamma = 1.0$ (dashed lines) and $\gamma = 3.3$ (full lines). **A:** $k_p d = 0.5$, **B:** $k_p d = 1.0$, **C:** $k_p d = 1.5$, **D:** $k_p d = 3.0$. (From Jacobsen et al., 2019)
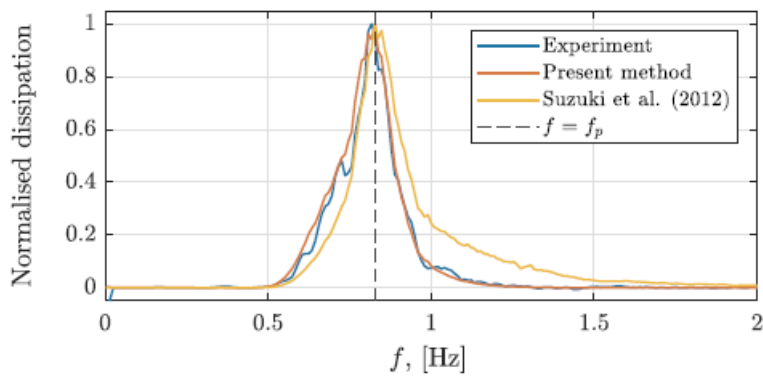

Figure 2.9: The measured normalised dissipation spectrum compared to the model of Jacobsen et al. [2019] and Suzuki et al. [2011] with vegetation properties of $N_v = 566$ stems/m^2, $b_v = 1$ mm, $h_v/d = 0.38$, $H_{m0}/h = 0.054$, $T_p = 1.15$ s, and $k_p d = 2.1$. (From Jacobsen et al., 2019)

{2.2, 1.3,0.4} respectively. The directional spreading will influence the bulk dissipation, as discussed in the present section. The work of Jacobsen et al. [2019] suggests a correction factor of 0.85.

From these previous comparisons, it can be concluded that the frequency-dependent model of Jacobsen et al. [2019] shows bulk and spectral differences to the available explicit model in SWAN for increasing submergence, frequencies, and width of the spectra. The dissipation model of Suzuki et al. [2011] assigns a multiplicative factor related to the mean frequency to all components. Including the velocity profiles for each frequency in Jacobsen et al. [2019] causes the peak of the dissipation shape to shift to frequencies lower than f_p, assigning larger dissipation to longer waves and conserving energy on high frequencies under submerged vegetation. This naturally incorporates a frequency cut-off where dissipation vanishes. The performance under the computational and experimental comparison shows that the new model could provide the frequency-dependent benefits of implicit modeling while keeping the stems' physical representation. Bridging the advantages of implicit and explicit modeling could reduce the spectral mismatch between measurements and models, and increase the range of values to its applicability. These results and further investigations of the report will be used to answer the research question, which relates to the spectral mismatch of storm waves modeling over submerged marshes.

3

New Model in SWAN

The implementation process of the new frequency-dependent model of Jacobsen et al. [2019] is described in the present chapter. The core of the implementation discussion is the choices and assumptions made during the creation of a new subroutine in SWAN. The possible effects of these choices are evaluated through a sensitivity analysis shared on this Chapter and Appendix B. Next, the validation is tested by developing computational experiments with regular and irregular waves, which are used to investigate the expected differences to the subroutine of Suzuki et al. [2011] in SWAN. This is related to the previous chapter's discussion, in which differences are discussed by varying h_v/d, k_pd, and γ. At the end of the chapter, a discussion gathers the main findings and its implications for the present research. In Appendix A, a short user manual of the newly developed subroutine is included for further use in SWAN.

3.1. Implementation

This section describes the implementation of the new dissipation model [Jacobsen et al., 2019] in the full spectrum model SWAN, which is used freely under the terms of the GNU General Public License source code. The SWAN website (http://swanmodel.sourceforge.net/) facilitates the access and download of the current official version's executable and source code. The implementation has been done in the latest stable version for Windows at the moment of the research (SWAN Cycle III version 41.31). A new subroutine has been coded in Fortran90 and further compiled using the Intel Fortran Compiler 19.0 Update 5 for 64 Windows applications and its redistributable libraries. This was accessed via the Visual Studio 2019 Developer Command Prompt v16.4.1. The new code was installed in the serial model because there was no need to share computational power with other cores for the present research. The guide for the use, programming, implementation, and technical features are available in the SWAN documentation (The SWAN team, 2019a, The SWAN team, 2019b, The SWAN team, 2019c, The SWAN team, 2019d).

The SWAN model solves the wave action balance (Equation 2.2), which is conserved in the presence of ambient current by using the relative frequency (σ). The absolute frequency (ω), as included in the model of Jacobsen et al. [2019], is hereafter exchanged for σ to match the SWAN implementation. If no current is present, the model is based on the energy balance, where this modification from the original form does not affect. Because the experimental campaign used in the present report does not include wave-current interaction in a controlled environment, the effects of this assumption are not explored in the present investigation but are recommended as further research. The field project for the last validation of this report do experience wave currents. The interaction of wave and currents for flexible submerged vegetation have been studied, confirming it to be crucial for the bulk and spectral dissipation (Chapter 2). Nevertheless, the measured currents over the vegetated field appear to be near zero, as displayed in Appendix D.

The new source term should have the same units to be comparable to the existing implementation. The variables and components of both dissipation models are carefully explained in Chapter 2. The vegetation source term from Suzuki et al. [2011] holds different units (m^2 in Equation 2.15) than the the dissipation term from Jacobsen et al. [2019] (kg/s^2 in Equation 2.20). The implementation of Suzuki et al. [2011] made use of the factor $1/(\rho g)$ between the dissipation rate ε and the source term. Therefore, similar steps are taken for the development of a new source term based on Jacobsen et al. [2019].

$$S_{ds,veg_J}(\sigma,\theta) = -\frac{1}{\rho g}D_{veg_J}(\sigma,\theta) \qquad [m^2] \quad (3.1)$$

In Suzuki et al. [2011] implementation, $E(\sigma,\theta)$ represent the matrix that is multiplied in every computational step and cell by the dissipation term. Therefore, we must conserve this term as an independent factor in the implementation of the new model. The surface spectrum (S_n) from Jacobsen et al. [2019] model is equal to the variance density spectra $E(\sigma,\theta)$ used in the matrix. Hereafter, these terms are exchanged for a clear comparison. For the present implementation, the option to define diverse vegetation characteristics in the vertical was not included because the validation data did not require it. Nevertheless, this could still be considered for a later upgrade after the present research. The possibility of defining different vegetation densities (N_v) over the horizontal spatial domain remains the same way as the existing version.

The formula has been divided into three parts, as shown in Eq. 3.2. The first term (outside the vertical integration) is the layer and frequencies independent term, which contains the parameters that do not depend on frequencies (e.g., density, vegetation diameter). The second term contains all factors that depend per frequency component within the vertical integration, in which σ and k represent the frequency and wavenumber of each component. In this term, the velocity profile experiences dissipation per frequency and elevation point. Finally, the surface elevation (or variance spectrum) is kept as independent, representing the SWAN energy matrix for source terms.

$$S_{ds,veg_J}(\sigma,\theta) = -\frac{1}{g}\sqrt{\frac{2}{\pi}}\alpha_u^3 C_D b_v N_v * \int_{-d}^{-d+h_v}\sqrt{m_{u,0}}(\frac{\sigma\cosh k(z+d)}{sinh(kd)})^2 dz * E(\sigma,\theta) \qquad [m^2] \quad (3.2)$$

The velocity spectrum is obtained through the surface elevation spectrum by multiplying it to the conversion factor defined in Equation 2.19. The surface elevation spectrum, with directional and spectral information, is obtained from the action balance density by multiplying it to σ^2. An additional σ is required for the first-order moment integration technique using the discrete logarithmic distribution of frequencies referred to in section 3.3 from The SWAN team [2019d]. Nevertheless, the surface elevation remains an independent term, and the wave components information (σ and k) only depends on frequencies. This causes the frequency-dependent dissipation rate to affect all directions of the same components evenly.

As described in Chapter 2, numerical integration is required to solve the formulation because no closed-form of the vertical integration has been identified. Therefore, the Simpson rule is used as an integral approximation. A small number of integration points are desired for a non-expensive computational subroutine but large enough to keep within the tolerances the approximation error. In the analysis from Jacobsen et al. [2019], 21 vertical points (20 layers) were sufficient for most of the applications. The required number of points increases with $k_p d$ and h_v/d. The decision of number points should be analyzed with engineering criteria on special projects that could require a different number of points. As a starting point, the implementation with 21 integration points was compiled and tested against other number of points, as shared in Appendix B. No significant differences were found to a lower number of points, concluding that the number of points could be reduced without a significant effect for most of the applications. Nevertheless, as no significant computational time was found between options, 21 points are kept for accuracy in the present version.

A numerical limitation in Fortran with the hyperbolic functions of the orbital velocities was found. This is a limitation present in computer models when calculating hyperbolic functions with very large numbers of the argument (kd and $k(d+z)$ in this case). To solve this, limiting the argument of the functions to a particular value could be sufficient (as done in other parts of the source code). Nevertheless, the ratio between sinh and cosh would be erroneously set to 1. Even though the deviations from the unity are small for large argument values, it was decided to follow another strategy and keep a physical representation of the velocity profile. To manage this, a conditional statement to determine the velocity for deepwater regimes was introduced. In other SWAN subroutines, the hyperbolic function's arguments are limited to 30, indicating that a threshold value of 20 should not represent a limitation for the code. This value is well within the deepwater regime and was analyzed after an investigation described in Appendix B.

$$\hat{u}_x = \omega a\frac{\cosh[k(d+z)]}{\sinh(kd)} \qquad\qquad kd \leq 20 \quad (3.3)$$

$$\hat{u}_x = \omega a e^{kz} \qquad\qquad kd > 20 \quad (3.4)$$

3.2. Evaluation in SWAN

For testing the new implementation, regular and irregular waves over a constant bottom are generated over a 500 m 1D domain. The model's differences identified in the previous research [Jacobsen et al., 2019] are expected to occur in the following analysis. To confirm these differences are conserved in the implementation, wave periods and vegetation height are varied. Other physical processes (e.g., wind growth, white capping, non-linear interactions) have been turned off in the model to compare only the dissipation models. The differences between models are evaluated through three methods. Their relevance depends on each case, but all together provide a good overview of the bulk and spectral differences between models.

- Visual Comparison

- Bulk Dissipation Ratio

- Performance Indicators

The bulk dissipation ratio for the present analysis is calculated by the total dissipation source term of Suzuki et al. [2011] over Jacobsen et al. [2019]. The bulk dissipation ratio is obtained from the SWAN output in the first cell where dissipation occurs. A comparison of the models' dissipation in the first cell guarantees that both models' performance depends on the same spectral input. Otherwise, the spectra evolve through the domain, and using other spatial grid cells would be comparing performances under different conditions. This ratio is envisioned to be comparable to the results from Figure 2.7, and is defined as:

$$\text{Ratio}_{ds,1} = \frac{S_{ds,veg_S}}{S_{ds,veg_J}} \qquad\qquad [-] \quad (3.5)$$

As the bulk dissipation is already analyzed with the bulk dissipation ratio, the spectral evolution caused by each model' is evaluated by looking at spectral characteristics (T_{m01} and T_{m-10}). The performance indicators Root Mean Squared Error (*RMSE*) and Mean Absolute Percentage Error (*MAPE*) are statistical parameters that indicate the degree of deviation between data against a reference. In the present analysis, the evaluation of the wave decay curve and mean period evolution are evaluated with:

$$RMSE = \sqrt{\frac{1}{n}\sum_{i=1}^{n}(x_{S,i} - x_{J,i})^2} \qquad\qquad (3.6)$$

$$MAPE = \frac{1}{n}\sum_{i=1}^{n}\frac{(x_{S,i} - x_{J,i})}{x_{S,i}} \qquad\qquad (3.7)$$

where

$$n = \text{number of data samples}$$
$$x_{S,i} = \text{value from Suzuki et al. [2011]}$$
$$x_{J,i} = \text{value from Jacobsen et al. [2019]}$$

The comparison model is based on a 1D model with 1 m constant water depth generating regular and irregular waves at the origin (0 m) of a 500 m domain. The length of the domain was chosen because reported vegetation lengths experiencing wave interaction are in the order of hundreds of meters. Tested periods ranged between 1.0 and 8.0 s, which under 1 m water depth registered values of $k_p d$ between 0.25 and 4.00. The wave amplitude was selected considering the wave steepness (H/L) when compared to observed waves in the field (average of 3.6% in deep water [Holthuijsen and Herbers, 1986]). The wavelength was computed from the dispersion relation $\omega^2 = gk\tanh(kd)$ using the peak frequency until convergence with two decimals. A constant incoming wave height of 0.10 m was selected for all tested periods. The degree of non-linearity was measured with the Ursell numbers ($N_{Ursell} = HL^2/d^3$), which depends on the wave height and length under the same depth. The non-linearity exceeded a N_{Ursell} of 30 for the 6 and 8 s waves, which is the recommended limit in Zhu and Chen [2017] for linear models and submerged vegetation. Because of this reason, no longer periods were explored in the present analysis. The boundary conditions and related characteristics used through the analysis are shared in Table 3.1.

d [m]	Regime	H_{m0}/d [-]	T_p [s]	$k_p d$ [-]	H_{m0}/L_p [-]	N_{Ursell} [-]
1	Deep	0.1	1.00	4.04	6.41 %	0.24
1	Intermediate	0.1	1.15	3.06	4.86 %	0.42
1	Intermediate	0.1	1.30	2.42	3.85 %	0.67
1	Intermediate	0.1	1.50	1.88	2.98 %	1.12
1	Intermediate	0.1	1.80	1.40	2.23 %	2.01
1	Intermediate	0.1	2.00	1.21	1.92 %	2.72
1	Intermediate	0.1	3.00	0.72	1.15 %	7.55
1	Intermediate	0.1	4.00	0.52	0.83 %	14.41
1	Intermediate	0.1	6.00	0.34	0.54 %	34.02
1	Shallow	0.1	8.00	0.25	0.40 %	61.49

Table 3.1: Reference boundary conditions for the implementation computational experiments with regular and irregular waves assuming a JONSWAP shape.

The model's vegetation properties, schematized as rigid canopies, are a stem diameter of 0.01 m, a drag coefficient equal to 1.0, and a density of 500 stems per area unit. The vegetation heights were varied to investigate the effect of relative submergence with values of h_v = 0.10, 0.25, 0.50, 0.75, and 1.00 m. All stem properties for explicit modeling are summarized in Table 3.2.

α	C_D	b_v	N_v	h_v
1.00	1.00	0.01 m	500 stems/m^2	{0.10, 0.25, 0.50, 0.75, 1.00} m

Table 3.2: Canopies properties for the implementation computational experiments with regular and irregular waves.

The spectral space was delimited by a lower limit of 0.03 Hz, as recommended by The SWAN team [2019a] (first frequency bin should be empty). The upper limit is set to 2.0 Hz as been used in the project from Figure 1.3. Typical values of the spectral and directional resolution for SWAN are df/f = 0.1 and 10 degrees per bin. Nevertheless, a spectral resolution equal to df/f = 0.01 was required to obtain a smooth spectrum in the irregular waves' visual comparison. The computational cost of this decision was very low (seconds-minutes for these simple cases), and the improvements to coarser values are disclosed in Appendix B. This analysis intends to reproduce the results from the 1D comparison of Jacobsen et al. [2019]. Therefore, it uses the most unidirectional setting in SWAN (2.0 degrees) with a resolution of 1.2 degrees per bin. This decision resulted in significantly larger computational time compared to the choice of spectral resolution. Following the recommendations from the The SWAN team [2019a], energy should not shift more than one spectral bin when propagating over one spatial grid. Therefore, for this academic testing with a high spectral and directional resolution, a high spatial resolution is required for accuracy reasons. The same discretization described in Table 3.3 is used for the regular and irregular wave comparison presented in the following sections.

3.2.1. Regular Waves

In this experimental phase, the range of wave periods in Table 3.1 were computed with each h_v, resulting in 50 runs per explicit model (Suzuki et al., 2011 and the new implementation). All other conditions are set as previously commented. The main variables are summarized in Table 3.4.

Regular waves were modeled by assigning energy to only one frequency bin. This causes all spectral characteristics (e.g. $T_p = T_{m01}$) to be equal and remain constant through the domain. Both models are based on a Morrison-type equation to determine the drag force of rigid canopies against the flow's orbital velocities. If

Spatial resolution	$\Delta x = 1$ m
Spectral resolution	$\Delta f/f = 0.01$
Frequency range	$0.03 \leq f \leq 2.00$ Hz
Directional resolution	$\Delta\theta = 1.2\,°$

Table 3.3: Computational discretization for the implementation computational experiments with regular and irregular waves.

T	{1.00, 1.15, 1.30, 1.50, 1.80, 2.00, 3.00, 4.00, 6.00, 8.00} s
h_v	{0.10, 0.25, 0.50, 0.75, 1.00} m

Table 3.4: Variables for the regular waves tests between the new implemented model and Suzuki et al. [2011].

the energy defines the velocity profile with one constant bin, both models should assign the same canopies dissipation rate. This evaluation investigates that the implementation has been done correctly. This is confirmed in the results from the present regular waves modeling campaign in which differences are not visually identified for the wave height evolution, as shown in Figure 3.1.
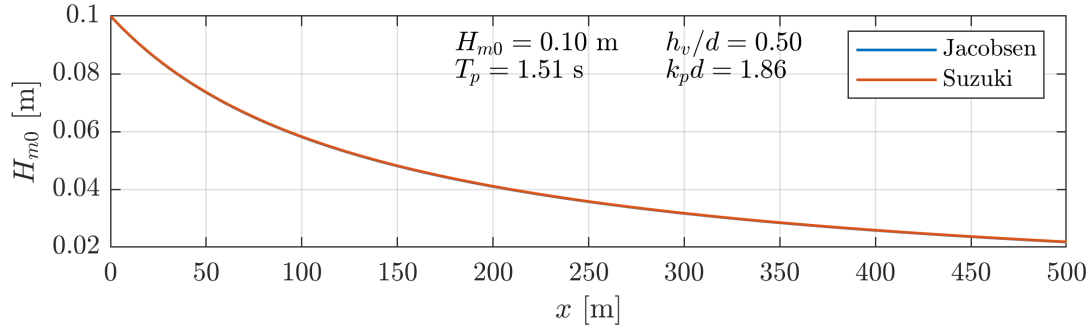
Figure 3.1: Wave height evolution through the spatial domain from model comparison with regular waves and boundary conditions $T =$ 1.5 s, $H = 0.1$ m, and $h_v/d = 0.50$.

The bulk dissipation ratio and performance indicators are used to visualize possible small differences. The deviations in the bulk dissipation ratio are smaller than 0.01, which are within the tolerance margin of numerical integrations. The deviations for the indicator parameters are not present for spectral characteristics as only a fixed period is present through the domain. For the wave height decay curves, the differences are smaller than 0.001 for *MAPE* and smaller than 0.0001 for *RMSE*. Therefore, it is concluded that both models are practically equal for regular waves and that the model is correctly implemented in SWAN.
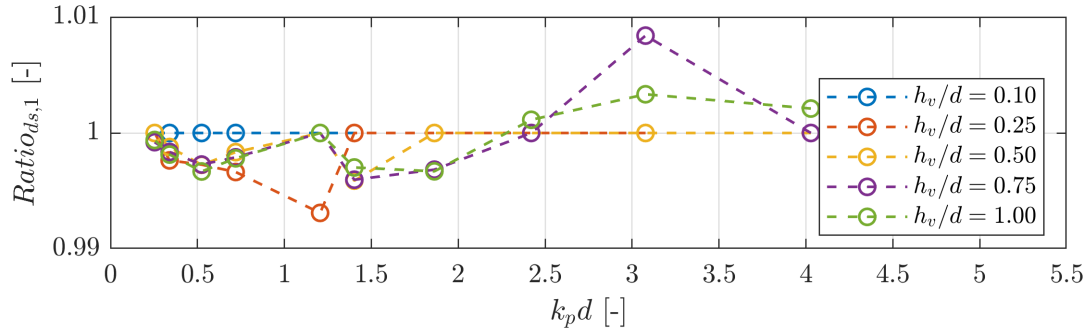
Figure 3.2: Regular waves total dissipation source term ratio at the first computational grid in SWAN from Suzuki et al. [2011] over the new model as a function $k_p d$ and h_v/d with $H = 0.1$ m.

3.2.2. Irregular Waves

Irregular waves were based on a JONSWAP spectrum with a peak enhancement factor γ equal to 3.3. The same ten reference periods from Table 3.1 are used and tested with five vegetation submergences. Other parameters have been explored to investigate the differences between models with changing spectral shape and wave heights. When other variables are modified and if no other indication is provided, the reference case with d =1.0 m, h_v = 0.50 m, H_{m0} = 0.10 m is used. These variables, which are summarized in Table 3.5, resulted in more than 100 runs per model. A numerical sensitivity analysis explores the effect of choices during the implementation and computational resolution during the experiments. The investigation over the number of integration points, the threshold for orbital velocities calculation of equation 3.4, and the discretization of space in SWAN are displayed in B.

T_p	{1.00, 1.15, 1.30, 1.50, 1.80, 2.00, 3.00, 4.00, 6.00, 8.00} s
h_v	{0.10, 0.25, **0.50**, 0.75, 1.00} m
JONSWAP γ	{1.0, **3.3**, 10.0, 100000.0}
H_{m0}/d	{**0.10/1.00**, 0.50/1.00, 0.40/4.00, 2.00/4.00}

Table 3.5: Variables for the irregular waves tests between the new implemented model and Suzuki et al. [2011]. Reference case in bold font.

For these computational experiments, spectral and bulk differences are expected. The newly implemented model is frequency-dependent, causing a change in the dissipation shape for different vegetation submergences and wave periods. The model from Suzuki et al. [2011], as discussed in Chapter 2, equally distributes the dissipation to the amount of energy on each spectral cell.
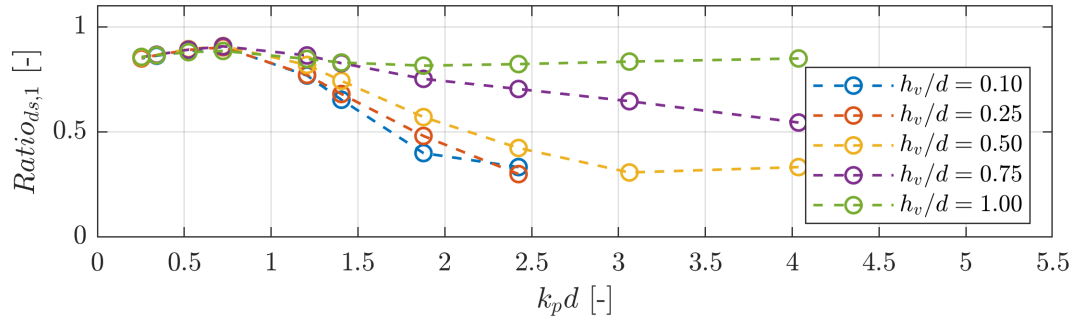
Figure 3.3: Irregular waves bulk dissipation ratio of Suzuki et al. [2011] over the new implementation with different values of periods and vegetation heights with γ = 3.3 and H_{m0} = 0.1 m.

The bulk dissipation of the new model was stronger in the first cell for all periods of the reference conditions. If Figure 3.3 is compared to the bulk dissipation ratio of Figure 2.7, differences are visible. The comparison between models from Jacobsen et al. [2019] shows that under emergent vegetation and small values of $k_p d$, the dissipation from Suzuki et al. [2011] should be stronger. The qualitative behavior is conserved, but an offset of the ratio is present. After an extensive investigation regarding this topic, it was concluded that the implementation of Suzuki et al. [2011] uses different spectral characteristics than documented. The mean frequency defined in the documentation follows from WAMDI Group [1988]:

$$\widetilde{\sigma}_{m-10} = (T_{m10})^{-1} = \left(E_{tot}^{-1} \int_0^{2\pi} \int_0^{\infty} \frac{1}{\sigma} E(\sigma,\theta) d\sigma d\theta \right)^{-1} \tag{3.8}$$

Within the implementation in SWAN, instead of the mean frequency defined by equation 3.8, the mean frequency according to the first order moment is used in SWAN version 41.31:

$$\widetilde{\sigma}_{m01} = (T_{m01})^{-1} = \left(E_{tot} \int_0^{2\pi} \int_0^{\infty} \frac{1}{\sigma E(\sigma,\theta)} d\sigma d\theta \right)^{-1} \tag{3.9}$$

This is confirmed by updating the plot from Figure 2.7 with the registered mean frequency in the implementation. In Figure 3.4 the bulk dissipation ratio of Suzuki et al. [2011] based on the mean frequency of equation 3.8 over Jacobsen et al. [2019] validates the present results.
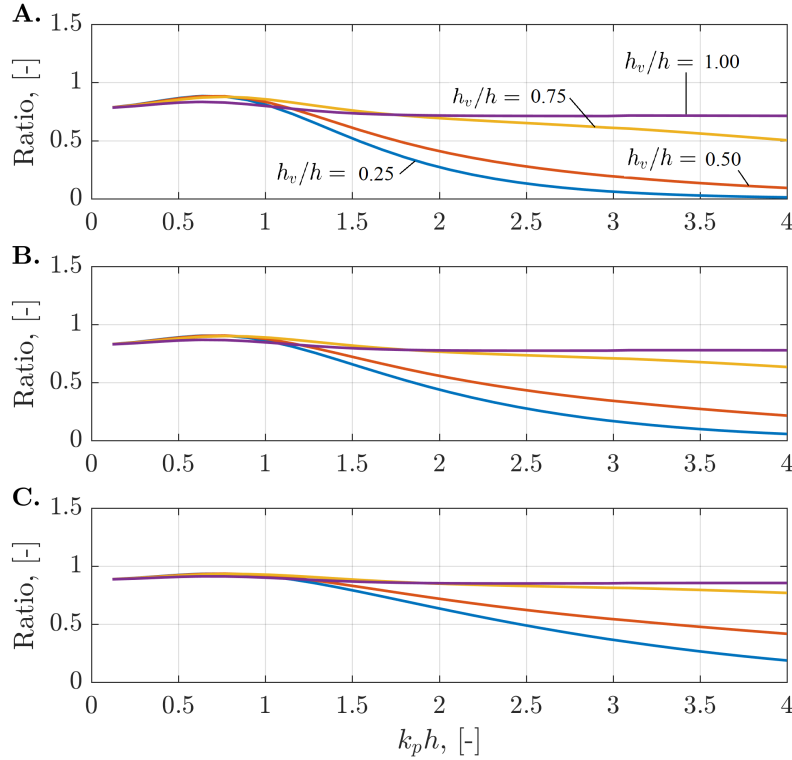

Figure 3.4: The ratio of the bulk dissipation from Suzuki et al. [2011] ($\widetilde{\sigma}_{m01}$) over Jacobsen et al. [2019] as a function the height of the vegetation for **A.** $\gamma = 1.0$; **B.** $\gamma = 3.3$, **C:**; and $\gamma = 10.0$. (Modified from [Jacobsen, unpublished])

The differences discussed in Chapter 2 remain, but the dissipation of the implemented model of Suzuki et al. [2011] is now smaller for all circumstances. The Ratio does not reach the unity in low values of $k_p d$ neither, as the linear dispersion is still not fulfilled between the characteristic wave number and frequency. The mean frequency $\widetilde{\sigma}_{m-10}$ gives more weight to low frequencies than $\widetilde{\sigma}_{m01}$. Therefore, for JONSWAP spectra defined by longer peak periods, the model of Suzuki et al. [2011] does not longer have a larger total dissipation. While the Ratio is unity for regular waves, emergent vegetation still differs for both models. Even though the vegetation is present in all the water column, Suzuki et al. [2011] will assign less dissipation to the low and mid-range frequencies if compared to Jacobsen et al. [2019]. Because more energy is present in this range of frequencies, the total bulk dissipation of Jacobsen et al. [2019] will be more significant than Suzuki et al. [2011] with the same drag coefficient.

The bulk dissipation of each model is evaluated in the wave height decay of the computational experiments. The energy decay of Jacobsen et al. [2019] is stronger than Suzuki et al. [2011] in the first meters of Figure 3.5, confirming previous discussions. Nevertheless, as the spectral shape evolves, the total energy in Suzuki et al. [2011] becomes lower. The distance in which the wave decay curves cross each other gets smaller with increasing periods and vegetation heights. There is a strong correlation between the magnitude of dissipation and these increasing factors. As each dissipation model assigns different dissipation per frequencies, the spectral shape is modified after being dissipated. The stronger dissipation in lower frequencies by Jacobsen et al. [2019] will eventually reduce the amount of low-frequency energy until the point where the spectra are less affected by submerged vegetation than compared to Suzuki et al. [2011]. The line-cross does not occur in cases with small dissipation because the length of the domain is not sufficient for the overlap to occur. If dissipation is increased by longer wave periods or higher vegetation, the lines could cross over more than once and conclude in similar total energy quantities. From this analysis, it is concluded that the drag

coefficients for each model will not depend only on the boundary conditions and vegetation properties, but also on the length of the domain.
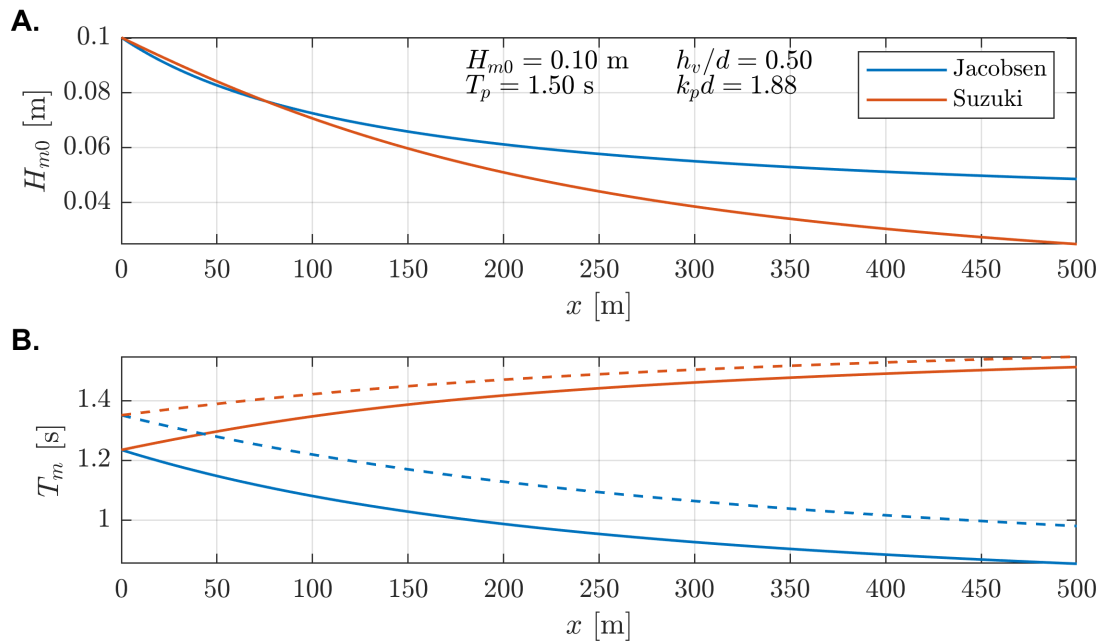
A.

B.

Figure 3.5: **A.** Wave height and **B.** Mean period (T_{m01} continuous line and T_{m-10} dashed line) evolution through the spatial domain from model comparison with irregular waves and boundary conditions $\gamma = 3.3$, $T_p = 1.5$ s, $H_{m0} = 0.1$ m, and $h_v/d = 0.50$.

In addition to the bulk differences, the spectra are studied by its characteristic periods. Between models, the mean periods evolve to opposite directions for submerged vegetation. The model of Suzuki et al. [2011] defines the dissipation of each component related to the velocity profile following linear wave theory. High-frequencies with high $k_p d$ remain in the model because its orbital velocities decrease rapidly with depth. Dissipation only occurs when orbital velocities interact with the canopies at each elevation point. If submerged vegetation is present, the velocities might be too small at the top of the canopy, resulting in low dissipation rates. This causes the mean period to evolve to smaller values for submerged vegetation. On the other side, the model of Suzuki et al. [2011] assumes an equally-distributed dissipation defined by T_{m01}. This representation of the velocity profile causes stronger orbital velocities than the new model for high-frequencies. The opposite occurs for low-frequency energy. Even though long components experience shallower conditions than the mean frequency, the model of Suzuki et al. [2011] assumes an equal velocity profile for all frequencies, underestimating the dissipation at those components. This is observed in Figure 3.6. For emergent vegetation, both models' mean periods increase. This is caused because the short components orbital velocities are maximum at the water surface, where they interact with emergent vegetation.

Mean periods (e.g., T_{m01}, T_{m-10}) are used for the comparison instead of the peak period because the peak evolution changes radically at one point. Once the energy at the peak frequency is lower than energy conserved in high frequencies, a secondary peak on high frequencies takes over the definition of peak frequency. This occurs in cases with significant dissipation and submerged vegetation. The other cases did not experience enough dissipation to allow the secondary peak to take over within the spatial domain length. The energy decay at the peak frequency and the development of a secondary peak can be observed in Figure 3.6.

All other dissipation processes were turned off, leaving the vegetation as the only cause for the energy decay. The spectral distribution of the energy decay is obtained by subtracting the first cell's spectra where dissipation occurs (1 m) from the one in origin (0 m). If this same subtraction is done between other points of the domain, the shape would not any longer be attached to the incoming boundary condition because the spectra already evolved differently for each model. The group velocity c_g is on the left side of the action balance equation, while the source term is in the right. Therefore, the spectral energy decay ΔE is not equal to the dissipation shape distribution. Nevertheless, the same qualitative behavior can be observed when

comparing it to Figure 2.8. The peak frequency of the spectra at the origin is plotted to be compared to the peak energy decay.
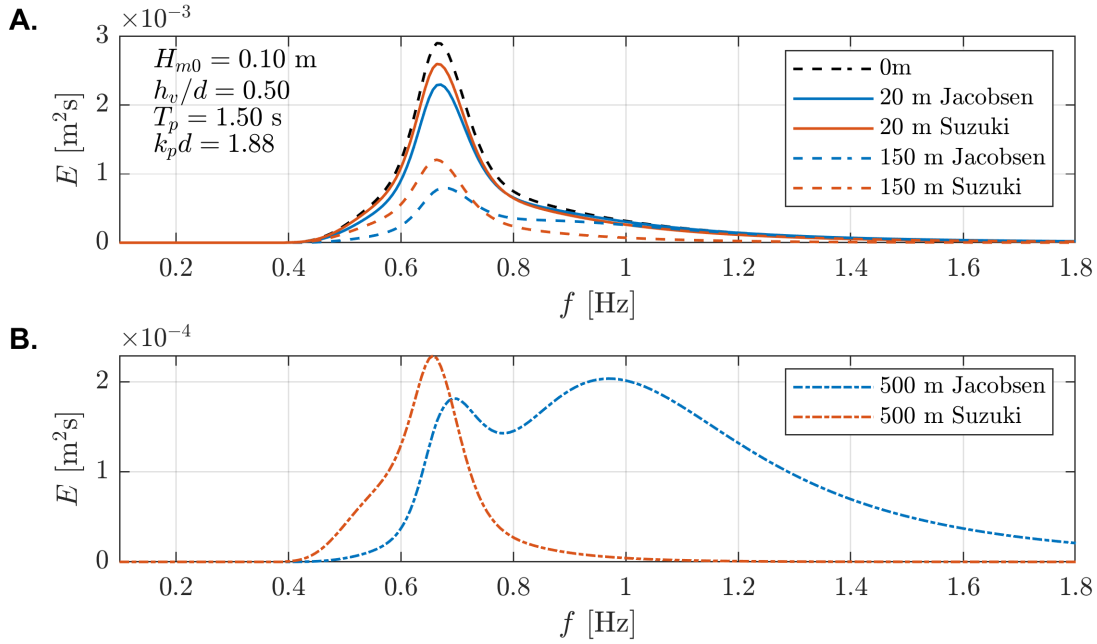

Figure 3.6: Spectral comparison at the end of the spatial domain with irregular waves and boundary conditions $\gamma = 3.3$, $T_p = 1.5$ s, H_{m0} = 0.1 m, and $h_v/d = 0.50$.
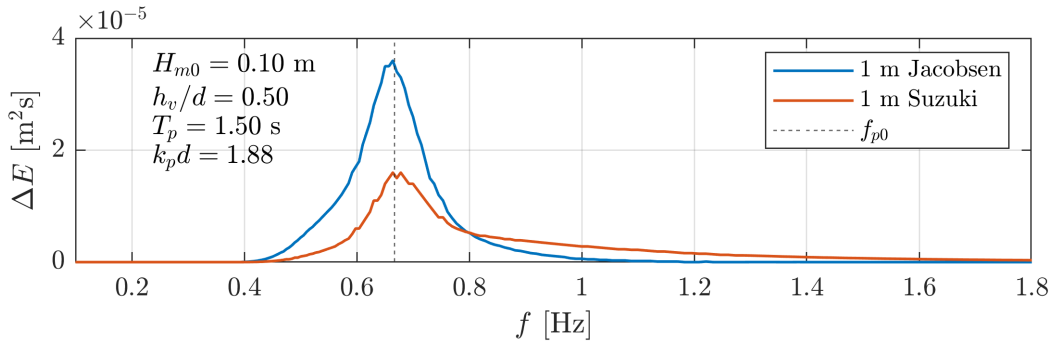

Figure 3.7: Spectral dissipation comparison at the beginning of the domain with irregular waves and boundary conditions $\gamma = 3.3$, $T_p = 1.5$ s, $H_{m0} = 0.1$ m, and $h_v/d = 0.50$.

The energy decay shape confirms the previous discussions, where the dissipation of short components is stronger and of long components weaker by Suzuki et al. [2011] than by Jacobsen et al. [2019]. The decay shape of Suzuki et al. [2011] remains close to the peak frequency of the incoming spectra, while Jacobsen et al. [2019] shifts slightly to low frequencies, as discussed in Chapter 2 by Jacobsen et al. [2019].

The most substantial period evolution differences between models are observed when dissipation is stronger, especially when vegetation is close to the water surface. Nevertheless, once the vegetation reaches emergence, the wave heights and period curves have the same evolution as displayed in Figure 3.8. The models will behave similarly with emergent vegetation, but a small spectral difference will remain. With the model from Jacobsen et al. [2019], the high frequencies are mainly only affected by the upper part of the emergent vegetation, while in Suzuki et al. [2011] these frequencies are affected by a larger part of the vertical related to the characteristic mean frequency that defines the velocity spectrum.

The overall effect of model choice on the energy distribution at the end of the domain is evaluated with the performance indicators, as shown in Figure 3.9. Most significant differences are observed for smaller values
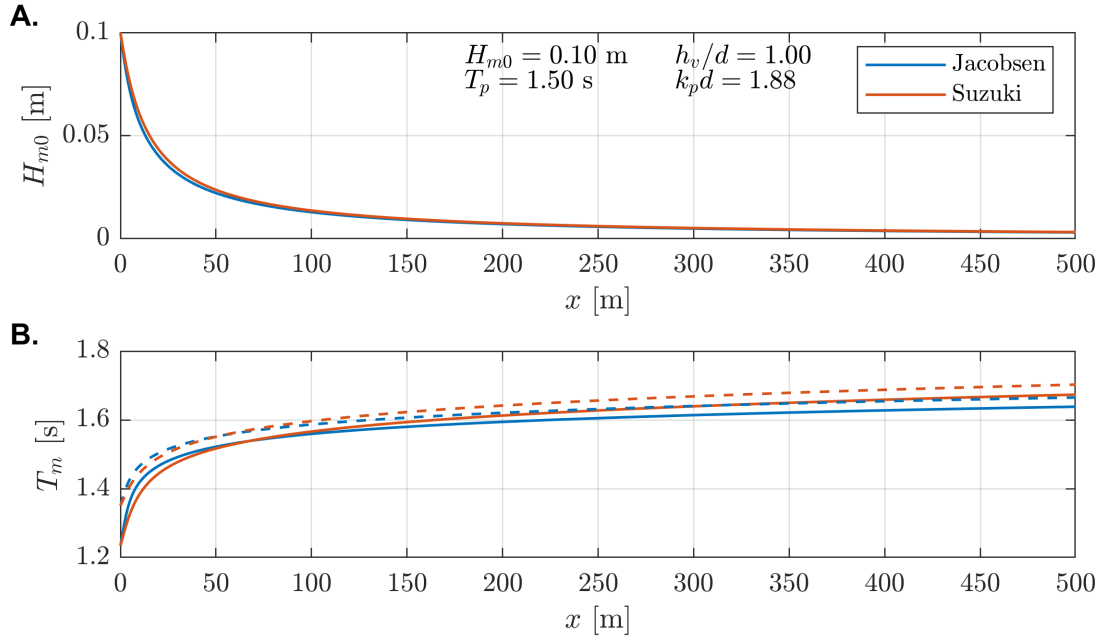
Figure 3.8: **A.** Wave height and **B.** Mean period (T_{m01} continuous line and T_{m-10} dashed line) evolution through the spatial domain from model comparison with irregular waves and boundary conditions T_p = 1.5 s, H_{m0} = 0.1 m, and h_v/d = 1.00.
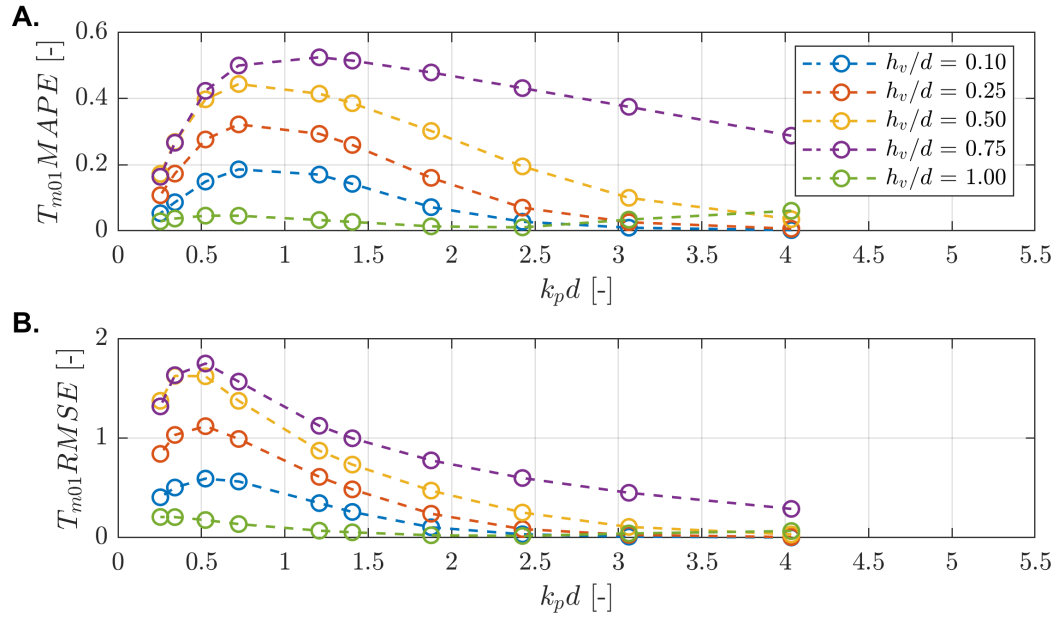

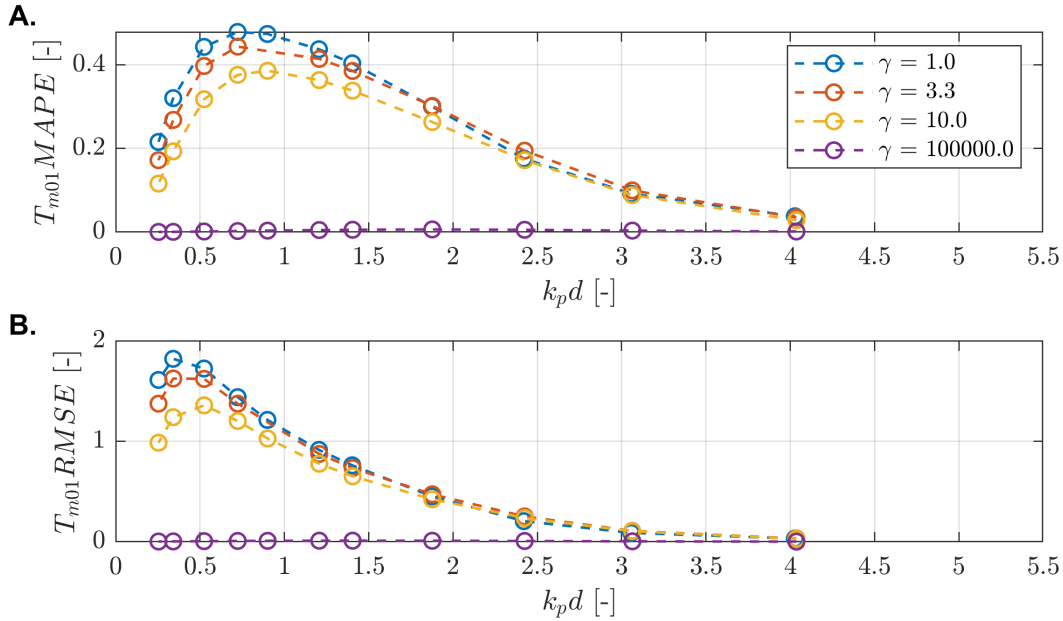Figure 3.9: Irregular waves statistical indicators (**A.**) *MAPE* and (**B.**) *RMSE* for the mean period evolution through the spatial domain using different vegetation heights with γ = 3.3 and H_{m0} = 0.1 m.

of $k_p d$ and vegetation heights close to the water surface. This agrees with the discussion about submergence and high-frequency components. Near emergence gives larger relative weights to high frequencies on the mean period evaluation, causing a significant change to high frequencies in the new model. This finding highlights the importance of model choice for low $k_p d$ values present in high energy events like storms.

Spectral Shape

From the publication of Jacobsen et al. [2019], it is expected that different spectral shapes change the performance of both models. Consequently, the peak enhancement factor γ of the JONSWAP spectrum is varied with values {1.0, 3.3, 10.0, 100000.0} using the reference parameters (d = 1 m, h_v = 0.50 m, H_{m0} = 0.1 m). The last value of the peak enhancement factor is so large that it is intended to be close to the definition of regular waves in which differences should be negligible, as confirmed below. A smaller γ means wider spectra, which enlarges the bulk and spectral differences between the models. These can observed in Figures 3.10 and 3.11. The sensitivity of the spectral change affects both high and small values of $k_p d$.
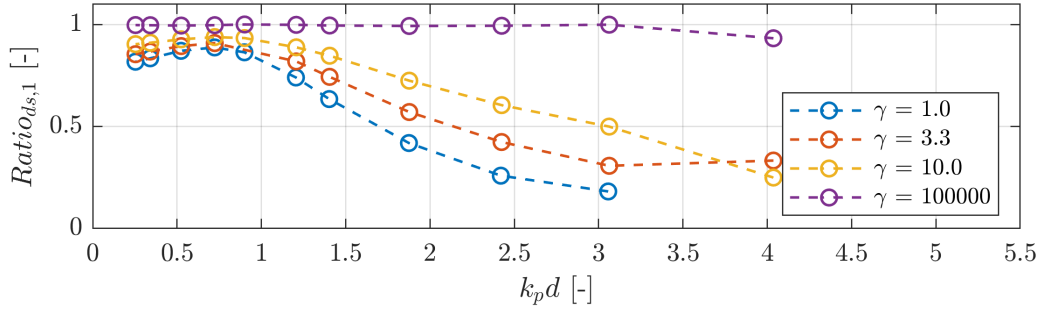
Figure 3.10: Irregular waves bulk dissipation ratio of Suzuki et al. [2011] over the new implementation with different values of periods and γ with h_v/d = 0.50 and H_{m0} = 0.1 m.

Figure 3.11: Irregular waves statistical indicators (**A.**) *MAPE* and (**B.**) *RMSE* for the mean period evolution through the spatial domain using different values of γ with h_v/d = 0.50 and H_{m0} = 0.1 m.

The bulk dissipation ratio gets closer to the unity for larger values of γ. A narrower spectrum reduces the effect of defining the velocity spectra by a characteristic frequency, as energy gets closer to the peak. The inverse is observed in Figure 3.12, where γ = 1.0 amplifies the spectral differences between models.

The differences between models for different peak enhancement factors with the same JONSWAP properties (T_p, H_{m0}) are significant for large scale modeling. The choice of models will enlarge for broader spectra. The example provided in the problem statement shows a wide distribution of energy, where substantial differences are expected between models. As discussed in the previous analysis, small differences in the bulk
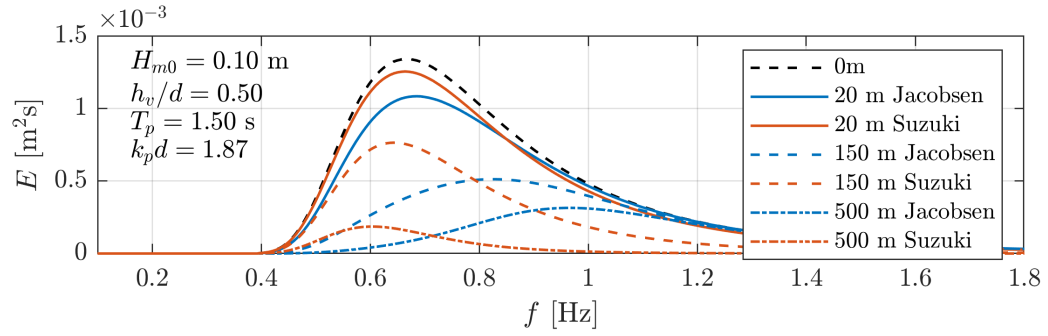
Figure 3.12: Spectral comparison at the end of the spatial domain with irregular waves and boundary conditions $\gamma = 1.0$, $T_p = 1.5$ s, H_{m0} = 0.1 m, and $h_v/d = 0.50$.

dissipation ratio but experiencing strong dissipation cause substantial differences at the end of the spatial domain.

Wave Heights and Depths

Experiments with an increase in wave height and water depth are explored to compare the sensitivity of the model to conditions more similar to a storm. Four conditions are computed to investigate this: wave heights of 0.10 and 0.50 m over the initial water depth (1 m), and waves of 0.40 and 2.0 m over 4.0 m water depth. The comparison results in two wave height to depth ratios (H_{m0}/d = 0.10 and 0.50) but defined by different variables. Even though the ratio of wave height and depth remains in some cases, differences are expected because these conditions modify the $k_p d$, wave steepness, and non-linearity. Small periods were not computed to maintain the steepness below the maximum observed value of 14% previously discussed. As these are randomly generated waves, some components might exceed this threshold. In order to exclude differences by vegetation relative submergences (h_v/d), the vegetation was set to $h_v = 2.0$ m when the water depth is 4.00 m (keeping $h_v/d = 0.50$). The tested conditions are summarized in the Table 3.6.

$H_{m0}/d = 0.10/1.00$	$T_p = \{1.00, 1.15, 1.30, 1.50, 1.80, 2.00, 3.00, 4.00, 6.00, 8.00\}$ s
($H_{m0}/d = 0.10$)	$k_p d = \{4.04, 3.06, 2.42, 1.88, 1.40, 1.21, 0.72, 0.52, 0.34, 0.25\}$
	$H_{m0}/L_p = \{6.41, 4.86, 3.85, 2.98, 2.23, 1.92, 1.14, 0.85, 0.55, 0.40\}$ %
$H_{m0}/d = 0.50/1.00$	$T_p = \{1.80, 2.00, 3.00, 4.00, 6.00, 8.00\}$ s
($H_{m0}/d = 0.50$)	$k_p d = \{1.40, 1.21, 0.72, 0.52, 0.34, 0.25\}$
	$H_{m0}/L_p = \{11.16, 9.61, 5.70, 4.23, 2.77, 2.00\}$ %
$H_{m0}/d = 0.40/4.00$	$T_p = \{1.50, 1.80, 2.00, 3.00, 4.00, 6.00, 8.00\}$ s
($H_{m0}/d = 0.10$)	$k_p d = \{7.51, 5.62, 4.83, 2.89, 2.10, 1.36, 1.01\}$
	$H_{m0}/L_p = \{11.39, 7.91, 6.41, 2.98, 1.92, 1.15, 0.83\}$ %
$H_{m0}/d = 2.00/4.00$	$T_p = \{4.00, 6.00, 8.00\}$ s
($H_{m0}/d = 0.50$)	$k_p d = \{2.10, 1.36, 1.01\}$
	$H_{m0}/L_p = \{9.59, 5.75, 4.17\}$ %

Table 3.6: Tested periods with their values for $k_p d$ and steepness for the irregular waves tests between the new implemented model and Suzuki et al. [2011] with different values of wave height and water depth using $\gamma = 3.3$ and $h_v/d = 0.5$.

The bulk dissipation ratio and statistical indicators of the mean period evolution indicate the differences to these conditions, as displayed in Figures 3.13 and 3.14. The dissipation of one model might be equal to

zero under large values of $k_p d$. The same was observed in small periods with h_v/d. In those cases, the ratio is not plotted in the results.
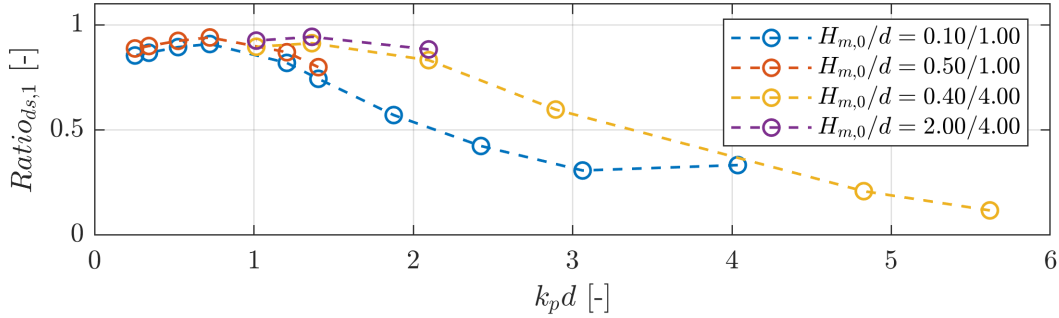

Figure 3.13: Irregular waves bulk dissipation ratio of Suzuki et al. [2011] over the new implementation with different values of periods, wave heights and water depths with $\gamma = 3.3$ and $h_v/d = 0.50$.

The most considerable bulk differences between wave height and depth ratio were found for values of $k_p d$ between 1.5 and 3.5. The cases with the same H_{m0}/d value but defined by different conditions show small differences. These are attributed to different incoming energy and steepness. More bulk energy is provided with higher and steeper significant wave heights, which results in other velocity profiles and distributed dissipation. If the cases with different wave height are compared under the same water depth, the initial wave height and the rate of wave height decay differ. Higher waves are translated into more dissipation. Stronger dissipation with submerged vegetation causes the mean periods evolution curves to increase their total difference as observed in the performance indicators from Figure 3.14.
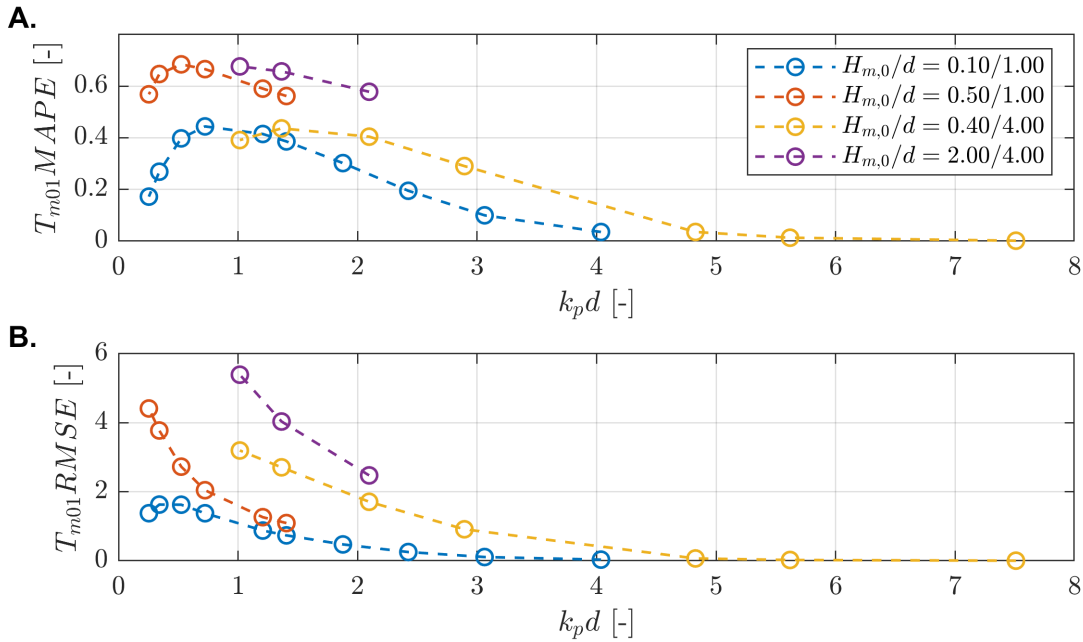

Figure 3.14: Irregular waves statistical indicators (**A.**) *MAPE* and (**B.**) *RMSE* for the mean period evolution through the spatial domain using different values of wave heights and water depths with $\gamma = 3.3$ and $h_v/d = 0.50$.

An increase in the differences is observed for larger wave heights with the same water depth, as larger incoming energy causes more dissipation for the same h_v/d. Nevertheless, for large wave heights with larger depth, the differences in *MAPE* seem to remain in the same order of magnitude but with an offset. The *MAPE* are shifted to larger $k_p d$ values. This is caused by more energy in the defined spectra by the same peak period, which results in larger model differences by the same T_p. These differences are clearly visible in *RMSE*. A

unique point provides a smaller value of *MAPE* for $k_p d$ = 1. The Ursell number for this case is 312, leading to a very large non-linearity outside of both models' valid assumptions.

3.3. Discussion

The newly implemented model assigns the dissipation to the energy matrix from SWAN, which has the frequency and directional information. Nevertheless, the wave components to obtain the multiplication factor of this matrix in SWAN subroutines (k, σ) depend only on frequencies. Therefore, it is assumed that the frequency distributed dissipation is evenly distributed in all directions. This might create differences from measurements on the field where components travel freely in all directions. It is recommended to research the implication of this decision further, and if significant, incorporate it in SWAN.

The in-canopy velocity reduction factor α_u is assumed to be 1.0, as done in the analysis from Jacobsen et al. [2019]. This was done to compare the model differences, excluding this coefficient that was not included in previous models. As mentioned in Jacobsen et al. [2019], this factor was nearly frequency-independent. If included as a constant factor, the bulk dissipation ratio between models might change the value but not its qualitative behavior and physical explanation.

Besides, the absolute frequency ω described in Jacobsen et al. [2019] was substituted by the relative frequency σ, as SWAN works with this parameter. The consideration of current interaction and the use of σ is not commented in the publications of Mendez and Losada [2004] and Suzuki et al. [2011]. The effect of currents on the wave energy dissipation due to implicit modeling (bottom friction) are not taken into account in SWAN either. As discussed in Chapter 2, the presence of currents can either increase or decrease the dissipation over vegetation. The main reason for this changing behavior is the velocity ratio between waves and currents [Hu et al., 2014]. During the present project, no experimental data to isolate and research this phenomenon is performed. It is recommended further to research the interaction of currents with the explicit models.

The possibility to vary vegetation properties horizontally is conserved in the new implementation, but their definition in vertical segments is not as it was not required for the present research. Nevertheless, this could be incorporated in upcoming versions if required. In both explicit models, flexibility is only included within the valid region of the canopies approach. The effect of this assumption on highly flexible vegetation is investigated with the field measurements.

A difference in the model of Suzuki et al. [2011] between documented (σ_{m-10}) and implemented mean frequency (σ_{m01}) was discovered from this analysis. The bulk dissipation ratio from Jacobsen et al. [2019] was updated with this parameter, resulting in comparable results to the present implementation analysis. Even though the mean frequency in the implementation is different, the used wave number and mean frequency do not fulfill the linear dispersion relation. Obtaining the frequency via the dispersion relation from the wavenumber would fulfill the linear dispersion and reach a ratio of 1.0 for shallow water conditions [Jacobsen et al., 2019]. This will improve the similarity of bulk dissipation for both models, but the spectral differences will remain. In addition and if updated, the large number of drag coefficients and empirical formulations based on Suzuki et al. [2011] would not hold anymore. This could confuse users who would need to be aware of this update and the validity of previous research, to avoid errors. Therefore, it is recommended to update the official SWAN version with the new formula if proven to be a significant improvement.

The dissipation from the new model was always stronger than Suzuki et al. [2011] in the first cell. Nevertheless, throughout the distance of the domain, the bulk dissipation ratio changes between models. This results in not exchangeable drag coefficients as they depend not only on the physical representation of the stem but on different velocity profiles and length of the vegetation field. The calibration of the drag coefficient and differences in are discussed in the validation against measurements.

The energy distribution of both models throughout the 500 m is evaluated with the mean period statistical indicators. The results highlighted the importance of model choice in the spectral shape for $k_p d$ values between 0.25 and 1.50. Even though small bulk ratio differences are present for those values, small spectral differences are multiplicative factors of the dissipation present, which increases for longer components and higher vegetation. Also, visual observations concluded that the most considerable spectral differences at the end of the domain (from the reference case in Table 3.1) were observed for $k_p d$ values between 1.50 and 3.00. This as a result of the second peak in high frequencies by the new model. This was not observed in Suzuki et al. [2011] results in which high-frequency energy is dissipated for all submergences. The findings from the

present chapter summarize that model choice becomes relevant for bulk and spectral analysis under almost all $k_p d$ tested periods for submerged vegetation.

The spectral shape was investigated by modifying the peak enhancement factor γ. Largest differences are observed for a wider spectrum as the new model's frequency distributed dissipation becomes more relevant. Broad spectra are often present in storms [Chen and Zhao, 2012], condition out of the narrow banded spectrum assumption (Rayleigh invariant) in the model of Mendez and Losada [2004] and Suzuki et al. [2011]. Different incoming wave energy levels in different water depths investigate the model's comparison under conditions closer to a storm. It was concluded that the incoming spectra (total energy and shape) are relevant for the model choice. The validation of each model to experimental and field data is investigated in the following chapters.

4

Validation with wave flume experiments

In this Chapter, the model setup and measurements for the wave flume validation are described. The experiments will work as the first validation for the newly implemented model against measurements. The model from Jacobsen et al. [2019] has already been validated against experimental data, as discussed in Chapter 2. Nevertheless, the present validation is of high value because of three main reasons. First, the model implemented in SWAN has not been validated against measurements. Secondly, a larger ranger of wave periods, heights, and submergences than the validation in Jacobsen et al. [2019] is here presented. Finally, this phase will provide a performance comparison between implicit and explicit models under controlled conditions, not found in the literature. The implicit model from Collins [1972] and the explicit model from Suzuki et al. [2011] are compared to the new implementation. The bottom friction model from Madsen et al. [1988] could not simulate the strong dissipation by canopies in the present analysis and is not included in the results. The reasons for the limitations are discussed in this report. The other dissipation processes have been turned off in SWAN as they were not relevant in the experiments. The boundary conditions were set as target values defined in the MetaData, but differences to the measurements were found. Therefore, the measured spectrum before the canopies was provided as a boundary condition to reduce the initial mismatch. The effect on these differences is discussed in Appendix C.

4.1. Experimental Campaign and Data

The data was generated through experiments performed at the U.S. Army Engineer Research and Development Center in Vicksburg, Mississippi, resulting from the collaboration between the USACE-ERDC, Rijkswaterstaat, and Deltares. A wave flume of 45.7 m long, 1m wide, and 1 m deep was equipped with a wave paddle from HR Wallingford. The reference system considers the wave generator as the origin, starting with 0 m in the horizontal axis and ending at 40 m where a wave dampener was installed to reduce wave reflection. An overview of the flume layout can be observed in Figure 4.1.
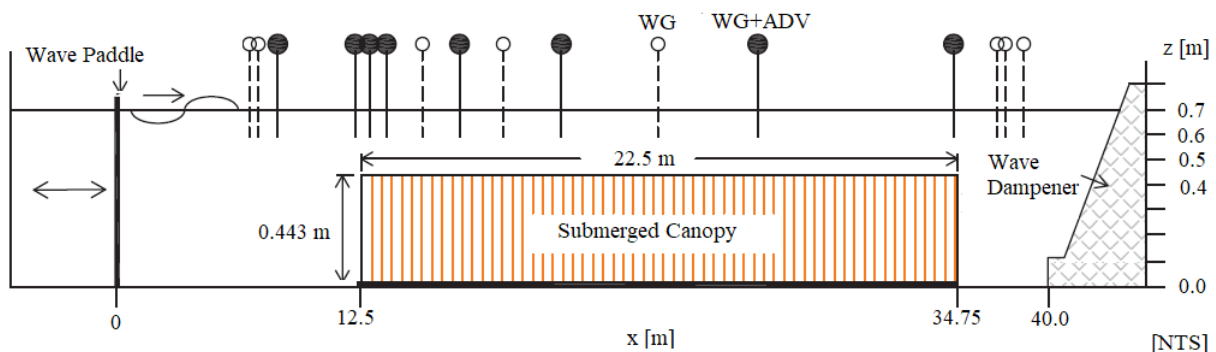

Figure 4.1: Cross section from the wave flume experimental campaign with indicative dimensions using the same reference system than the present validation. Hollow circles indicate a wave gauge (WG) location and the filled circles indicate a wave gauge with an additional Acoustic Doppler Velocimeter (ADV). (Modified from *[McFall et al., In preparation]*). Dimensions Not to Scale [NTS].

The vegetation was schematized as rigid cylinders made of wood with 9.5 mm in diameter and 44.3 cm in height. They were placed over a 2 cm piece of plywood that reduced the relative submergence at that point. On top of it, a density of 625 stems per m^2 with a staggered stem array. The canopies patch length was 22.25 m long, starting 12.5 m until 34.75 m from the wave paddle. The vegetation height remained constant throughout the experiments, but different water levels investigated the effect of h_v/d.

The experimental campaign's objective focus was other than the present research. The campaign sought to collect the wave height decay, local velocity field through the canopies, the organized shear stresses, and the Lagrangian Stokes drift. Because of this, wave gauges (WG) and additional Acoustic Doppler Velocimeters (ADV) were installed at some stations. For the present investigation, the water surface elevation from WG data is more than enough to compute the wave properties and variance density spectrum. The 16 WG were positioned at x[m] = {8.33, 8.66, 9.39, 12.26, 12.80, 13.44, 14.78, 16.17, 17.79, 19.96, 23.57, 27.28, 34.58, 36.21, 36.51, 37.20} (all significant ciphers for their location can be accessed in the project metadata).

Regular and irregular waves were generated in this experimental campaign, but only the irregular waves are used for the present analysis as the spectral mismatch is the core of the research. The water level started on 0.7 m, as described in Figure 4.1, with local relative submergence of $h_v/d = 0.65$ (including the reduction of depth by the plywood). The water level was later lowered to three other different levels (0.6, 0.5 and 0.4 m) resulting in $h_v/d = 0.76, 0.92$ and 1.17 respectively. This last set of experiments are executed with canopies emerging 6.3 cm over the still water level. Different significant wave heights with levels between 3.76 and 9.5 cm were registered, meaning that higher waves than 12.6 cm could exist and experience part of their crest above the canopies, adding other effects like a possible increase in Stokes drift. The same could happen for the cases with near emergence in which the wave valley could experience vegetation emergence. If existent in the data, this effect is not further analyzed in the present research. Target peak periods range from 1.1 to 2.1 s, creating a group of 21 experiments for the present research.

The water surface elevation data was processed to compute the spectrum at each of the wave gauges. Waves smaller than 2 mm were neglected from the process to reduce instrument noise in the analysis. After testing other values, the equidistant frequency resolution used in the spectral processing is $df = 0.035$. The experiments contain four repetitions of a $\sim 210 T_p$ irregular wave signal (each test is $\sim 840 T_p$ long). The signal is not truly random because it repeats after ~ 250 waves due to the different objectives with which the experiments were executed. The original study aimed to measure the velocity field over the vertical at a specific moment of the time series, choosing to repeat the signal for that purpose. Even substantial differences between neighboring frequencies cause the bulkiness of the spectrum. It resulted in being enough for this analysis. A discussion over the spectral resolution is shared in Appendix C.

4.2. Model Validation and Comparison

The ratio between the width and length of the wave flume allows us to schematize the experiments in a unidirectional study. The 1D model in SWAN uses cartesian coordinates to define a spatial grid of 40 m starting at the wave paddle (0 m) and ending in the wave absorber. The most unidirectional directional spreading setting in SWAN (2 °) is computed with a resolution of 1.0 °. Using the standard directional setting in SWAN (31.5 °) resulted in artificial spreading with values up to 0.3 cm for an incoming wave height of 7.3 cm. The canopies' presence is represented by an input grid file with values equal to one in cells where canopies are present, and equal to zero where not. Following the same reasoning as Chapter 3, high resolution in space and frequencies were chosen as significant energy variance is observed in space and frequencies. The model uses the same frequency bins as the measurements spectral processing and boundary condition between 0.03 and 2.00 Hz. The resolution in SWAN considers the frequencies' logarithmic scale, refining the spectral resolution in high frequencies. The values of the discretization are shared in Table 4.1.

The initial boundary conditions for the model validation were based on the target spectrum during the experimental campaign, a JONSWAP spectrum with certain T_p and H_{m0}. Nevertheless, it was found that the measured spectrums before the canopies presented differences than the target JONSWAP spectrum described in the metadata. The four WG before the canopies show differences due to possible wave reflection. Therefore, WG 04 was initially discarded for this reason. Between WG 01 - 03, it was observed that the second and third instruments collected a more consistent amount of energy than the decay curve. For the present results, the WG 02 data was selected as the boundary conditions. The effect of different spectra at the origin is discussed in Appendix C. All other physical processes were deactivated from the wave model. This decision has been validated by one of the authors of the experimental campaign, which confirms that no wave

Spatial resolution	$\Delta x = 1$ cm
Spectral resolution	$\Delta f / f = 0.035$
Frequency range	$0.03 \leq f \leq 2.00$ Hz
Directional resolution	$\Delta \theta = 1.0\,°$

Table 4.1: Computational discretization for the model based on the wave flume experiments.

breaking and white-capping were observed. As the waves are assumed unidirectional, the wave-wave inter-
actions are assumed not to be dominant, but it is recommended to research further the interaction of these
mechanisms with the dissipation models.

Each combination of water depth, wave heights, and periods cause a different set of hydrodynamic con-
ditions, which will affect the drag coefficient values of both models. As commented previously in Chapter
2, this will result in different drag coefficients between runs and models. As a starting point, the coefficients
were set to 1.0 for CD (= $\alpha^3 CD$ for this comparison) of the explicit models (Suzuki et al., 2011 and the new
implementation), C_b ([cfw] in SWAN) of Collins [1972], and k_s ([kn] in SWAN) of Madsen et al. [1988]. This
resulted in an uncalibrated preliminary result with an overall wave height decay not matching the measure-
ments. An example is shared below in Figure 4.2. Before calibration and between explicit models, the model
from Suzuki et al. [2011] showed stronger dissipation in most of the cells. A similar result was observed in the
previous Chapter, were the dissipation at the first cell shows stronger bulk dissipation by the new model but
overtaken by Suzuki et al. [2011].
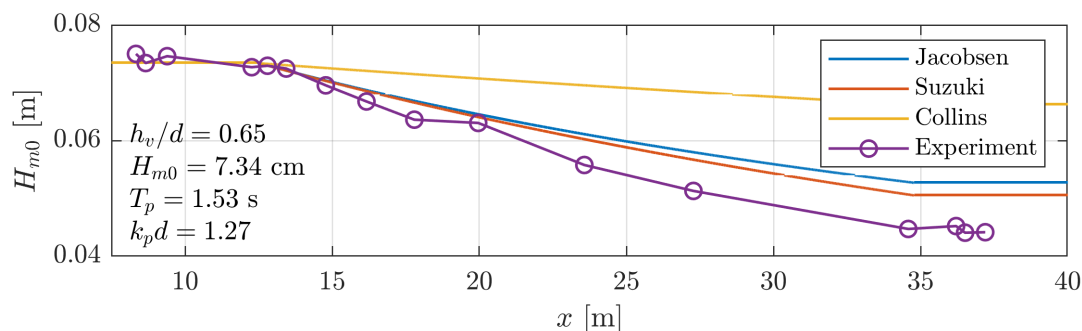
Figure 4.2: Uncalibrated significant wave height evolution through the spatial domain including experimental data and model
comparison with boundary conditions T_p = 1.53 s, H_{m0} = 7.34 cm, and h_v/d = 0.65.

From the calibration process, Madsen et al. [1988] shows some limitations under the experimental con-
ditions. It was observed that the formulation writes *"error in iteration fw: Madsen formulation"* stopping the
computations from SWAN if the same vegetation input grid was provided. This problem was investigated
through internet forums, finding similar questions by SWAN users without a clear answer. From discussions
with the SWAN team, it resulted that [kn] appears somewhere in the denominator in the iteration process.
The SWAN team solved this by releasing a patch for the current SWAN version during the last phase of this
thesis. This can also be solved by providing an input file that exchanges the 0 values (where vegetation is not
present) to a minimal number (e.g., 1x10^{-6}). Besides, Madsen et al. [1988] could not be calibrated because
the model in SWAN cannot reproduce strong values of dissipation. This model was developed for bottom
friction, and h_v/d values larger than 0.65 are outside of its capabilities. Therefore, Madsen et al. [1988] is not
included in the results of this Chapter. Implicit modeling was represented by Collins [1972], which was able
to simulate stronger total dissipation for most of the experimental campaign cases.

The calibration target was an overall good fit of the wave decay curves, aiming primarily to match the wave
height after the canopies. The objective behind the calibration is to compare the models' spectral differences
with the same bulk dissipation at the end of the domain. The significant wave height after the canopies
(WG14-16) were averaged and compared to the models, with deviations smaller than 2x10^{-4} m for all cases
except for one. Experiment IR31 with Collins [1972] model could not reproduce the dissipation as marked in

Table 4.2 and displayed in Figure 4.3.A. This case is not included in Figure 4.3.B as small differences would not be appreciated for the rest of cases.
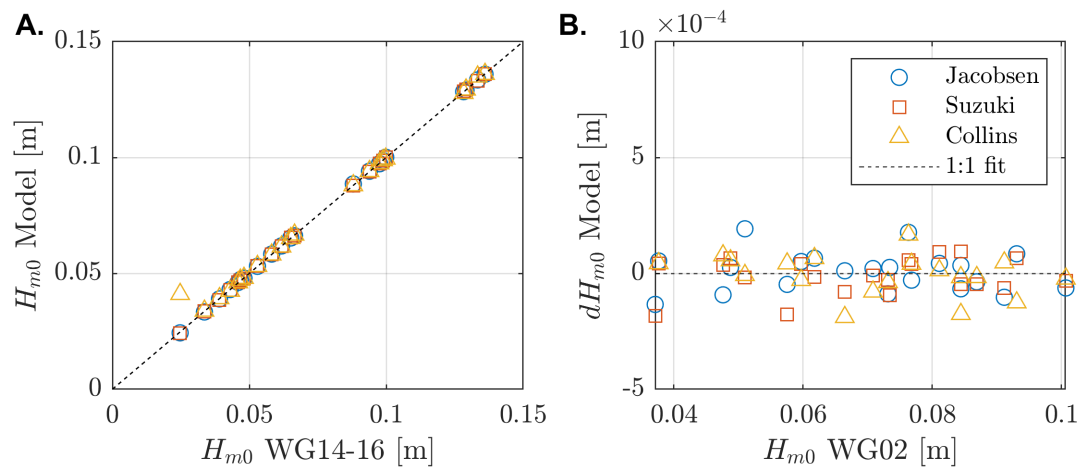

Figure 4.3: **A.** Significant wave height for the tested models and experiments after the canopies by averaging results at WG14-16. **B.** Difference between average significant wave height after the canopies (WG14-16) of the models to the experiments in the vertical, compared to the wave height at the boundary condition (WG02).

Table 4.2: Experiments, their wave parameters, and calibration coefficients per water level. Significant wave height and peak period are included for * Target values described in metadata, and **Boundary Conditions used during SWAN modeling.

Water Level 0.70 m

ID	h_v/d	$H_{m0}*$ / $H_{m0}**$	T_p* / T_p**	SWAN Model	CD or [cfw]
IR06	0.65	7.20 cm / 7.34 cm	1.50 s / 1.53 s	Jacobsen et al. [2019]	1.73
				Suzuki et al. [2011]	1.42
				Collins [1972]	7.40
IR07	0.65	8.60 cm / 7.68 cm	1.70 s / 1.75 s	Jacobsen et al. [2019]	1.62
				Suzuki et al. [2011]	1.32
				Collins [1972]	6.00
IR08	0.65	10.00 cm / 8.44 cm	1.90 s / 1.98 s	Jacobsen et al. [2019]	1.55
				Suzuki et al. [2011]	1.32
				Collins [1972]	5.30
IR09	0.65	11.00 cm / 10.07 cm	2.1 s / 2.12 s	Jacobsen et al. [2019]	1.52
				Suzuki et al. [2011]	1.30
				Collins [1972]	4.70

Water Level 0.60 m

ID	h_v/d	$H_{m0}*$ / $H_{m0}**$	T_p* / T_p**	SWAN Model	CD or [cfw]
IR11	0.76	5.60 cm / 5.10 cm	1.30 s / 1.39 s	Jacobsen et al. [2019]	1.75
				Suzuki et al. [2011]	1.50
				Collins [1972]	15.0

IR12	0.76	6.90 cm / 6.18 cm	1.50 s / 1.53 s	Jacobsen et al. [2019]	1.60
				Suzuki et al. [2011]	1.35
				Collins [1972]	9.50
IR13	0.76	8.20 cm / 7.32 cm	1.70 s / 1.75 s	Jacobsen et al. [2019]	1.54
				Suzuki et al. [2011]	1.31
				Collins [1972]	7.40
IR14	0.76	9.50 cm / 8.44 cm	1.90 s / 1.98 s	Jacobsen et al. [2019]	1.52
				Suzuki et al. [2011]	1.34
				Collins [1972]	6.30
IR15	0.76	10.60 cm / 9.31 cm	2.10 s / 2.12 s	Jacobsen et al. [2019]	1.47
				Suzuki et al. [2011]	1.35
				Collins [1972]	5.40

Water Level 0.50 m

ID	h_v/d	$H_{m0}*$ / $H_{m0}**$	T_p* / T_p**	SWAN Model	CD or [cfw]
IR21	0.92	4.10 cm / 3.76 cm	1.10 s / 1.08 s	Jacobsen et al. [2019]	1.58
				Suzuki et al. [2011]	1.68
				Collins [1972]	220.
IR22	0.92	5.30 cm / 4.88 cm	1.30 s / 1.39 s	Jacobsen et al. [2019]	1.50
				Suzuki et al. [2011]	1.55
				Collins [1972]	45.0
IR23	0.92	6.50 cm / 5.97 cm	1.50 s / 1.53 s	Jacobsen et al. [2019]	1.44
				Suzuki et al. [2011]	1.48
				Collins [1972]	18.0
IR24	0.92	7.70 cm / 7.08 cm	1.70 s / 1.75 s	Jacobsen et al. [2019]	1.42
				Suzuki et al. [2011]	1.47
				Collins [1972]	11.5
IR25	0.92	8.80 cm / 8.11 cm	1.90 s / 1.98 s	Jacobsen et al. [2019]	1.38
				Suzuki et al. [2011]	1.44
				Collins [1972]	8.00
IR26	0.92	9.90 cm / 9.12 cm	2.10 s / 2.12 s	Jacobsen et al. [2019]	1.40
				Suzuki et al. [2011]	1.48
				Collins [1972]	6.50

Water Level 0.40 m

ID	h_v/d	$H_{m0}*$ / $H_{m0}**$	T_p* / T_p**	SWAN Model	CD or [cfw]
IR31	1.17	3.90 cm / 3.71 cm	1.10 s / 1.08 s	Jacobsen et al. [2019]	2.30
				Suzuki et al. [2011]	2.55

				Collins [1972]	> 10000.
IR32	1.17	5.00 cm / 4.76 cm	1.30 s / 1.39 s	Jacobsen et al. [2019]	1.78
				Suzuki et al. [2011]	1.90
				Collins [1972]	150.
IR33	1.17	6.00 cm / 5.75 cm	1.50 s / 1.53 s	Jacobsen et al. [2019]	1.60
				Suzuki et al. [2011]	1.75
				Collins [1972]	25.0
IR34	1.17	7.00 cm / 6.65 cm	1.70 s / 1.75 s	Jacobsen et al. [2019]	1.50
				Suzuki et al. [2011]	1.65
				Collins [1972]	11.5
IR35	1.17	8.00 cm / 7.63 cm	1.90 s / 1.98 s	Jacobsen et al. [2019]	1.40
				Suzuki et al. [2011]	1.55
				Collins [1972]	7.00
IR36	1.17	9.00 cm / 8.69 cm	2.10 s / 2.12 s	Jacobsen et al. [2019]	1.43
				Suzuki et al. [2011]	1.59
				Collins [1972]	5.80

The drag coefficient for explicit models has been related to the flow conditions with the Keulegan Carpenter number by several studies (e.g., Mendez and Losada, 2004, Sánchez-González et al., 2011, Jadhav et al., 2013). The relation to the KC depends on the maximum orbital velocity (z=0) from H_{rms} at the center of the canopies field [Mendez and Losada, 2004]. The WG11 is only 5.5 cm after the exact canopies length center and is used for the present study. The maximum velocity was obtained with T_p as more energy is present at that point, which results in the final form of the KC given as:

$$KC = \frac{\hat{u}_{rms,max} T_p}{b_v} = \frac{H_{rms,WG11} \frac{\cosh[k_p(d+0)]}{\sinh(k_p d)}}{2b_v} \qquad\qquad [-] \quad (4.1)$$

Previous studies have arrived to CD predictions with good correlations to their experimental data. Mendez and Losada [2004] tested $CD(KC) = 0.47 * \exp(-0.052 K)$ and later suggested a relation of the CD to a modified version of KC (Q) that includes the vegetation height (h_v), finding a correlation of 92 % to Løvås and Tørum [2000] data set. The relation is included in Figure 4.4 and given by:

$$CD(Q) = \frac{\exp(-0.0138Q)}{Q^{0.3}} \qquad\qquad 7 \le Q \le 172 \quad (4.2)$$

with

$$Q = \frac{KC}{h_v/d^{0.76}} \qquad\qquad [-] \quad (4.3)$$

Other formulations to predict the drag coefficients have been explored in the present research. The relations of Sánchez-González et al. [2011] and Jadhav et al. [2013] valid region ($15 \le KC \le 425$, and $25 \le KC \le 135$ respectively) are outside of the values in the present study ($0 \le KC \le 3$). Exploring their performance under the present conditions resulted in substantial deviations (up to factors 40 and 20, respectively). The valid range of Mendez and Losada [2004] formulation is neither fulfilled. Still, this model provided results in the same order of magnitude than the present coefficients. It was found that a correction factor of 2.0 increases its correlation to the present data, as displayed in Figure 4.4. The differences between explicit models'

coefficients are analyzed through the CD ratio of Suzuki et al. [2011] coefficient over the new model. These observations showed that a threshold could be present (between $2 \leq Q \leq 3$), having larger Suzuki et al. [2011] coefficients below this threshold, and smaller above it. The CD ratio ranged between 0.80 to 1.15 in the tested conditions. The differences between explicit models' drag coefficients are larger for increasing values of $k_p d$ and submergence, which is consistent with the bulk differences discussed in Chapter 2 and 3. Performing further investigations around the relation between explicit models' coefficients could lead to expressions between the CD obtained after several experimental and field campaigns, and the required $\alpha^3 CD$ values for the new formulation.
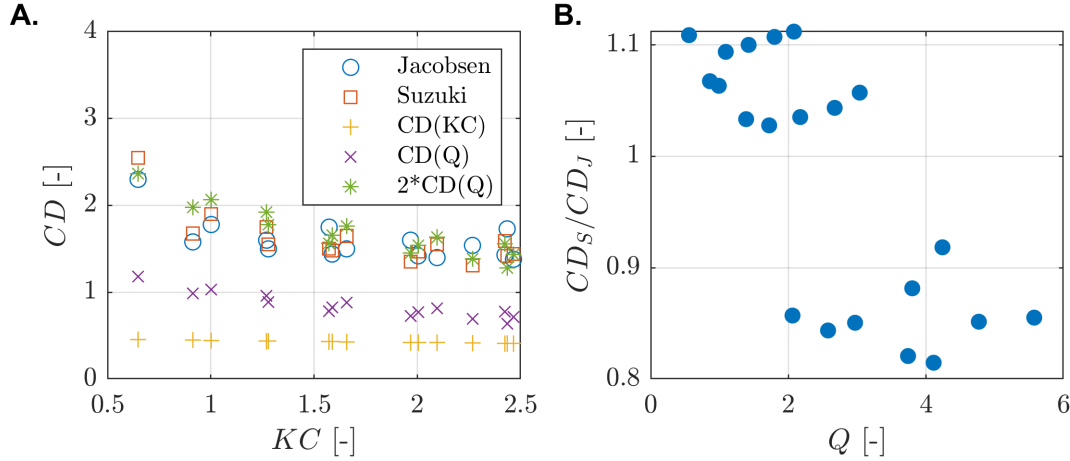
Figure 4.4: Drag coefficients for tested explicit models (Suzuki et al. [2011] and new implementation) with **A.** the Keulegan Carpenter number KC, and **B.** wave-depth regime represented by $k_p d$.

Implicit modeling represented by Collins [1972] model could reproduce the total dissipation except for case IR31. For this experiment, [cfw] was increased up to a value of 10,000. No improvements in the decay curve were observed after values [cfw] = 500. Even though Collins [1972] could simulate the total dissipation for most cases, the decay curve of the bottom friction model followed a curvature with a larger radius than measurements for all cases, as displayed in Figure 4.5. The deviations of this decay curve were considerably smaller for the smallest wave periods under h_v/d = 0.65, as displayed in Figure 4.6. Between explicit models, the new implementation's decay curve showed a slightly stronger curvature than Suzuki et al. [2011], placing Suzuki et al. [2011] closer to the cases in which measurements had milder curvatures than both explicit models. These differences are small, concluding that both of the explicit models presented a good match for the measurement decay curves.

Spectral characteristics like the mean period can represent the distribution of energy. In the present analysis, T_{m01} and T_{m-10} are included due to their extensive use in the engineering and scientific community. The spectral changes, driven by the dissipation present in the canopies field, are compared between measurements and models through the mean period evolution (T_{m01} in full lines and T_{m-10} in dashed lines), as displayed in Figures 4.5 and 4.6.

Both frequency-dependent and equally distributed explicit models capture the spectra's qualitative evolution for $h_v/d \geq 1.0$. This is consistent with the observations in Chapter 3 in which emergent vegetation gives rise to the smallest differences between models. The implicit model evolved for smaller values of the mean period, while the measurements mean period increased for these conditions as predicted by the explicit models. The implicit model from Collins [1972] did not capture the total energy decay and the energy distribution for emergent vegetation.

If canopies are submerged, the conserved energy in high frequencies shifts the spectral evolution to lower characteristic frequencies (higher values of T_m). Under these conditions, the model from Collins [1972] captures the right sign of the period evolution but not the magnitude. The explicit model from Suzuki et al. [2011] assigns more dissipation to the high frequencies that are not significantly affected in the measurements, causing an opposite result in the prediction of the mean period. The new model showed the capability to assign the right weight of dissipation depending on the level submergence, leading to the right prediction of mean periods for emergent and submerged vegetation.
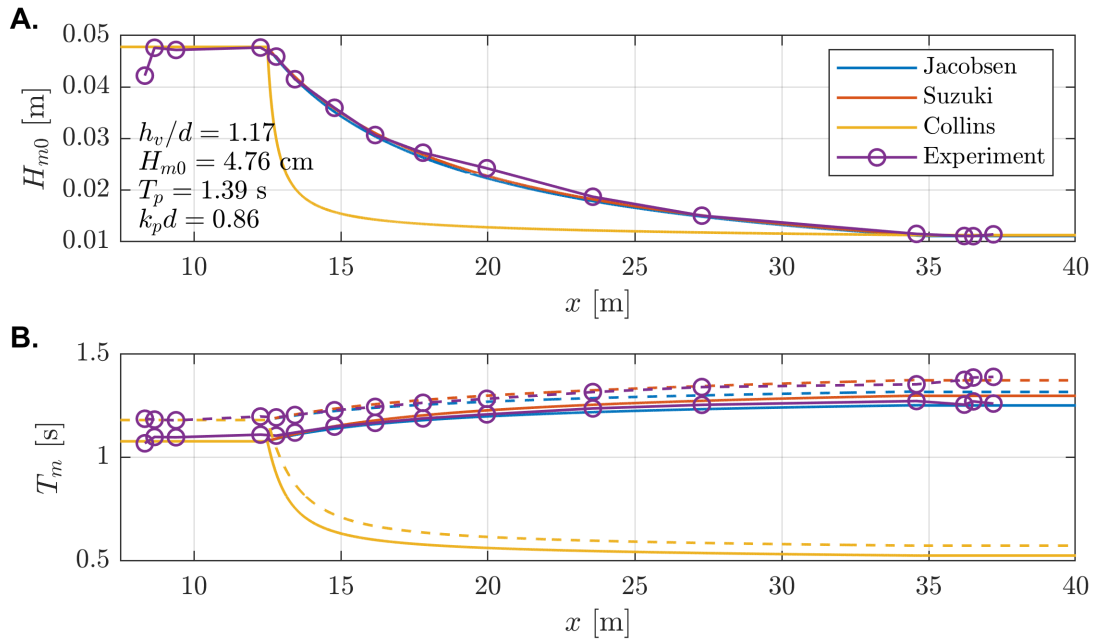
Figure 4.5: Calibrated **A.** significant wave height, and **B.** mean period evolution (T_{m01} full line, T_{m-10} dashed line) through the spatial domain including experimental data and model comparison for IR32 with boundary conditions $T_p = 1.27$ s, $H = 4.76$ cm, and $h_v/d = 1.17$.
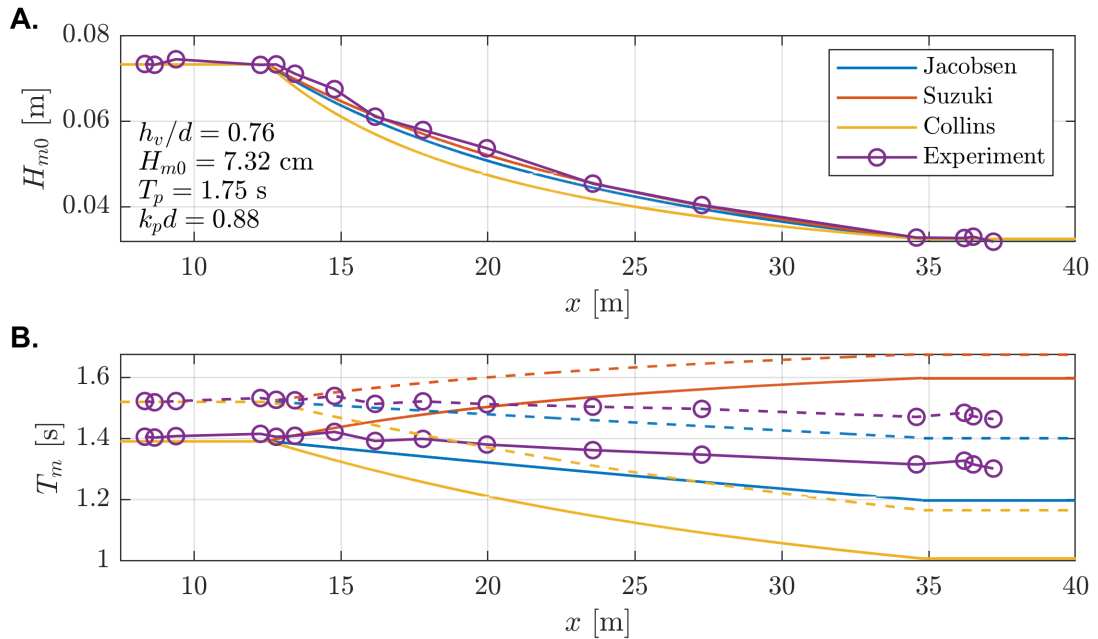

Figure 4.6: Calibrated **A.** significant wave height, and **B.** mean period evolution (T_{m01} full line, T_{m-10} dashed line) through the spatial domain including experimental data and model comparison for IR13 with boundary conditions $T_p = 1.75$ s, $H = 7.32$ cm, and $h_v/d = 0.76$.

The modeling performance and spectral mismatch are analyzed by comparing the distribution of energy on different stations (WG), as displayed in Figures 4.7, and 4.8. The measured spectra by gauges after canopies (WG14-16) show differences around the peak frequency. This is related to the small amount of energy present at those locations, which becomes more sensitive to data collection and processing. These three stations' results have been average and included in the visual comparison to the model results.
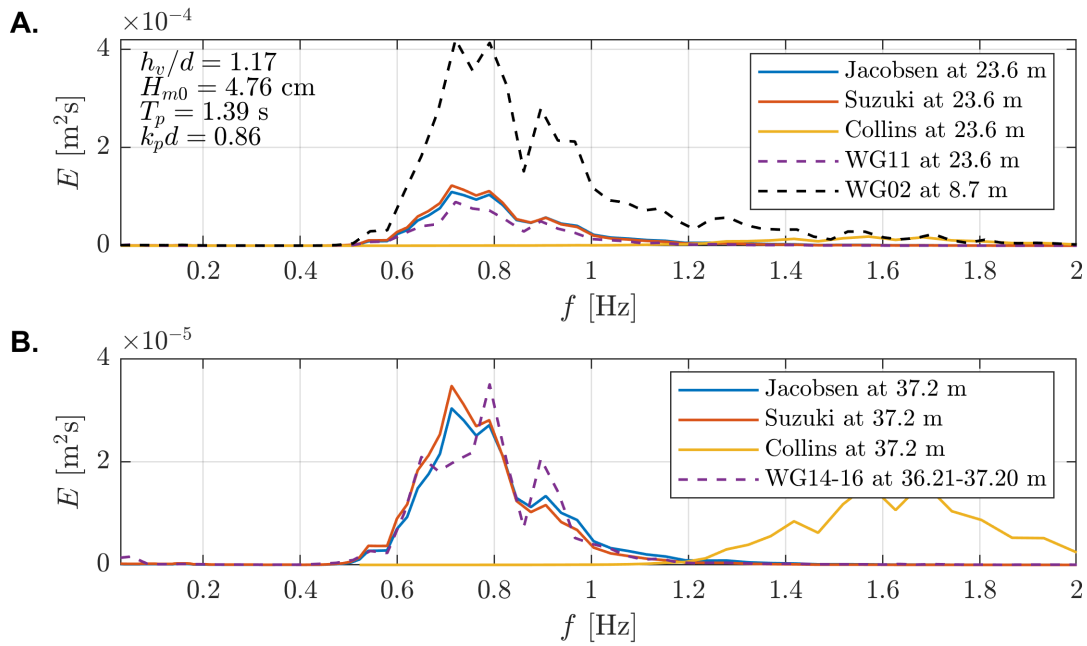
Figure 4.7: Variance density spectrum for the measurements and models for IR32 with boundary conditions T_p = 1.39 s, H_{m0} = 4.76 cm, and h_v/d = 1.17. **A.** Boundary condition (WG02) compared to WG11 at 23.57 m. **B.** Comparison of mean spectra of measurements after canopies (WG14-16) and experiments.
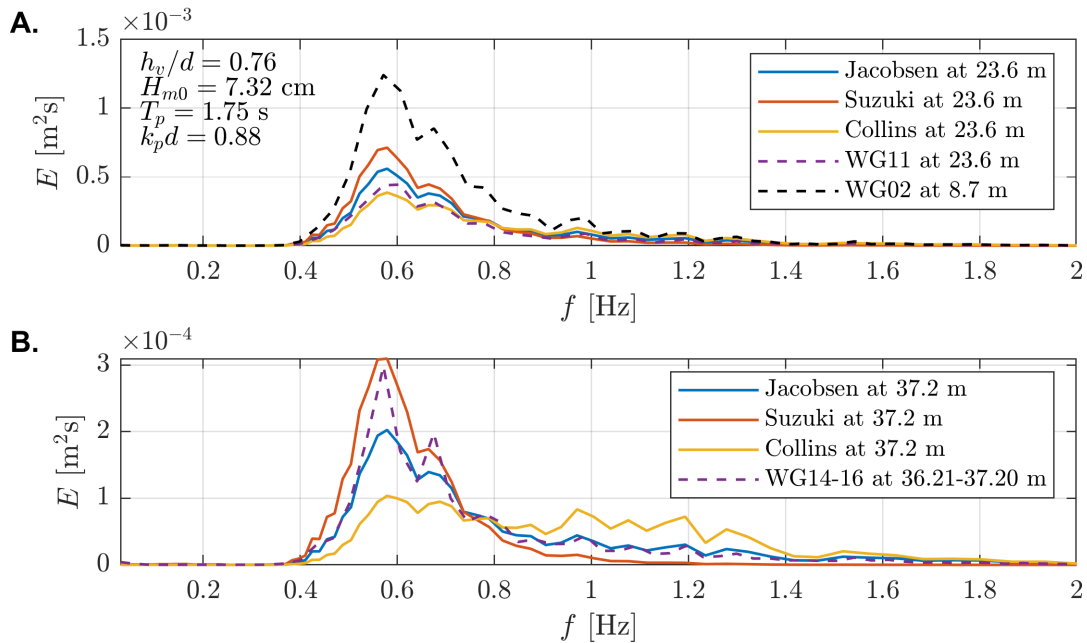
Figure 4.8: Variance density spectrum for the measurements and models for IR13 with boundary conditions T_p = 1.75 s, H_{m0} = 7.32 cm, and h_v/d = 0.76. **A.** Boundary condition (WG02) compared to WG11 at 23.57 m. **B.** Comparison of mean spectra of measurements after canopies (WG14-16) and experiments.

The presence of energy below frequencies 0.4 Hz was almost non-existent in the measurements. According to an author of this experimental campaign, no energy has been filtered out. As random waves were generated to target a specific spectrum, low frequencies should have occurred in the wave flume. The lack of random waves outside a specific range might be related to the conditions in which the waves were generated, aiming for linear conditions under certain spectral range by repeating the signal. It is recommended to

investigate further the lack of energy at low frequencies in the present data set.

As discussed previously, the differences between explicit models become smaller for $h_v/d \geq 1.0$ but are still present. More energy is present at the peak for Suzuki et al. [2011], while the opposite is found in the high-frequency tail. The spectral mismatch for implicit modeling and vegetation present in all the water column is vast, all the energy around the peak is dissipated after the canopies shifting the spectral to higher frequencies. The spectral comparison tells that the implicit model is not capable of spectral modeling the dissipation by vegetation with $h_v/d \geq 0.65$. The spectra's energy is underpredicted by strong bottom-friction coefficients that favor the dissipation from long to short components, vanishing all energy in those frequencies. The spectral distribution at the end shows a widely distributed shape, which does not represent the measurements. The model from Suzuki et al. [2011] performed better than implicit modeling but with significant qualitative mismatch by dissipating almost all energy in high frequencies, as shown in Figure 4.8. The new model shows a good fit for all submergences, accurately predicting the energy before and after the peak frequency.

The spectra are modified by the dissipation shape, which is analyzed by looking at the changes in the energy distribution. The average variance spectrum of the last wave gauges (WG14-16) is subtracted from the boundary conditions (WG02), as shared in Figure 4.9. This is different from the previous Chapter, which focused on comparing the shape on the first grid. It was decided not to subtract the first two stations because of two reasons. First, large variability is present between neighboring gauges adding weight to local processes and instrument errors. Secondly, the calibration was performed targeting the end of the canopies, and if the spectral distribution aims to be clearly observed, the spectrums should have the same amount of energy.
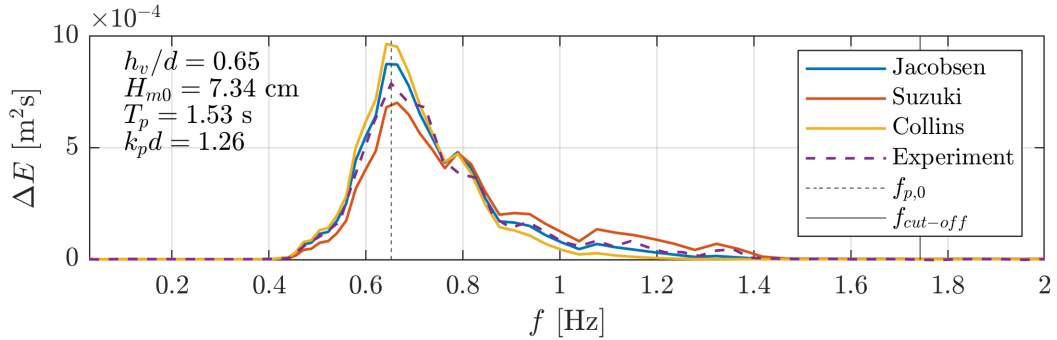

Figure 4.9: Distribution of the energy decay between WG14-16 (36.21-37.2 m) and WG02 (8.7 m) for the experimental data and models with boundary conditions T_p = 1.53 s, H_{m0} = 7.34 cm, and h_v/d = 0.65.

As observed in Figure 4.9, the model from Suzuki et al. [2011] dissipates the energy in high frequencies more strongly than the measurements. If the same total energy is compared between measurements and this model, the energy present in the rest of the frequencies will be under dissipated. This pattern was observed for all cases but more substantial for larger values of $k_p d$. The definition of the velocity spectrum by mean properties in Suzuki et al. [2011] causes orbital velocities and their dissipation to be over and underpredicted for high and low frequencies, respectively. Defining the dissipation by a different characteristic frequency would assign more weight to the dissipation of specific frequencies. Nevertheless, measurements have shown that the weight of dissipation to specific frequencies depend on the regime of each component (kd). Different levels of submergences require a model that can shift the weight of dissipation depending on the interaction between the velocity profile and canopies. The new model showed to be capable of capturing the physics behind this process by providing accurate results for all tested cases.

Implicit modeling showed an increasing mismatch for shallower depths and longer periods. The model dissipated too much energy on the low and mid-range frequencies while keeping too much on high frequencies. Implicit modeling was developed to reproduce the dissipation by bottom friction. Later, this model has been used to model the dissipation by highly submerged vegetation like seagrasses. Under those cases, seagrasses might be present in only a small fraction of the water column, leading to the findings of better spectral performances when compared to other models [Nowacki et al., 2017]. Nevertheless, the tested values of the present campaign ($h_v/d \geq 0.65$) showed that the implicit model of Collins [1972] was not able to reproduce the distribution of energy.

The dissipation frequency cut-off defined with linear wave theory in Jacobsen et al. [2019] (equation 2.16) was compared to the measurements. As observed in the example of Figure 4.9, the theoretical cut-off (1.74

Hz) for h_v/d = 0.65 is well beyond visible changes in the energy distribution. The dissipation frequency cut-off for $h_v/d \geq 0.76$ was located in frequencies higher than the models spectral upper limit of 2.00 Hz, and therefore, their dissipation.

All models' performances have been analyzed and summarized by their fit to the measurements mean period in the same spectral range. The subtraction of the mean period after and before the canopies (ΔT_m) captures the sign and accuracy of the prediction. The results of this comparison based on T_{m01} and T_{m-10} are shared in Figures 4.10 and Figure 4.11, respectively.
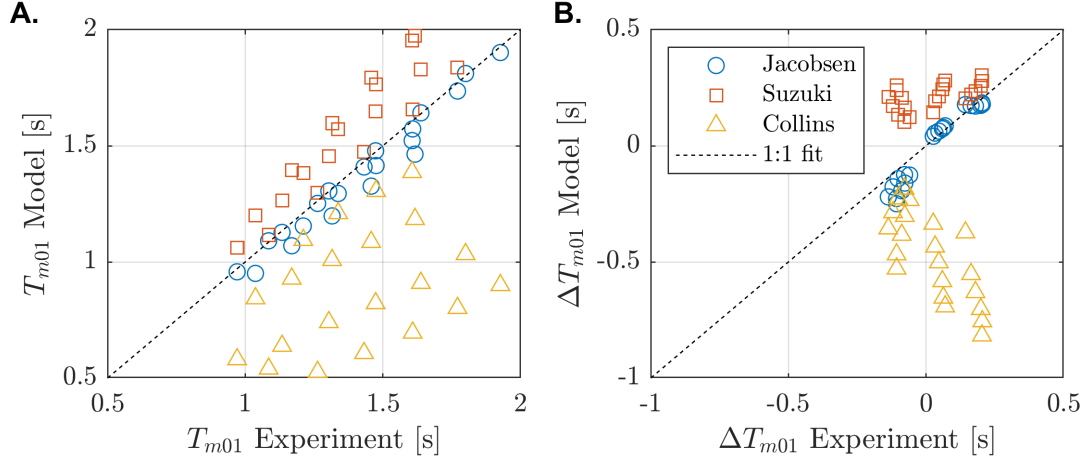
Figure 4.10: **A.** Mean period T_{m01} at the end of the canopies (WG14-16) by the model and measurements. **B.** Subtraction between mean period T_{m01} at the end of the canopies (WG14-16) and boundary condition (WG02) for the model outputs and measurements.
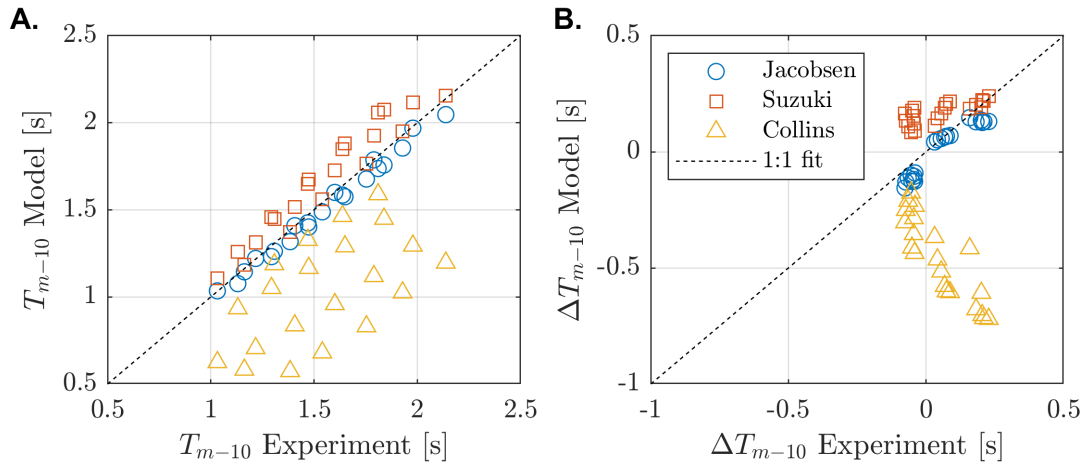
Figure 4.11: **A.** Mean period T_{m-10} at the end of the canopies (WG14-16) by the model and measurements. **B.** Subtraction between mean period T_{m-10} at the end of the canopies (WG14-16) and boundary condition (WG02) for the model outputs and measurements.

The mean periods at the end of the domain were smaller than the boundary condition for all cases with the implicit model of Collins [1972], while all the results from the explicit model of Suzuki et al. [2011] showed larger values. The measured spectra, characterized by the mean periods, evolved to higher or lower frequencies depending on the submergence and wave conditions. The new implementation based on Jacobsen et al. [2019] showed the capability to shift together with the measurements. The new model captures the correct sign of ΔT_m and an accurate prediction on the magnitude of T_m at the end of the canopies. This is contrary to the results from Collins [1972] and Suzuki et al. [2011], which validity to reproduce the period evolution properly is restricted to certain conditions, showing improvements for canopies modeling.

4.3. Discussion

The experimental campaign measurements were developed for a different purpose than the present research. This created a difference between target and measured conditions. An analysis in Appendix C shows that defining a JONSWAP or providing the measurements as boundary conditions is not crucial for conclusions, as differences are not significant. During the field validation, a large mismatch is present at this range of frequencies. Therefore, it is recommended in future investigations with flume experiments to generate and measure energy in low-frequencies for validation purposes.

The C_D predictive formula of Mendez and Losada [2004] based on a modified version of the KC (Q) showed a good correlation if factor 2.0 was added. This provides a possible starting point for future calibrations with similar conditions. The drag coefficients from Suzuki et al. [2011] were higher than the new model for $Q < 2.0$, and the opposite for $Q > 4.0$. Performing research between the obtained drag coefficients in previous studies (e.g., Cavallaro et al., 2010, Jadhav et al., 2013, Ozeren et al., 2014) considering its dependency on the canopy properties, submergence, wave conditions, and extension of the vegetated field could draw a connection between dissipation models. If a conversion relation is obtained, the use of these values could provide the new model with a wide range of C_D for future applications.

The implicit model from Madsen et al. [1988] could not be calibrated to reproduce the amount of dissipation for the present conditions. The model is iteratively solved in SWAN with Jonsson [1966], for which a friction factor of 0.3 is set if $A_b/k_N < 1.57$. If the limitation is removed from the Madsen et al. [1988] implementation in SWAN, the model could be compared to measurements with higher dissipation rates. The model from Collins [1972] represented the implicit approach for the remaining experimental validation. The large variability of the friction coefficients was observed for the present experiments (e.g., 6.50 to 220.00 for $h_v/d = 0.92$), which are conditions beyond the range the formulation was designed for (bottom friction). The friction coefficient from Collins [1972] lacks a physical relation to the canopies properties, making it prone to tuning errors. Also, under high relative submergences ($h_v/d \leq 0.65$), the spectral performance of Collins [1972] was very poor, dissipating most of the energy around the peak frequency and conserving a large amount of energy at high frequencies.

Different levels of submergences require a model that can shift the weight of dissipation to different ranges of frequencies, depending on the interaction between the velocity profile of each component and canopies. The present validation and performance comparison analysis are qualitatively summarized in Table 4.3.

In addition to vegetation, rigid canopies have also used to represent the dissipation of other natural barriers like coral reefs. The underwater ecosystems are represented implicitly due to the frequency-dependent dissipation, as discussed in Lowe et al. [2007]. Exploring the applicability of the present model to those ecosystems could provide the possibility to be the first implemented model in SWAN to include this type of modeling explicitly.

Furthermore, the studied experimental campaign uses rigid elements, while flexibility is inherent in vegetation. Flexibility would likely modify the spectral and bulk dissipation of the tested dissipation models. In the validation from Jacobsen et al. [2019] with flexible stems, a slight overprediction of dissipation in low frequencies was observed. This factor could be isolated by investigating the effect of flexibility on the spectral evolution of wave flume measurements. This is discussed with the field measurements in the upcoming Chapter.

Approach	Model	h_v/d	Performance over Canopies	
			Bulk	Spectral
Implicit	Madsen et al. [1988]	0.65	- -	- -
		0.76	- -	- -
		0.92	- -	- -
		1.17	- -	- -
Implicit	Collins [1972]	0.65	+ +	+
		0.76	+	-
		0.92	- -	- -
		1.17	- -	- -
Explicit	Suzuki et al. [2011]	0.65	+ +	-
		0.76	+ +	-
		0.92	+ +	-
		1.17	+ +	+ +
Explicit	Jacobsen et al. [2019]	0.65	+ +	+ +
		0.76	+ +	+ +
		0.92	+ +	+ +
		1.17	+ +	+ +

Table 4.3: Modeling performance of implicit and explicit models for wave dissipation over the present experimental campaign of rigid canopies with different submergences over a flat bottom.
Good qualitative and quantitative fit: ++ , Qualitative fit with some deviations: + , Bad fit: - , Wrong representation: - - .

5

Validation with field measurements

This Chapter describes the site and conditions on which field measurements were performed. The field campaign is part of the *"POV Waddenzeedijken HR Effectiviteit Voorlanden"* (*POV*), which performed previous SWAN computations and analysis, and the *BE-SAFE* project (Bio-Engineering for safety using vegetated foreshores) projects. Both programs investigate the effectivity of vegetated foreshores in providing coastal protection, especially in front of existing barriers as dikes. Collaborators on these projects include companies and research institutes like Deltares, HKV, TU Delft, Arcadis, and NIOZ. At the study location in the province of Groningen, instruments were deployed during the period of the year when storm occurrence is the largest: winter. Successfully, two large storms were recorded by pressure sensors in January of 2015 and 2017. This local wave information was validated against nested SWAN modeling, which was fed by hindcast information of wind, water levels, and currents at different moments during the storm. The model output at the end of the canopies showed not yet understood differences against measurements, as described in the problem statement and Figure 1.3, which is hereafter investigated. The new implementation, together with other explicit and implicit models, are used to explore the SWAN performance under this situation. Insights from previous chapters are used to contribute towards the understanding between model differences, possible improvements, and further recommendations to reduce the spectral mismatch.

5.1. Field Measurements and Data

The site of study is located on the continental dutch coastline of the Wadden Sea between Noordpolderzijl and Eemshaven in the province of Groningen, in the north of the Netherlands. The Wadden Sea is the largest unbroken tidal flat system in the world and a UNESCO World Heritage site. Separated by a system of islands and islets from the North Sea, the waves are a combination of locally generated waves at the Wadden Sea and waves penetrating from the North Sea between the islands.

The Wadden Sea is a dynamic system where tides, waves, and biological factors shape the morphology and habitats like tidal channels, shoals, seagrass meadows, mussel beds, mudflats, and salt marshes. Vegetated foreshores are often present in front of the protecting dikes. Understanding the effects of vegetation in the wave transformation is key to determine the forcing that these dikes experience. Therefore, the *POV* and *BE-SAFE* projects have collected data in vegetated foreshores to study its effect on flooding safety and structures design. It has been confirmed that vegetation reduces the load forces on the dikes, reducing design and maintenance requirements [Vuik et al., 2019], and failure mechanisms like wave run-up Post [2015].

The boundary conditions for the flooding assessments and design criteria are provided by the SWAN model, which allows predicting the conditions that the dikes and foreshores will experience. During the validation of the model for these locations, spectral differences between model and measurements have not been understood. Explicit and implicit models have been tested without further reduction in the spectral mismatch. Accurately predicting the frequency distribution of energy is crucial to determine critical processes on the protection structures against the forces of the sea (e.g., the run-up is largely affected by low frequencies, which are presently mismatched by the model output). Measurements have provided validation material for improvements of the wave model. A field campaign successfully obtained wave pressure information for two winter storms in January of 2015 and 2017. During these events, the water level experienced
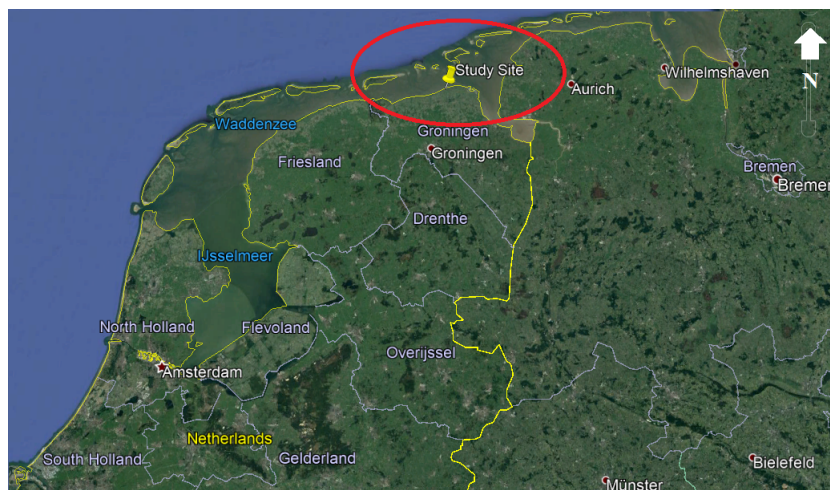
Figure 5.1: Study site at the Wadden Sea coastline close to Eemshaven, Groningen in the north of The Netherlands.
(Based on Google Earth Imagery).

an increase of more than 3 m for the water level of both events, due to a significant storm surge during high tide. This allowed storm waves to reach the dike over 1-2 meters of water over the marshes.

The storm of January 2015 was measured with eight wave gauges, which were mounted between 9 and 17 cm from the bottom and deployed, as shown in Figure 5.3. The stations' distribution consisted of a transect normal to the dike, and additional measurements along the coastline. From the additional locations, one sensor (p6) was placed in front of the dike western from the transect, where vegetation is mature, other (p7) to the east where pioneer marsh is present, and the last one (p8) was installed on a bare mudflat. The normal transect consists of five stations using the marsh edge as the origin. The first station (p1) is located 2.5 m before the start of the salt marsh, the next stations are at 5, 15, and 50 m inside of the vegetated field (p2, p3, p4), and finally (p5) near the dike which is around 300 m from the marsh edge. Poles 1-4 collected the wave transformation over the pioneer zone, as shown in Figure 5.2, and poles 4-5, the mature marsh zone. The pioneering zone from salt marshes consists of certain species adopting a new area and, consequently, scarcer vegetation. Images accessed by satellite images do not show significant changes in the marsh edge position and vegetation density in the pioneer zone between 2015 and 2017.

Figure 5.2: Wave gauges owned by NIOZ at the transect of study, after the storm of January 2015. On the picture is observed p1 located 2.5 m before the marsh edge, while p2 and p3 on top of the pioneer zone. Denser vegetation in the mature zone is observed closer to the dike. (Data obtained from Vincent Vuik)

The storm of January 2017 was measured with seven wave gauges, which were also mounted around 10 cm from the bottom and deployed in a slightly different arrangement than the previous campaign. The

position of these stations is shown in Figure 5.3. The same transect than previously studied is included in the measurements but with one instrument less. In this case, the wave gauges were installed at 2.5 m before the marsh edge (p1, same than p1 in 2015), 50 m from the edge inside the vegetation (p2, same location than p4 in 2015), 100 m (p3), and near the dike (p4, same location than p5 in 2015). Poles 5-7 were installed on the mudflat east from the site to isolate the effect of vegetation in wave dissipation over foreshores for other studies (e.g., [Vuik et al., 2016], [Vuik et al., 2018b]).

Figure 5.3: Position of the eight deployed pressure sensors at the study site during the storm of January 2015. (Modified from data provided by Vincent Vuik)

Figure 5.4: Position of the seven deployed pressure sensors at the study site during the storm of January 2017. (Modified from data provided by Vincent Vuik)

The wave pressure was recorded by wave gauges (Ocean Sensor Systems, Inc., USA) with a frequency of 5 Hz over a period of 7 min, every 15 min for the storm of 2015 and continuously in 2017 [Zhu et al., 2020b]. The collected wave pressure data can be processed to obtain the surface water elevation in time series following linear wave theory. During the storm, the water levels and wave conditions change over time. The time burst (15 min) with the highest amount of wave energy, characterized by $H_{m,0}$, is defined as the peak of the storm. It occurred at 01:00 on the 11th of January 2015, and at 22:00 h on the 13th of January 2017, as selected in Steetzel et al. [2018]. These two moments and the wave transformation over the transect are the centers of the present validation and comparison. A burst of the time series near the peak of the storm in January 2017 is shared in Figure 5.5.
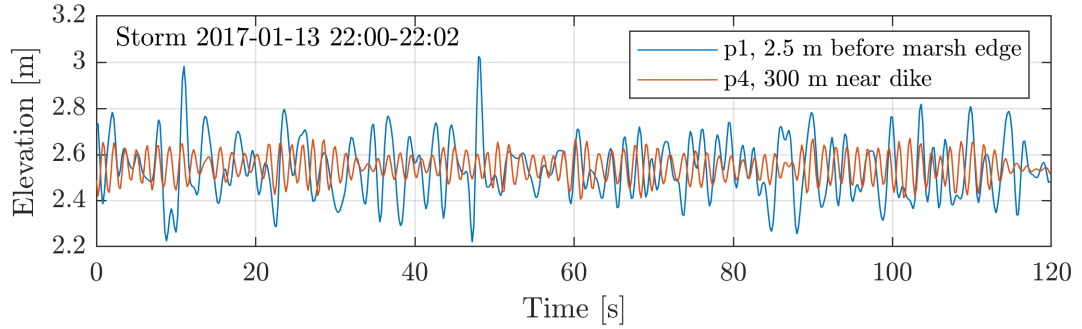
Figure 5.5: Water surface elevation between 22:00 and 22:02 h, around the peak moment of the storm in January, 2017 for the first (p1) and last station (p4) of the study transect.

Before the marsh edge, the incoming conditions show asymmetric and skew steep waves, pitched-forward and with higher crests than troughs. This is caused due to shallow water conditions, as the foreshore reduces the wave depth, which might end up in-depth wave breaking. It was documented in Vuik et al. [2018b] that the relative contribution of vegetation to energy dissipation depends on the water depth. Therefore, even though other mechanisms could contribute to a large part of the total dissipation in the first meters, the vegetation will increase its contribution as it becomes denser and water shallower. Near the dike, the water surface elevation of Figure 5.5 shows wave groups caused by the interaction of two wave trains with slightly different frequencies and similar amplitudes. This will result in a bounded wave, with the trough where amplitudes are higher due to a larger transport of momentum. The classification and possible cause of these long waves is discussed in section 5.5.

The variance density spectrum is obtained from these 15 min time series with a Fourier Transform, as briefly described in Section 2.1. The spectra were delimited between 0.01 and 1.00 Hz during the spectral processing, as almost no energy was observed after 0.8 Hz. The evolution of bulk energy is represented by the significant wave height ($H_{m,0} = 4\sqrt{m_0}$) and visualized with the bathymetry and water levels during the storm peak at each station, as shared in Figure 5.6. Before and after the storm, bed elevations values varied up to 3 cm at the instrument stations. The post-storm bathymetry is used in the present analysis. The bed elevation near the dike had a lower elevation (16 cm less) in 2017 than in 2015. The depth of the water column caused by the storm surge and high tide at the peak of both storms are very similar but slightly higher for 2017. The wave height evolution shows a more energetic event in 2017 than 2015 but with similar results near the dike. Vegetation and other dissipation mechanisms (e.g., depth breaking) damped the energy in the foreshore and converged in similar energy levels near the dike for equivalent submergences.
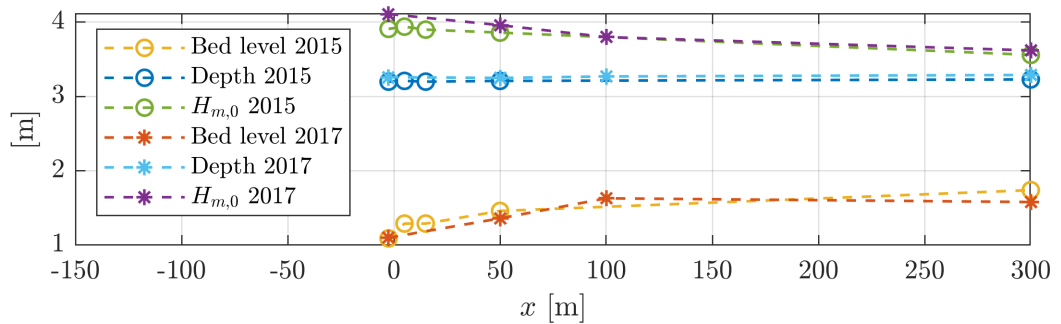

Figure 5.6: Water depth and significant wave height at the peak of the storm of January 2015 and 2017 compared to the bed elevation post-event. The bathymetry reported +NAP, water depth above the bed level, and the significant wave height visualized on top of the water surface. (Data from Steetzel et al. [2018] and Zhu et al. [2020b]).

Figures 5.7 and 5.8 show the distribution of energy between stations for the storm of January 2015 and 2017, respectively. A large amount of energy is present around 0.03 Hz, a recommended lower limit for SWAN wave modeling. According to the The SWAN team [2019a], this limit is suggested as no energy should be present in the first spectral bin. A considerable amount of energy at low frequencies exists in all measure-

ments according to the author of the field campaign, opening the hypotheses that physical processes at the site could these still unexplained very long waves. The energy bellow 0.03 Hz might be originated during the wave spectrum analysis. Therefore, the energy bellow this frequency is not included in the characteristics analysis (e.g., $H_{m,0}$, T_m) but it is in the discussion. For a clear visual comparison, the input spectra's 400 spectral points are frequency average over five spectral bins (5-point moving average). A discussion over the visual comparison before and after frequency averaging the spectra is shared in Appendix E.
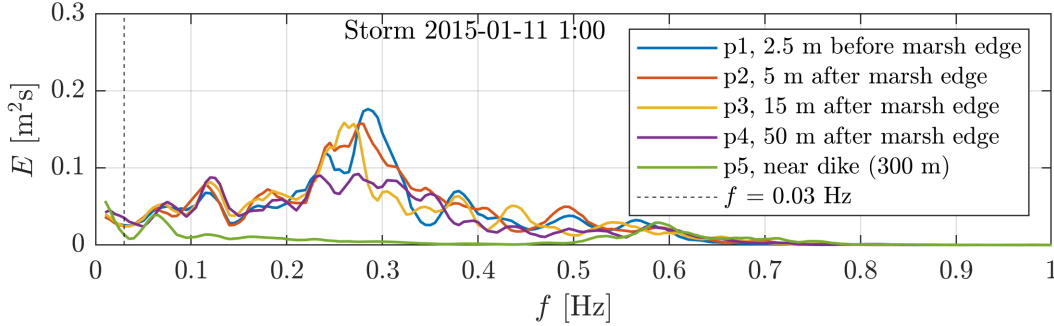
Figure 5.7: Spectral evolution along the measurements transects p1-p5 during the storm of the 11th of January 2015 at 01:00 h.
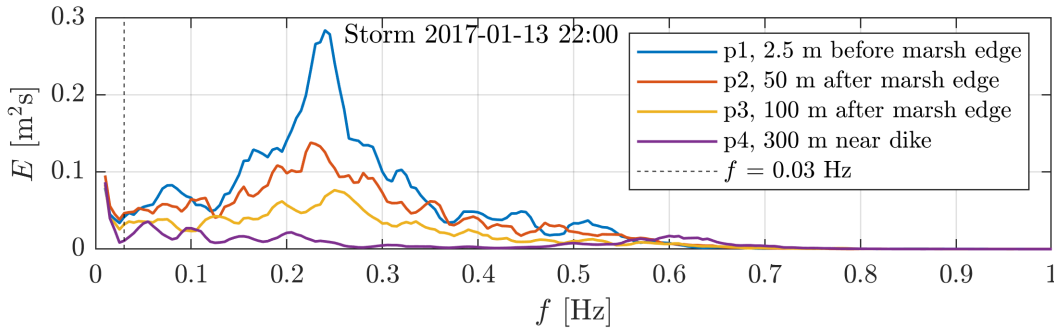
Figure 5.8: Spectral evolution along the measurements transects p1-p4 during the storm of the 13th of January 2017 at 22:00 h.

The spectral evolution from 2015 in Figure 5.7, and bulk energy decay in Figure 5.6, shows that almost no energy was dissipated between p1 and p3 ($H_{m,0}$ = 0.72, 0.73, and 0.70 m for p1, p2, and p3 respectively). Nevertheless, the distribution of energy does change. The energy around the peak shifts to lower frequencies and losses energy, while a slight increase in low and high frequencies is observed. Non-linear processes and wave-wave interactions like triads and quadruplets could be responsible for energy redistribution. The wind provides energy input at mid-range and high frequencies also, generating new waves over the transect. At p4, the spectra are already more widely distributed if compared to the shape at p1. The vegetation in the pioneer zone (p1-p4) dissipates the energy at the wind sea region (0.2-0.5 Hz) while keeping the energy at low frequencies almost unmodified. Almost all energy at the wind sea region has vanished after the mature marshes and near the dike, leaving behind a peak at low and high frequencies. The possible reasons behind the distribution of energy on this last station are discussed in the upcoming sections.

The peak of the incoming spectra at the marsh edge in 2017 contains significantly more energy than in 2015. In addition, the distance between stations provides a more clear overview of dissipation. The transect experiences stronger dissipation than the measurements of 2015, as similar energy near the dike is obtained. The station p2 is equivalent to the boundary between the pioneer and mature zone defined for the 2015 storm. Therefore, station p3 provides us a new insight into the evolution of the spectrum within the mature marsh zone. Near the dike, it is possible to observe the same overall behavior than discussed for the event of 2015. Most energy on the mid-range frequencies is dissipated. The energy on very high frequencies is increased, highlighting the effect of the wind or non-linear interactions in providing new energy to these frequencies. Energy is still retained in the low frequencies without a clear answer at the moment but investigated in the present Chapter. Important to note is the challenges to measure high frequencies with a deeply

submerged pressure sensor. The small pressure fluctuations are converted to wave amplitudes using an approximation factor from wave linear wave theory. The spectral evolution, measurements, and processing of the data are analyzed and commented throughout the present investigation.

The vegetation properties were measured via the dry biomass (*DBM*) method. The process involves putting into an oven the sampled and cut vegetation (shown in Figure 5.9), weighing it before and after the oven provides the wet and dry mass. The dry biomass results were close to 85% of the 'wet' natural biomass. Based on characteristic stem diameter, height, and ρ of the specie at the site, the density can be obtained following the relation:

$$N_v = \frac{DBM}{\rho \frac{\pi}{4} h_v b_v^2} \tag{5.1}$$

Figure 5.9: Picture of sampled Elymus vegetation for properties determination in January 2015. (Data obtained from Vincent Vuik)

In the present analysis, the marsh specie Elymus athericus & repens is assumed as dominant compared to the presence of other species. Because spatial and temporal variation exists in properties, and only one sample was obtained in this site, the detailed measurements of another project were received for reference and analysis. Along the coast of Friesland, a campaign measured the mean and standard deviation of vegetation properties over four months (March, June, August, and November), as displayed in Table 5.1. The months of March and November are more relevant for the present analysis and compared to the present project.

Location	Friesland				Groningen
Month	June	August	November	March	January
Stem length [cm]	47 ± 21 (180)	77 ± 13 (180)	77 ± 13 (180)	50 ± 14 (120)	50 ± 0 (1)
Stem diameter [mm]	1.6 ± 0.2 (20)	1.5 ± 0.3 (20)	2.1 ± 0.4 (15)	1.3 ± 0.2 (19)	1.3 ± 0 (1)
Stem density [stems/m^2]	533 ± 90 (36)	701 ± 207 (36)	637 ± 220 (36)	405 ± 339 (24)	1000 ± 0 (1)
Flexural stiffness [N mm^2]	1.4 ± 0.7 (20)	1.5 ± 0.8 (20)	1.1 ± 0.6 (15)	4.5 ± 1.1 (19)	-

Table 5.1: Vegetation measured properties along the north coast of Friesland with mean value $\pm$ standard deviation and number of samples between parenthesis for Elymus athericus & repens, compared to the vegetation properties of Elymus athericus & repens in the present field campaign for 2015. (Data obtained from Vincent Vuik)

The observed values at the site were similar to the mean reported values of March. The vegetation height at this month is shorter and thinner than the vegetation in November. During winter, stem flexibility reduces due to seasonal changes, increasing the possibility of stem breakage (which largely change biomass). At the end of winter and beginning of spring, the new young and thin stems start to grow. The characteristic density

of the salt marsh species Elymus is 732 g/m^2, which with the observed vegetation height (~ 0.5 m) and diameter (~ 1.3 mm) resulted in a vegetation density of ~ 1000 stem per m^2. This density is considerably larger than in Friesland, which high variability is a factor to consider for wave modeling over vegetation. The vegetation density could change the dissipation model results by a factor 1.8 if the deviation from March is observed.

The same properties observed in 2015 are used to describe vegetation in 2017. Nevertheless, more intensive grazing by sheep was observed in 2017, as observed in Figures 5.10 and 5.11. Besides, it is possible to observe significant spatial variations on the vegetation properties and morphology (flats and channels). These temporal and spatial variations are considered for the following discussion.

Figure 5.10: Picture of the site of study in January 2015. Taken at the end of the dike slope facing seawards. Note the metal door and bridge for reference. (Data obtained from Vincent Vuik)

Figure 5.11: Picture of the site of study in January 2017. Taken on top of the dike slope facing seawards. Note the metal door and bridge for reference. (Data obtained from Vincent Vuik)

The effect of breakage was studied by Vuik et al. [2018b] as it reduces stem height and density. Breakage is highly possible during winter when the stem flexibility is lower and orbital velocities are more significant due to higher storms occurrence. The biomass loss due to this effect at the measurement location is shared in Figure 5.12. To include the change in vegetation, Vuik et al. [2018b] created a model in which a critical orbital velocity can define for characteristic vegetation, and include a reduction on the wave energy balance. Nevertheless, this was not included in the present analysis as similar bulk dissipations were measured before and after breakage in [Vuik et al., 2018b], and the effect of shorter vegetation in the spectral transformation is discussed in the upcoming sections.

Figure 5.12: Picture of the site of study in January 2015. Taken at the east from the transect and on top of the dike slope facing seawards. Note the location of the sensor p5 in the red circle during retrieval after the storm. (Data obtained from Vincent Vuik)

5.2. Model Description

The model for the site of study has been created to reproduce the generation, transformation, and dissipation of waves from a coarser model with buoy and atmospheric information, to finer calculations for local projects and prediction of research conditions. Nesting grids of different resolutions can obtain this. In this case, a set of four nested grids is described in the project information, as shown in Figure 5.13, computing from the North Sea and the Wadden Sea to the location of interest. The nested grids G01 and G02 are used in the present investigation to test explicit and implicit modeling over submerged vegetation. As observed in Figure 5.14, the transect and presence of vegetation is a small fraction of the finest grid (G02). The reference system is based on the Dutch Reference system (RD).

Figure 5.13: Computational Grids used for SWAN nested modeling on the research site. G01 and G02 were used during the validation and comparison investigation of this report. (Data obtained from project input files and Steetzel et al. [2018]).

The SWAN model's settings from the *Effectiviteit Voorlanden HR* project [Steetzel et al., 2018] are here described and kept for the present analysis. The 2D nested model grids (G01, G02) use the stationary mode and nautical coordinates. The spectral space was defined from 0.03 up to 2.00 Hz. No significant amount of energy was observed above the higher limit in the spectral processing (1.00 Hz), and 2.00 Hz is expected to be sufficient for the present wave computations. Nevertheless, around the lower limit, widely spread energy is present. The SWAN team [2019a] recommends defining the lower limit where energy is no longer present. This is discussed in the present report but not modified as energy is already 0 m^2 at 0.03 Hz from the boundary conditions provided by coarser grids. The number of frequency bins is left for SWAN to determine the minimum requirement according to the DIA method (an approximation of non-linear 4-wave interactions), which for this case in sigma-space is MSC-1 = 44 leading to df/f = 0.1. Even though the model over the transect shallow conditions would not generate quadruplets, the model nested grids embrace a larger area in which this mechanism could be relevant. Spatial and input grids (e.g., bottom, wind, currents) are curvilinear and use the boundary conditions at the storm's peak time. The value of this temporal input variables, as shared in Steetzel et al. [2018], is shared in Appendix D.
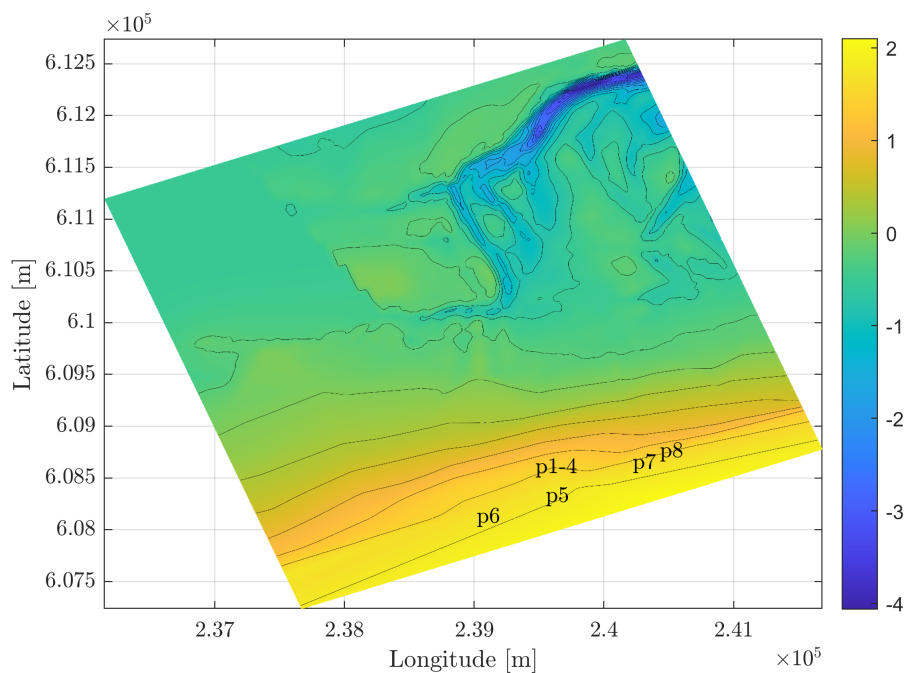
Figure 5.14: Nested G01 bathymetry represented by the color elevation setting the elevation zero reference with the Normaal Amsterdams Peil (NAP). Latitude and Longitude Datum based on the Dutch reference system (RD) in meters. Contour lines are 0.25 m from each other. Sensor stations during the 2015 are included for comparison. Modeled marsh vegetation is only present in elevations higher than p1

The physics of the third-generation, based on Komen et al. [1984], are here described. The input source term uses the wind drag formulation from Wu [1982] and white-capping from Komen et al. [1984]. The non-linear interactions are represented by the DIA model of Hasselmann et al. [1985] for quadruplets and the LTA method of Eldeberky and Battjes [1996] for triads. The quadruplets use the fully explicit computation of the non-linear transfer with DIA per sweep becoming inactive when the Ursell Number exceeds a value of 10. In the user manual [The SWAN team, 2019a], the option per iteration instead of per sweep is recommended when ambient current is included (as it is the case in this simulation). Depth-induced breaking uses the model from Battjes and Janssen [1978] with γ of 0.73.

The bottom friction model uses the JONSWAP results from Hasselmann et al. [1973] with its default value. To model vegetation with the implicit approach, this model must be exchanged for Collins [1972] or Madsen et al. [1988]. To avoid introducing differences where vegetation is not present, the default values are used ([cfw] = 0.015 and [kn] = 0.05). The default friction coefficient of Madsen et al. [1988] seems to be high for non-vegetated areas with fine sediments. This is discussed with the results at the marsh edge. Other friction coefficients will be provided and calibrated for the vegetated area. The explicit models from Suzuki et al. [2011] and Jacobsen et al. [2019] interact with the default bottom friction model settings, which does not include vegetation. The vegetation properties for explicit modeling of both storms, as discussed in Section 5.1, are h_v = 0.5 m, b_v = 0.0013 m, and N_v = 1000 stems/m^2. The calibration coefficients for friction (implicit) and drag (explicit) models are included in the upcoming section.

5.3. Comparison

Vegetation implicit and explicit modeling are compared to field measurements and activated as mentioned earlier. An input grid with values of 1 (and 0) where vegetation is (not) present, allows the SWAN explicit models to assign vegetation dissipation only where required. This also assumes that no horizontal variations in vegetation density are introduced in the model. For the implicit models, a special grid has was created for each. Instead of 0 values, the default values for each model where vegetation is not present are used, and the calibrated value of [cfw] or [kn] instead of 1. The calibration objective was to fit the energy at the near dike station, where the spectral differences will be compared. The coefficients from this process are summarized in Table 5.2 and compared in Figure 5.15 and 5.16.

An initial mismatch with overestimation of H_{m0} and underestimation of the $T_{m,01}$ is present at the marsh edge. The grids G01 and G02 cover an area much larger than the transect of investigation, meaning that any modifications to tune the energy at this point might lead to erroneous results at other sites. Also, the Wadden Sea is an extremely complex system. The mismatch at p1 might differ per modeled conditions, as it is possible to see between 2017 and 2015. An overprediction of dissipation is required in the pioneer zone to cope with the initial mismatch. This initial mismatch will be accepted as a starting point for the present research, but its possible reasons and effects are discussed.

Calibration Parameters for Field Measurements

Storm ID	Date and Time	SWAN Model	Coefficient
2015	11th of January at 01:00-01:15 h	Jacobsen et al. [2019]	[CD] = 0.96
		Suzuki et al. [2011]	[CD] = 0.90
		Collins [1972]	[cfw] = 0.615
		Madsen et al. [1988]	[kn] > 1.57 A_b
2017	13th of January at 22:00-22:15 h	Jacobsen et al. [2019]	[CD] = 1.20
		Suzuki et al. [2011]	[CD] = 1.10
		Collins [1972]	[cfw] = 0.615
		Madsen et al. [1988]	[kn] > 1.57 A_b

Table 5.2: Calibration parameters of the drag and friction coefficients for the storm peak of 2015 and 2017 per dissipation model in SWAN.

The model from Madsen et al. [1988] could not reproduce the strong dissipation as also experienced in previous analyses. This is caused by the numerical limitation in SWAN [Jonsson, 1966], which limits the friction factor to 0.3 if the A_b/k_N ratio is lower than 1.57. As observed, the Nikuradse number is in the denominator, which, if increased, will not make any difference in the dissipation output of the model. Nevertheless, the model results are still included in the discussion as it provides an essential conclusion towards its applicability. The used friction coefficient for Madsen et al. [1988], discussed in the previous section, results in a slightly lower total energy at the marsh edge than the other models. Nevertheless, as the bulk dissipation could not be reduced within the transect, this is not modified.

Studies (e.g., Lowe et al., 2007, Beudin et al., 2017) have confirmed that flexibility alters the drag forces of vegetation. The obtained calibration values are theoretically high for flexible vegetation if compared to the rigid cylinders drag coefficients from Chapter 4, and the standard Manning and Nikuradse roughness values. The Nikuradse values obtained from the Manning roughness Wamsley et al. [2010] coefficients following Bretschneider et al. [1986] range between 0.012 and 0.054 m for marsh vegetation under 2 m of water depth Vuik et al. [2018a]. This upper value is close to the default value of Madsen et al. [1988] in SWAN ([kn] = 0.05). Nevertheless, these coefficients have been obtained for unidirectional flow. Studies have confirmed the considerable differences between steady flow and wave forcing for stem motion (e.g., Bradley and Houser, 2009, Hansen and Reidenbach, 2012). Grass vegetation has been reported to move with low frequencies but behave rigidly and out of phase near the peak frequency. The deeper submergence causes orbital amplitudes to reduce when reaching the top of the canopies (if an intermediate or deep regime), causing them to favor swaying out of phase to the wave component than when closer to the water surface.

Besides, a large variability between vegetation properties has been discussed in the previous section. A rough estimate of the diameter and height determined the density for one dry biomass sample. The uncertainties and deviation of these values will impact the calibration of the drag coefficient. Denser vegetation or thicker stems could be present in other parts of the foreshore, as shown in Table 5.1. Besides, the initial mismatch requires the models to assign stronger dissipation to the processes happening over the transect. Therefore, it is assumed that the drag coefficients are correct in the present calibration by considering the additional drag to compensate for the initial energy difference, the variability observed in vegetation properties, and the different behavior of flexibility in waves than in steady flow.

The large range of bottom friction factors from Collins [1972] was discussed in Chapter 4. The [cfw] changed from 4.70 to 7.40 for $h_v/d = 0.65$ and from 6.50 to 220 for $h_v/d = 0.92$. In this analysis, the same bottom friction was enough for the calibration in both storms. This is caused by a lower level of submergence ($h_v/d \sim 0.25$), which gets closer to the range of values the model was made for. Therefore, it is concluded that the high sensitivity of Collins [1972] factors holds only for high values of relative submergences.
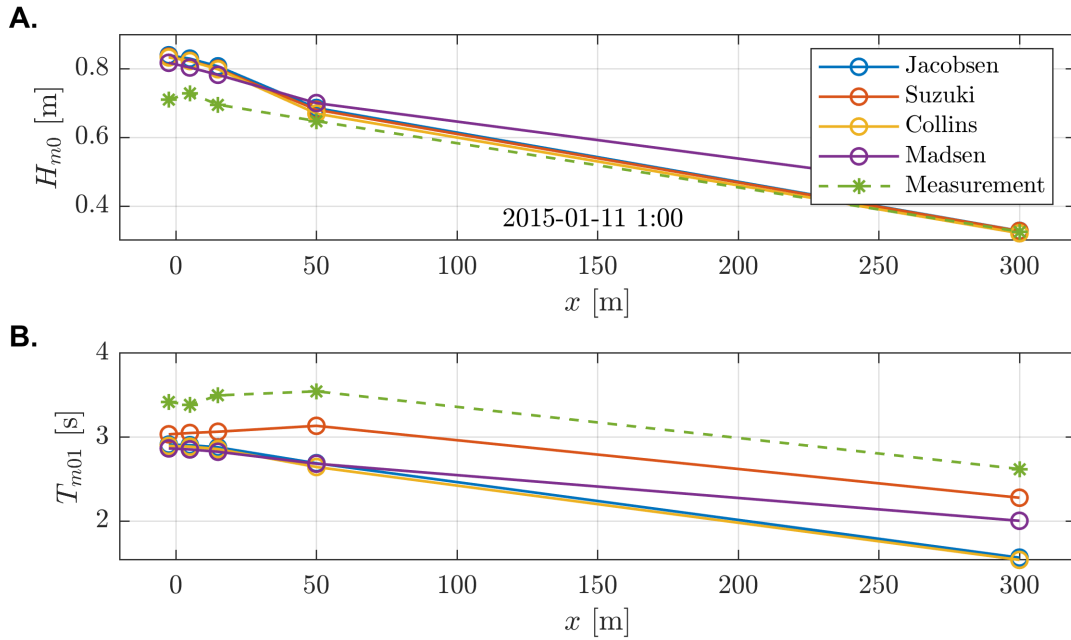
Figure 5.15: **A.** Significant wave height and **B.** Mean Period $T_{m,01}$ evolution of measurements and models between transect's stations p1-p5 at -2.5, 5, 15, 50, and 300 m for the storm of the 11th of January 2015 at 01:00 h.
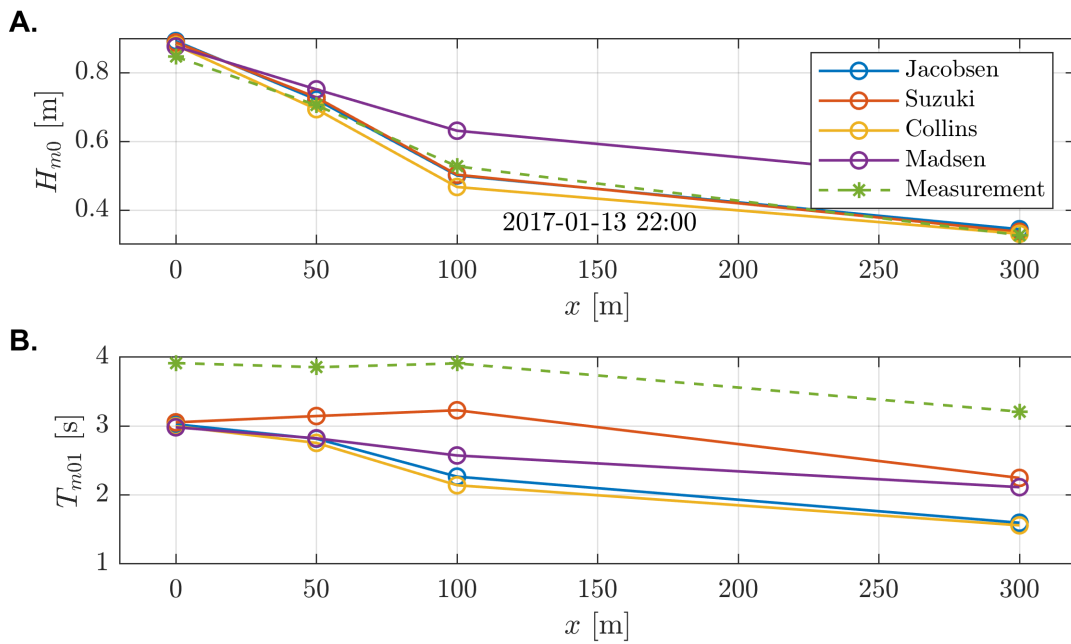
Figure 5.16: **A.** Significant wave height and **B.** Mean Period $T_{m,01}$ evolution of measurements and models between transect's stations p1-p4 at 0, 50, 100, and 300 m for the storm of the 13th of January 2017 at 22:00 h.

The total mean period evolution (ΔT_m) of all models show a decrease between the first and last station, which corresponds to the measurements. No substantial magnitude changes occur in the pioneer zone, but a slight increase was visible in 2015. The model of Suzuki et al. [2011] was the only model simulating the period increase at 50 m from the marsh edge in 2015. The rest showed more relative weight at higher frequencies. The new implementation and the implicit model from Collins [1972] evolved similarly, showing the correlation to the results over submerged canopies in Chapter 4. The reasons behind the mean period evolution are analyzed by looking at the distribution of energy in Figure 5.17 and 5.18.

The station near the dike is the most impactful for assessing the dikes design criteria, maintenance, and failure probability. Therefore, the mismatch at this location is the center of the comparison. The energy left at this station is only ∼ 10-20 % than the incoming wave energy at the marsh edge. Intermediate processes at other stations could help understand the dissipation mechanisms that could be missing in SWAN for better outputs.
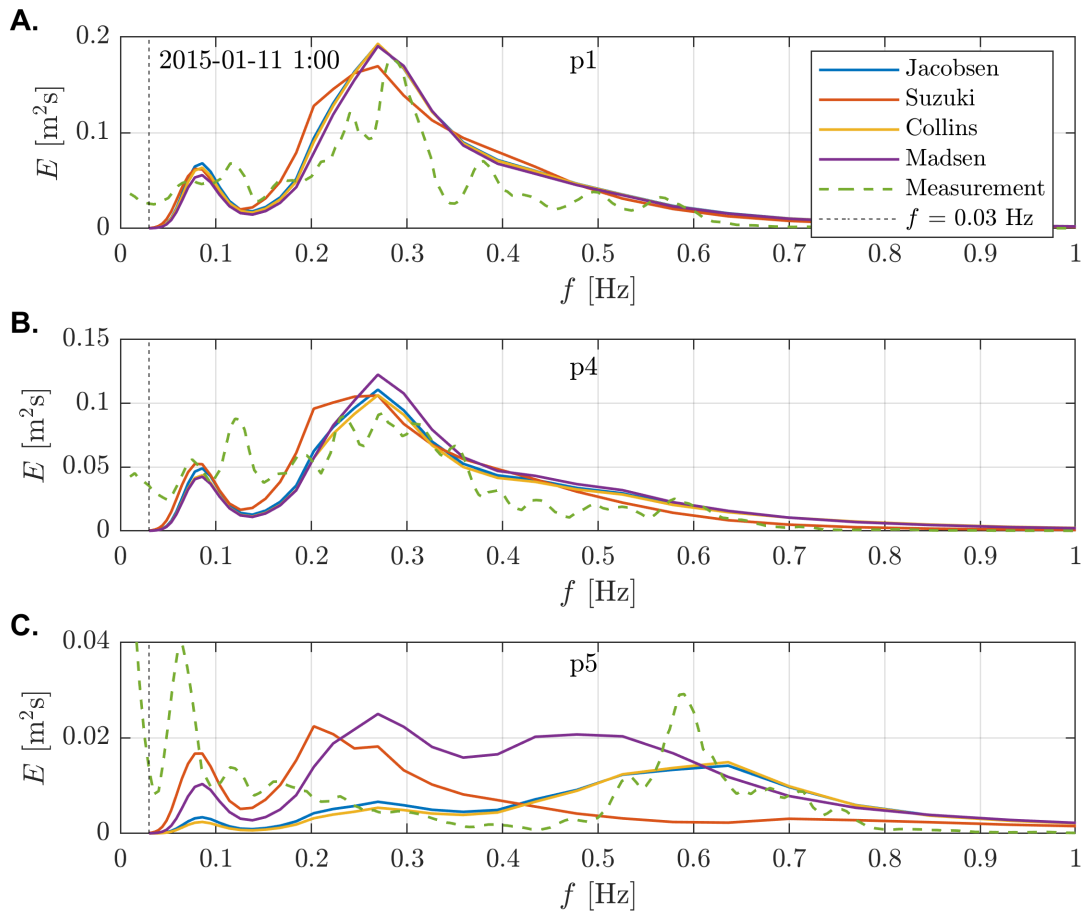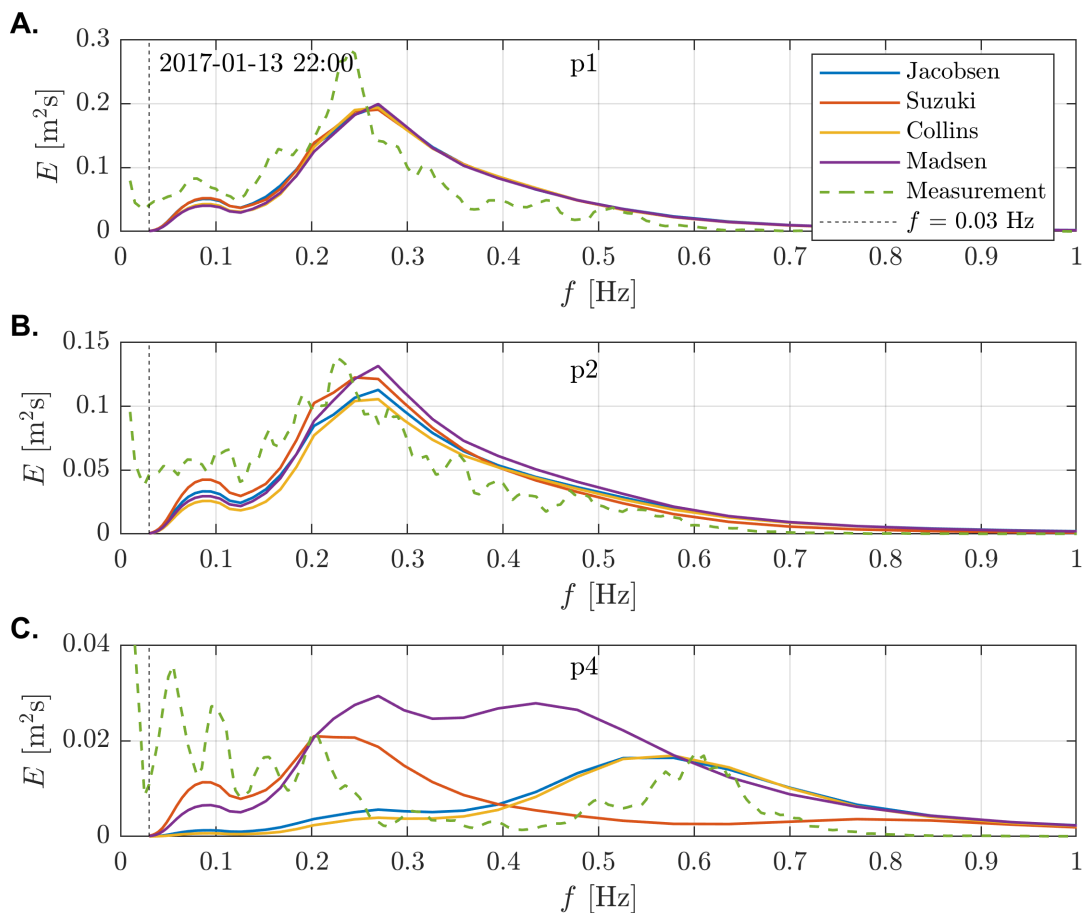

Figure 5.17: Spectra comparison between models and measurements for **A.** p1 (2.5 m before marsh edge), **B.** p4 (50 m from marsh edge), and **C.** p5 (near dike, 300 m) for the storm of the 11th of January 2015 at 01:00 h. Note the different scale of the figures.

The large deviations between models are triggered by the dependency of the dissipation on the individual wave components. As observed in Chapter 4, both frequency-dependent models of Collins [1972] and Jacobsen et al. [2019] will decrease their mean period by retaining the energy on high frequencies for submerged vegetation. The regime in which these components are (intermediate to deep), causes that the orbital velocities at the elevation point where the stems are (∼ 0.5 m from the bed and ∼ 1.5 m from the water surface) to be very small and not significantly affected. The model from Suzuki et al. [2011] showed in the experimental validation that for submerged vegetation, the wrong mean period evolution was predicted. This is

Figure 5.18: Spectra comparison between models and measurements for **A.** p1 (2.5 m before marsh edge), **B.** p2 (50 m from marsh edge), and **C.** p4 (near dike, 300 m) for the storm of the 13th of January 2017 at 22:00 h. Note the different scale of the figures.

caused by the equally distributed dissipation factor that affects the energy at all frequencies, causing the little energy to almost vanish at high frequencies. The same is observed in this case, where the multiplicative factor assigns dissipation to the energy present in the incoming spectra, over-dissipating high frequencies, and under-dissipating low and mid-range frequencies.

The spectral evolution shows that the new model performed very closely to the implicit model of Collins [1972], capturing the right order of dissipation required in the wind sea region (0.2-0.5 Hz) and following the same qualitative evolution for the high frequencies. With the opposite result, the model from Suzuki et al. [2011] does not capture the qualitative evolution at these frequencies. Besides, it significantly reduces the energy after 0.5 Hz. An investigation of the model outputs without wind is shared in Appendix F, concluding that the energy present in those frequencies for Suzuki et al. [2011] is merely attributed to this source term. Also, without wind the mean period of Suzuki et al. [2011] evolved to the opposite side than the measurements (and rest of models) for submerged vegetation, as observed in Chapter 4.

The results from Suzuki et al. [2011] in Figure 5.17 and 5.18 show more energy at f < 0.10 Hz than other models. Nevertheless, this occurs due to the wrong reasons as a conservation of energy in low frequencies is not consistent with the physics behind the interaction of rigid canopies with wave components from Dalrymple et al. [1984]. The energy at low frequencies increases its weight as the dissipation by mean properties damp energy relative to the mean frequency value. That means that, even though all frequencies face dissipation, the low frequencies dissipation is characterized by a mean value assigning under dissipation while the opposite for high frequencies. Also, as dissipation is equivalent to the incoming energy, frequencies with more energy (peak-mid values) will experience more dissipation than the rest. This explains the gained rel-

ative weight of low frequencies compared to the rest of the spectra from Suzuki et al. [2011]. The possible causes of the generation and retention of energy in measurements at frequencies lower than 0.15 Hz are addressed in the upcoming discussions of this Chapter.

The measurements show almost no energy after 0.8 Hz because of the inaccuracy of pressure sensors with high frequencies at high water depths, the correction factor from the pressure to amplitudes (based on linear wave theory) was limited up to a particular frequency to prevent scaling up noise. The models (with a spectral upper limit of 2.0 Hz) have a more gentle slope in the high-frequency tail. The additional relative weight of energy on those frequencies could be contributing to the mean period mismatch between measurements and SWAN in Figures 5.15 and 5.16. The model of Suzuki et al. [2011] had the closest mean period prediction to the measurements. Nevertheless, if the spectral evolution is observed, it can be deduced that the model does not capture the qualitative behavior of the spectral transformation. The measurements near the dike show a spectrum with two peaks, in which their average matches the mid-peak frequency result of Suzuki et al. [2011].

The changes between the frequency distributed variance of each station help to investigate the processes within the transect, as shown in Figures 5.19 and 5.20. The spectra at the marsh edge is different between models and measurements. As this is significant in some frequencies (eg., $f < 0.1$), this is likely to impact the spectra near the dike. Analyzing the qualitative energy decay per frequencies contributes to evaluating the models' performance in the present case.
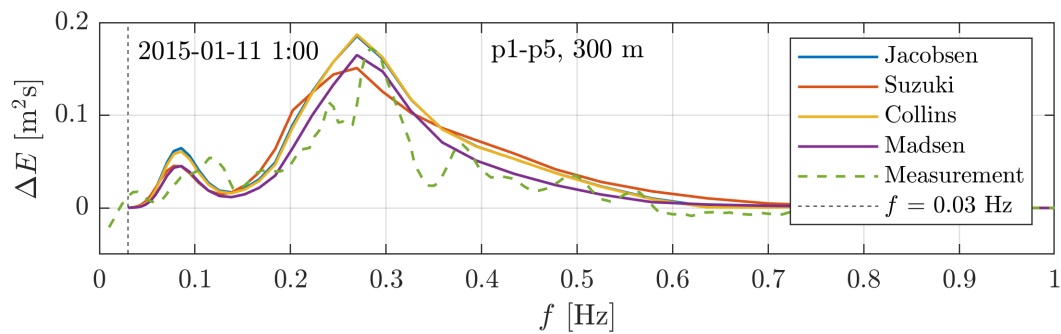
Figure 5.19: Distribution of the energy decay of measurements and models in the marsh for the storm of the 11th of January 2015 at 01:00 h.
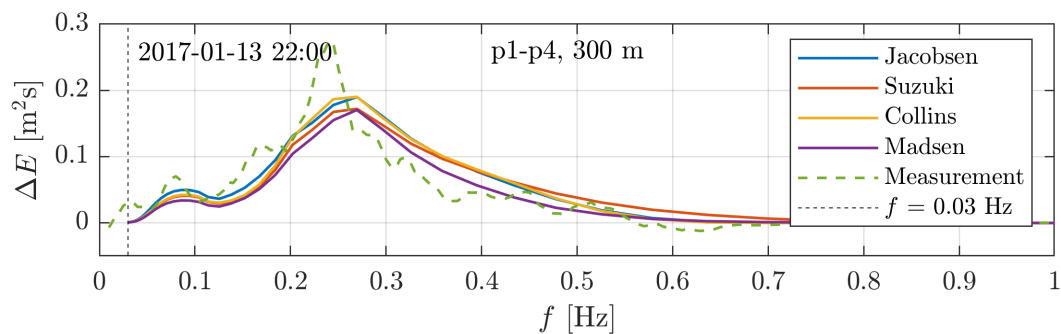

Figure 5.20: Distribution of the energy decay of measurements and models in the marsh for the storm of the 13th of January 2017 at 22:00 h.

The spectral shape near the dike from Figures 5.17 and 5.18 show a larger relative amount of energy in low frequencies by the measurements than models. Despite this fact, the energy decay in Figures 5.19 and 5.20 shows that the decay below 0.08 Hz is significantly less in measurements than by models. Especially Jacobsen et al. [2019] and Collins [1972] assign more energy decay to this point in 2015. The combination of more energy in low frequencies at the marsh edge, and the over dissipation of models on that range of values, results in the significant mismatch discussed near the dike. Nevertheless, the order of magnitude of energy decay for 2017 seems to be best replicated by Jacobsen et al. [2019]. In spite of, this was not enough to reduce

the mismatch in the low-frequencies range as the initial mismatch still plays a significant role. The mismatch at the marsh edge in these ranges of values is larger in 2017 than in 2015, causing a better match of the new model's energy decay.

Even though the model from Madsen et al. [1988] is not included in the discussions, as the calibration was not sufficient, Figure 5.19 could indicate its match to the energy decay of measurements. All other models overestimate the energy decay in the high-frequency tail, while Madsen et al. [1988] gets the closest. Nevertheless, the model experiences less bulk dissipation, which makes it match better than the rest due to the wrong reasons. Therefore, it is advised to be aware of the incoming energy shape and total bulk dissipation when drawing conclusions from these results.

The high-frequency tail mismatch in the energy decay is assumed to be caused by the role of wind input and non-linear interactions. Energy increases for frequencies over 0.6 Hz, which is not reproduced by any model in SWAN. Local wind velocities or gusts could have been stronger than average values during the 15 min time series analyzed on these spectra. An investigation over the role of wind in SWAN is discussed in Appendix F.

5.4. Additional Mechanism(s) in Model

The new implementation in SWAN has shown improvements during the experimental validation. The formulation favors the dissipation of frequencies with larger orbital velocities that experience the presence of rigid canopies. Nevertheless, in the site of study, highly flexible vegetation is present. Riffe et al. [2011] confirmed that wave modeling over salt-marsh vegetation is improved by considering the stem motion. Therefore, including this vegetation property is a natural step towards further improvements. Modifications and possible improvements to the newly implemented model are investigated considering the reported mechanisms in the literature and observed in the field measurements.

Studies have reported the drag coefficients of rigid elements in a wave flume setup to double the bulk drag of salt-marsh vegetation in the field Riffe et al. [2011]. Nevertheless, other studies concluded that live vegetation presented larger coefficients than flexible and rigid artificial models [Ozeren et al., 2014]. This highlights the complexity in the plant's change of geometry with the wave periods, altering the drag and inertial forces.

Effective Length for flexible vegetation

The reduction of bulk dissipation by the stem flexure has been approached in large scale modeling by Luhar and Nepf [2011] and Dijkstra [2008]. Both studies have developed models to determine the effective posture of the stem against steady flow. The effective length is estimated with the flow velocities and stem properties. Because the stem response to steady flow significantly differs from orbital velocities, an initial number is arbitrary chosen to understand this approach's spectral effects. In the present investigation, the vegetation height has been reduced 50 %, and the drag coefficient doubled to conserve the bulk energy calibration. This modification factor is defined as the vegetation factor V_f in the present document. The model is represented by the original formulation of Jacobsen et al. [2019] with different parameter values to include this approach.

$$S_{ds,veg_J}(\sigma,\theta) = -\frac{1}{g}\sqrt{\frac{2}{\pi}}\alpha_u^3 C_D * b_v N_v * \int_{-d}^{-d+h_v*}\sqrt{m_{u,0}}(\frac{\sigma \cosh k(z+d)}{\sinh(kd)})^2 dz * E(\sigma,\theta) \ \ [\text{m}^2] \quad (5.2)$$

where

$$h_v = V_f h_{v,meas} = 0.5 h_{v,meas} \tag{5.3}$$

$$C_D = \frac{C_{D,calib}}{V_f} = 2C_{D,calib} \tag{5.4}$$

with

$$a_u = 1.0$$

Constant Reduction Factor

Vegetation is capable of reducing the velocity within the stems [Hansen and Reidenbach, 2012] and generating a shear layer if vegetation is dense [Nepf, 2012]. This is included in the in-canopy velocity reduction factor, which strongly depends on drag and inertial forces [Luhar et al., 2010]. Up until now, $\alpha_u = 1$ has been used for the dissipation model of Jacobsen et al. [2019]. This was decided for model comparison reasons and because not sufficient information is available to define a specific value in the present cases. During the experiments in Jacobsen et al. [2019], α_u was fairly constant over frequencies. Therefore, a constant reduction factor is investigated here.

In-canopy reduced velocities have been reported to change largely Luhar et al. [2010]. An initial reduction factor with α_u of 0.85 (85 % of the velocity without canopies) is chosen based on the 70 % and 90 % in-canopy velocity from Hansen and Reidenbach [2012]. This results due to the cube power in a total dissipation reduction of $\sim$ 61%. The reduction has been limited to certain frequencies as the wind sea region has been properly estimated. Defining reduction under $kd = 0.8$ would mean for the field conditions, that frequencies bellow 0.35 Hz will be less dissipated. This is the deflection point in which the energy near the dike starts to increase towards lower frequencies Figures 5.17 and 5.18. Even though this threshold fits for the present data, further investigations would be required to determine a robust limit between reduction factors. The model version with a constant reduction factor reads:

$$S_{ds,veg_J}(\sigma,\theta) = -\frac{1}{g}\sqrt{\frac{2}{\pi}}\alpha_u^3 C_D b_v N_v * \int_{-d}^{-d+h_v} \sqrt{m_{u,0}}(\frac{\sigma \cosh k(z+d)}{\sinh(kd)})^2 dz * E(\sigma,\theta) \quad [\text{m}^2] \quad (5.5)$$

where

$$\alpha_u = 1.00 \qquad\qquad\qquad\qquad kd > KD_{LIM} \quad (5.6)$$

$$\alpha_u = 0.85 \qquad\qquad\qquad\qquad kd \le KD_{LIM} \quad (5.7)$$

with

$$KD_{LIM} = 0.8$$

Frequency dependent reduction factor

In the present measurements, the energy decay at low frequencies shows a decrease in dissipation. Vegetation has been reported to have little dissipation effect on low-frequencies (e.g., Bradley and Houser, 2009, Hansen and Reidenbach, 2012, Zhu and Chen, 2018). The explanation behind this is the phase relation between the stem motion and wave components. It has been observed that submerged grass vegetation was in phase for long components (f < 0.38 Hz) and out of phase near the peak energy (0.67 Hz) [Bradley and Houser, 2009]. Larger amplitudes allow the stem to bend, reducing the dissipation for those frequencies. If stems are out of phase or very small orbital amplitudes are present, the vegetation tends to behave like rigid elements.

Frequency-distributed drag coefficients have been obtained in different investigations, concluding that wave modeling over vegetation can be improved if spectral drag coefficients instead of a constant value Jadhav et al. [2013]. The change of geometry due to flexibility will largely impact the in-canopy velocity reduction, causing that some studies attribute the spectral reduction factor while others to flexibility alone. The magnitude and shape of reduction factors largely vary in the literature, as their definition does (e.g., Lowe et al., 2005, Luhar et al., 2010, Hansen and Reidenbach, 2012, Nepf, 2012, Jadhav et al., 2013).

The attenuation factor from Jadhav et al. [2013] uses the frequency-dependent rigid canopies model from Chen and Zhao [2012] to define a frequency-dependent drag coefficient $C_D \alpha_{n,j}^2$. The squared reduction factor $\alpha_{n,j}$ was assumed to be independent of water depth and is estimated by the reduction of mean and root mean square velocities within the canopies. The obtained attenuation parameter from measurements, in Figure 5.21, ranges from $\alpha_{n,j} \sim 0.5$ for $f \sim 0.05$ Hz, to $\alpha_{n,j} \sim 1.0$ for frequencies larger than 0.2 Hz. These values were obtained from field measurements with flexible marsh vegetation. Therefore, the subscript of α_u related to velocity is changed to α_v to note the inclusion of more processes in flexible vegetated fields.

Frequency-dependent drag coefficients tend to minimal values with lower frequencies. If the results from Jadhav et al. [2013] are used as an initial reference, it reduces the dissipation with $\alpha_n^2 \sim 0.25$ factor for $f \sim$
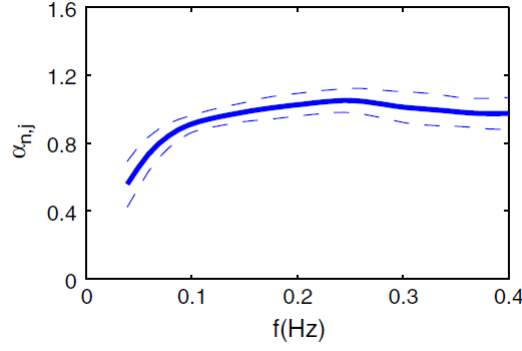
Figure 5.21: "Spectral variation of ensemble-average velocity attenuation factor parameter, α_n, based on 118 spectra. Dashed lines represent standard deviation." [Jadhav et al., 2013]. This reduction factor is based on Chen and Zhao [2012] model to determine the frequency-dependent drag coefficient in Jadhav et al. [2013]. (From Jadhav et al., 2013)

0.05 Hz. If extrapolated, this value is expected to decrease even more for longer components. Therefore, an initial formulation that depends on the frequency or wave number is here implemented. The form here described was not derived from theory or representative of the physics in the reduction mechanism but merely an approximation. This model modification investigate if the vegetation reduction factor a_v, like involving mechanisms as flexibility and in-canopy velocity reduction, could improve large-scale modeling over flexible vegetation in storms. Two versions with (out) the cubic power of the reduction factor are implemented to understand the velocity-reduction relation in the formulation.

$$S_{ds,veg_J}(\sigma,\theta) = -\frac{1}{g}\sqrt{\frac{2}{\pi}}\alpha_v^3 C_D b_v N_v * \int_{-d}^{-d+h_v} \sqrt{m_{u,0}}\left(\frac{\sigma\cosh k(z+d)}{\sinh(kd)}\right)^2 dz * E(\sigma,\theta) \quad [m^2] \quad (5.8)$$

where

$$\alpha_v = 1.00 \qquad\qquad kd > KD_{LIM} \quad (5.9)$$

A.

$$\alpha_v^3 = C_{D,low} + (1 - C_{D,low}) * \frac{kh}{KD_{LIM}} \qquad kd \leq KD_{LIM} \quad (5.10)$$

B.

$$\alpha_v = C_{D,low} + (1 - C_{D,low}) * \frac{kh}{KD_{LIM}} \qquad kd \leq KD_{LIM} \quad (5.11)$$

with

$$KD_{LIM} = 0.8$$

$$C_{D,low} = 0.2$$

Validation with measurements

These new versions are tested and validated against the storms of 2015 and 2017. The constant or frequency-dependent reduction versions alter the same drag coefficients than obtained from the calibration with the original model of Jacobsen et al. [2019]. This provides an insight into how sensitive the bulk and spectral dissipation can be for these cases. The most considerable bulk difference between models near the dike was attributed to equation 5.11. An example of the impact on the bulk dissipation by these models is visualized in Figure 5.22. Considering these bulk differences, the spectra at the end of the vegetated field and near the dike is compared to the models results in Figures 5.23 and 5.24.
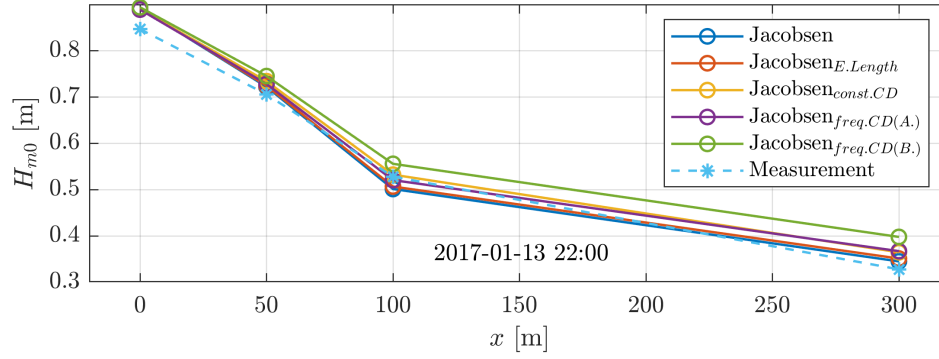
Figure 5.22: Significant wave height evolution of measurements and modified models based on Jacobsen et al. [2019] between transect's stations p1-p4 at 0, 50, 100, and 300 m for the storm of the 13th of January 2017 at 22:00 h.
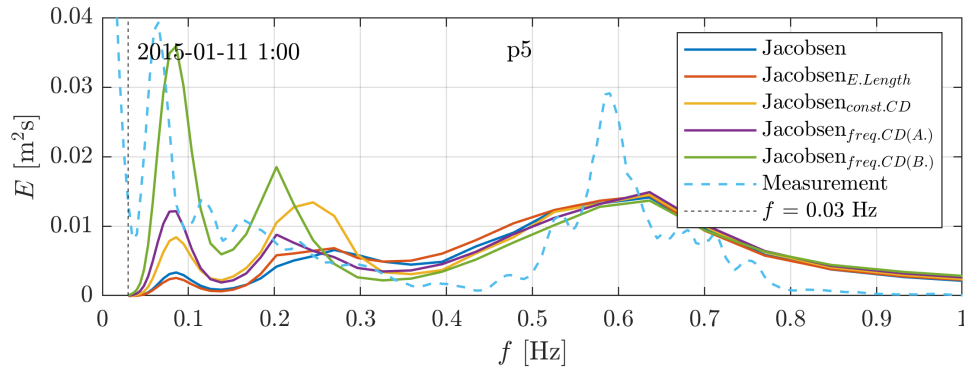

Figure 5.23: Spectra comparison between Jacobsen et al. [2019] original model, modifications and other modeling approaches to measurements for p5 (near dike, 300 m) during the storm of the 11th of January 2015 at 01:00 h.
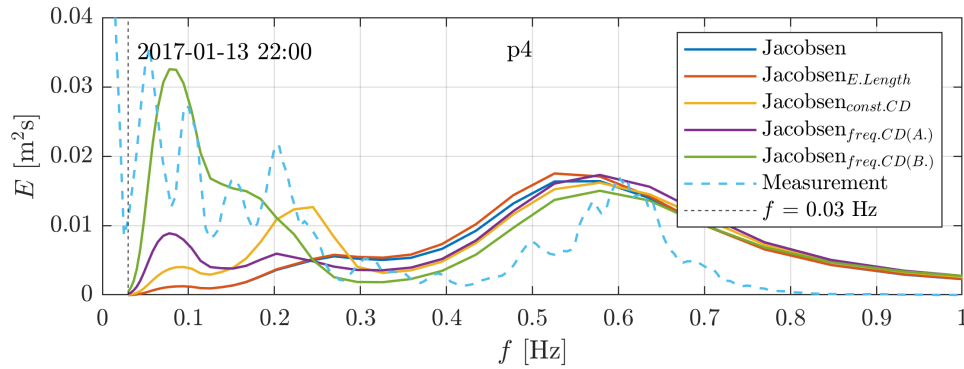

Figure 5.24: Spectra comparison between Jacobsen et al. [2019] original model, modifications and other modeling approaches to measurements for p4 (near dike, 300 m) during the storm of the 13th of January 2015 at 22:00 h.

The model modifications using the frequency-dependent reduction factor of equations 5.10 (version A) and 5.11 (version B), reproduce the qualitative shape of the spectra by capturing the energy peaks in low and high frequencies. The model with a constant reduction factor was not capable of this. Even though constant values for the velocity reduction factor have provided good results for experimental validations, other processes have been reported to be crucial in the field (e.g., flexibility phase relationship with wave components). The effective length showed little differences to the original approach with Jacobsen et al. [2019] at the end of the transect. These are mainly present at high frequencies, as the submergence of vegetation affects the components with which orbital velocities interact with the model, allowing more energy to remain in high-frequencies. As discussed, reducing the vegetation height does not change the preference to dissipate components with stronger velocities near the submerged canopies (long waves). Throughout the transect,

the effective length approach showed significantly larger dissipation in the pioneer zone than measurements and other models, as a larger drag coefficient was used.

The two new versions of frequency-dependent factors show the best qualitative results from the present modifications, and are further investigated with the energy decay shape displayed in Figures 5.25 and 5.26. The incoming spectra at the marsh edge of measurements and the original model of Jacobsen et al. [2019] are included to facilitate the comparison and discussion.
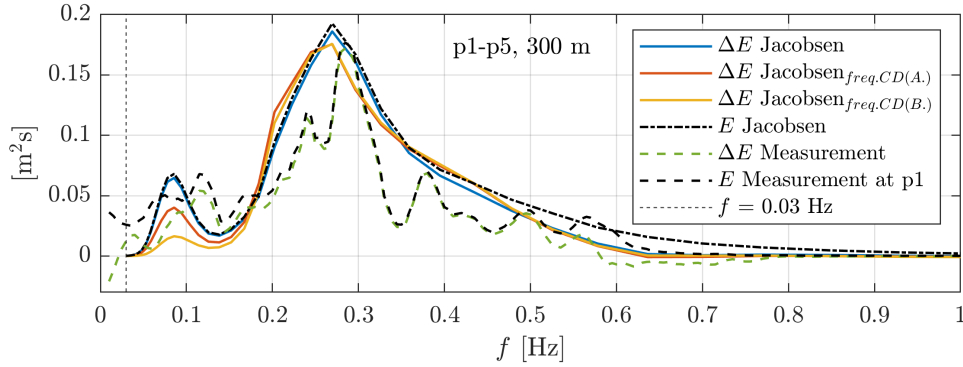
Figure 5.25: Distribution of the energy decay of measurements and spectral reduction factors for models based on Jacobsen et al. [2019] in the vegetated transect (p1-p5) for the storm of the 11th of January 2015 at 01:00 h. The incoming energy of measurements and Jacobsen et al. [2019] are included for comparison. (Please note the scale if compared to other figure).
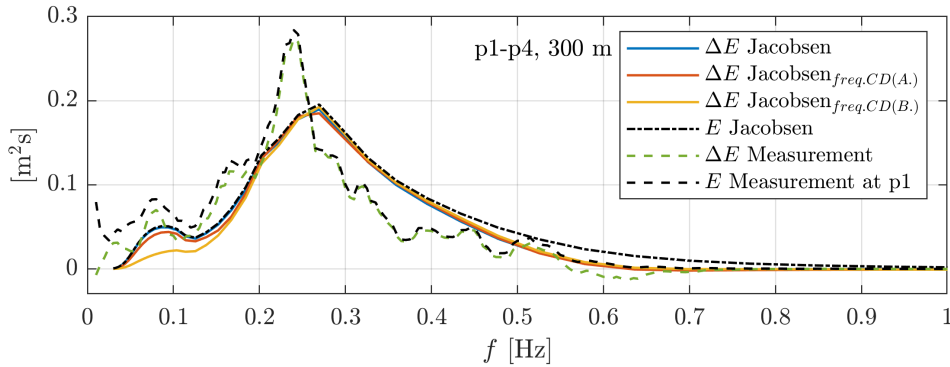
Figure 5.26: Distribution of the energy decay of measurements and spectral reduction factors for models based on Jacobsen et al. [2019] in the vegetated transect (p1-p4) for the storm of the 13th of January 2017 at 22:00 h. The incoming energy of measurements and Jacobsen et al. [2019] are included for comparison. (Please note the scale if compared to other figure).

Comparing the energy decay shape to the incoming spectra provides a clear idea of the magnitude of energy dissipated at each frequency. For both storms, it is possible to see that almost all energy at the peak vanished in the measurements. This is equivalent to the original form of Jacobsen et al. [2019]. Modified versions present a slight deviation due to the defined threshold (~ 0.35 Hz), which alters the dissipation of all frequencies under it. Investigating the model performance with a lower limit (KD_{LIM}) could provide a better fit on this range of frequencies.

In addition to the wind sea region, all model versions based on Jacobsen et al. [2019] predicted the high frequencies decay if compared to the incoming spectra. This is attributed to the values of the velocity profile with highly submerged vegetation. In low frequencies, larger differences are observed. The spectral α_v of version B shows a stronger reduction towards low frequencies than compared to version A. The reduction seems appropriate for the storm of 2017 in Figure 5.26 but excessive for 5.25. The specific form and frequency-dependent power must be investigated for further model improvements.

The reduction of dissipation in low frequencies in the measurements confirm the findings from previous studies (e.g., Bradley and Houser, 2009, Hansen and Reidenbach, 2012, Zhu and Chen, 2018), and highlights the importance of including this in vegetation modeling. The original form of Jacobsen et al. [2019]

dissipates most of the energy present in low frequencies as rigid canopies are assumed. The dissipation of each frequency will be dissipated by the interaction between the individual velocity profile and the canopy's presence in the model. Including the modified versions with the first forms of the frequency-distributed reduction factor α_v, which empirically introduces the effects of flexible stems phase relationship with wave components, have shown the best match for flexible salt marsh modeling.

5.5. Energy in Low Frequencies

A big unknown remains on the explanation of energy below the wind sea region (< 0.2 Hz). In the measurements, the energy is widely spread at these frequencies, while all SWAN models' energy starts increasing from 0.03 Hz, causing mismatch at this point. The importance of the initial spectra has been highlighted through this report. Even though a model captures the right amount of dissipation, the shape will differ at the end of the domain if significant differences were present at the origin. This especially if the energy at the comparison station is just a small part of the incoming wave field. Investigating the reasons for this low-frequency energy is crucial to reduce the mismatch near the dike in future predictions. Besides, increasing our understanding of these long waves' physics could lead to different model developments, as vegetation might respond differently to different long-wave processes.

Four main reasons might cause the presence of energy on these frequencies: long waves coming from The North Sea, non-linear wave-wave interactions pumping energy to lower frequencies, Infra-Gravity (IG) waves, and measurements. A slight increase in energy between 0.01 and 0.03 Hz is displayed in both storms. As discussed with the author of the measurements and spectral processing, the energy near 0.01 Hz might be related to the spectral leakage. Performing further in-depth analyses of the pressure measurements (e.g., by-spectral analysis) could help understand if the energy at those frequencies was physically present at the site or if it resulted from data processing. If physically present, local generation mechanisms like non-linear interactions and IG waves could be the reason for them.

The wide channels between the islands Schiermonnikoog, Rottumerplaat, and Borkum could allow waves from the North Sea to reach the site. As the measurements of 2015 and 2017 were done targeting large storm surge, which is highly related to the presence of north winds, waves from these directions are highly possible. Investigating the boundary conditions of the coarser grids would partially help solve if these long components come from the North Sea or if they are locally generated at the Wadden Sea.

Non-linear interactions influence increase for steep waves, as often present during storms. The expressions to describe the resonance between two diamond patterns require that the frequency, wave number, and direction coincide [Hasselmann, 1962]. The DIA method in SWAN approximates this mechanism due to large computational times by considering only two quadruplets per wave component, while in reality, each component interacts in a vast number of combinations Holthuijsen [2007]. The quadruplets settings in this model use the non-linear transfer with DIA per sweep instead of iteration. The second is recommended in [The SWAN team, 2019a] if currents are present. The user-defined limit for this approximation is Ursell Number ≤ 10. Investigating the contribution of quadruplets to lower frequencies in this system would determine their relevance and modeling approach towards reducing the spectral mismatch. With a sloping bed and presence of wave breaking before the marsh edge, triads' relevance should be considered . Especially because they will be much more dominant in the complex area in front of the canopy. Triad interactions generate subharmonics and superharmonics due to resonance or near-resonance conditions [Nwogu, 1995]. The frequency interactions of the widely distributed spectra interact in the generation of low-frequency waves (e.g., surf beat, IG waves).

Infra-Gravity (IG) waves or surf beat are classified with frequencies smaller than 0.05 Hz. The generation of these types of waves is attributed to the transfer of energy to low from higher frequencies and has been identified as an important process for steep wind waves [Battjes, 2004]. These conditions were probably present in the complex Wadden Sea during storms, transferring energy to lower frequencies. Under gentle slopes, the dominant generation mechanism is lead by the interaction of two wave trains with similar frequency and amplitude, while for steeper slopes, the variant breaking point of wave groups transfers energy to IG frequencies [de Bakker et al., 2016]. The steep wind waves of the storm could be interacting with the shallows of the Wadden Sea, which might even cause the bounded wave to free if the individual waves break. Charles Feys [2018] made a computational investigation over the interaction of vegetated foreshores and IG waves, concluding the dominance of IG waves for gentle slopes and the little effect of vegetation on their dissipation.

The widely spread energy at low frequencies shows that more than one mechanism might be involved in the distribution of energy at those values. The complex bathymetry and presence of such a large amount of factors in the Wadden Sea create conditions for various processes. Determining their dominance towards the final spectra is key for further steps. Some generation mechanisms have been discussed in this section, but further research is required. The water level time series of two moments are shared over 10 min to provide an insight into the waves at the site and direction for further research.
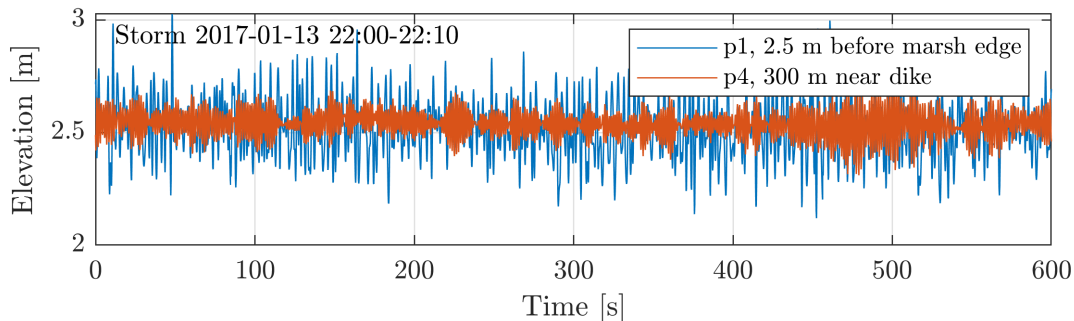
Figure 5.27: Water surface elevation between 22:00 and 22:10 h, around the peak moment of the storm in January, 2017 for the first (p1) and last station (p4) of the study transect.
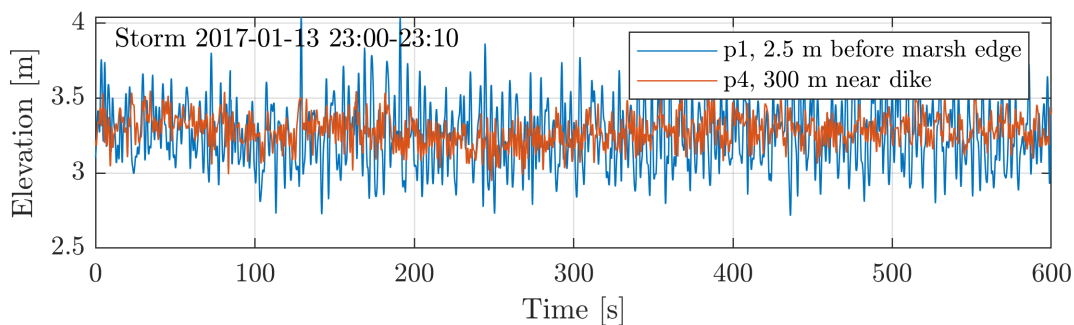
Figure 5.28: Water surface elevation between 23:00 and 22:10 h, around the peak moment of the storm in January, 2017 for the first (p1) and last station (p4) of the study transect.

In Figure 5.28, shorter waves are superimposed on very long waves. The same is not observed in Figure 5.27, where short waves remain next to the still water level. Nevertheless, short waves trains show a wave envelope, as discussed in Figure 5.5, which might lead to the transfer of energy to low frequencies. This process might occur not only near the dike but also in the Wadden Sea. Comparing both time series shows the high complexity of the situation and the requirement for an in-depth analysis of it in the next research.

5.6. Discussion

Describing the site and the measurements contribute to understanding the system. This is crucial before looking at figures and numbers, as this provides an insight into the variability of measurements and the type of phenomena that could be present at the location. Two significant storms were measured with similar spectral evolution, dissipation of most energy present around the peak frequency while conserving very low and high frequencies of the spectrum. The measurements and processing have shared that energy in frequencies higher than 0.8 Hz was challenging to measure with the deeply submerged pressure sensors, and energy in frequencies lower than 0.03 might present spectral leakage. Also, the vegetation properties at the site were determined with one sample. Other detailed studies in surrounding areas have shown that large variability, especially for stem density. Also, the biomass (and density) is altered during the storm as stem breakage occurs Vuik et al. [2018a]. In the present investigation, the pioneer and marsh zone spectral shapes have been investigating, showing that the spectra evolve differently. In SWAN, the vegetation properties are constant between the marsh edge and the dike. This underestimates other processes that might occur, especially in

the first 50 m, where pioneer vegetation is present. Previous studies have shown the improvements of horizontally varying the vegetation properties in the same transect [Post, 2015]. Obtaining more information on the spatial variation of vegetation properties at the site and including them is recommended as a next step.

Implicit (Collins, 1972 and Madsen et al., 1988) and Explicit (Suzuki et al., 2011 and Jacobsen et al., 2019) models have been tested with the measurements of both storms. The model of Madsen et al. [1988] holds a better physical representation of vegetation than other implicit models by using the Nikuradse roughness length. Nevertheless, the model could not reproduce the amount of dissipation required in the present case ($h_v/d \sim 0.25$), showing the limitations from the experimental validation were also experienced under the field conditions with larger submergences. The implicit model from Collins [1972] was capable of reproducing the bulk and spectral dissipation for the present case with smaller submergences than the ones used during the experimental studies. In addition, it was discovered that the large variability of friction factors only occurs on high relative submergences (h_v/d), as this was not encountered in the field validation. This model behaved very similar to Jacobsen et al. [2019] in which the dissipation at the wind sea region (0.2-0.5 Hz) was well estimated. This is related to smaller differences between models for larger water depths in Chapter 4. The explicit model from Suzuki et al. [2011] did not capture the physics and energy distribution of the field measurements. This model defines dissipation with the first-order mean frequency, which results in over-dissipation for high frequencies and under dissipation for peak frequencies with submerged vegetation, as observed here and in Chapter 4.

The spectral mismatch has been analyzed considering the initial differences at the marsh edge. From the literature and discussion over the present Chapter, several processes at the Wadden Sea and over vegetated foreshores have been identified as possible contributions to the mismatch between measurements and the model. These are summarized as:

- Generation of long waves at the Wadden Sea and (or) at the vegetated foreshore.

    i) Non-linear interactions pumping energy to low frequencies

    ii) Infra-Gravity waves

- Ambient Current in the Wadden Sea

- Generation of nearshore currents by vegetation properties horizontal variations.

- Vegetation flexibility.

- In-canopy reduction factor.

The presence of energy redistribution to low-frequencies has been investigated by understanding the conditions that might favor them. In the complex Wadden Sea, conditions like steep wind waves are prone to energy transfer to low frequencies. Triad interactions should be considered as shallow conditions are present in large part of the Wadden Sea and front of the marsh. These conditions are relevant for low-frequency wave generation by triad-interactions [Nwogu, 1995]. IG waves can be generated, depending on the bed slope, which will also in, by the interaction of two wave trains with similar frequency and amplitude de Bakker et al. [2016], and the variant wave breaking of wave groups [Battjes, 2004]. The Wadden Sea presents a mix of gentle slopes due to fine sediments and rapid depth changes between channels and flats, meaning both could occur. The presence of IG waves and non-linear interactions are mechanisms that should be considered in the site of study. Due to the complexity of the data and the time frame of the present research, it is advised to do further research on the relation of these long waves to SWAN modeling at the site.

Ambient current has shown to be significant during the storms of the present validation. The model from Jacobsen et al. [2019] was implemented in SWAN exchanging ω for σ. The effect of this assumption has not been investigated. The intensity of these currents is shared in Appendix D. The Wadden Sea's mean velocities are between 0.0 and 0.5 m/s and nearly zero over the vegetated foreshore. Therefore, a significant deviation is not expected from this assumption for the present analysis. The vegetation implicit models and model Suzuki et al. [2011] performance have not been investigated with wave-current interaction either. It is recommended to perform further research on this topic and to determine the implications for the models. Furthermore, currents also have implications for other source terms. For example, the model settings of quadruplet interactions could be modified following the recommendation of SWAN when currents are present. This has been included in the recommendations of non-linear interactions.

Horizontal variations in vegetation have reported a strong return flow in unvegetated areas for emergent vegetation, maintaining the channel morphology in these types of ecosystems Temmerman et al. [2005]. For submerged vegetation, Ma et al. [2013] and Luhar et al. [2010] reported a strong onshore flow just over the canopies that were compensated by a return flow in the remaining upper part of the water column. This is caused by pressure gradients, large-scale vortices, and wave stresses. Ma et al. [2013] used the experiments of Dubi and Tørum [1995] to create a 3D computational model with vegetation submergences of h_v/d = 0.2 to 0.5. In the present project at Groningen, we have 1-2 m of water on top of the 0.5 m marshes (h_v/d = 0.25 to 0.50), which is within the submergence conditions of Ma et al. [2013]. The velocity of the return flow due to the large spatial variability of the site properties could modify the model's dissipation rate. Investigating this mechanism with a similar spatial arrangement than the field measurements could determine its relevance for SWAN modeling. Nevertheless, the intensity of this velocity is not expected to be strong as large water depth and channels facilitate the return flow.

Drag and friction coefficients used during the models validation and comparison were larger than those reported for flexible vegetation under steady flow [Wamsley et al., 2010]. Nevertheless, the behavior of flexible vegetation to orbital velocities largely differs from the one with steady flow as the stems bend with the flow but behave as rigid elements for small orbital amplitudes. In addition, the large variability of vegetation properties on similar sites has shown that the rough determination of the stem parameters might be compensated during the calibration. It is recommended to obtain further information on the spatial variation of vegetation properties and investigate its effect on the spectral evolution.

The model of Jacobsen et al. [2019] has shown the best performance in the experimental and field validation by capturing the physics behind canopies dissipation in different submergences. The effect of flexibility in the in-canopy velocity and dissipation reduction is crucial to replicate measurements (e.g., Lowe et al., 2005, Hu et al., 2014). Therefore, the spectral effect of flexibility and velocity reduction is combined in the α_v factor, which replaces α_u. A frequency-dependent formulation has been included by modifying Jacobsen et al. [2019] model. The validation confirmed that a frequency-dependent reduction factor provides a good fit for the site's energy distribution. The form of this frequency-dependent reduction factor could not be further investigated in the present time-limited research. Spectral parameters have been obtained (e.g., Lowe et al. [2007], Luhar et al. [2010], Jadhav et al. [2013]) for rigid and flexible canopies measurements. Comparing these to a larger set of conditions could result in a robust empirical or analytical formulation without the need for velocity measurements, making it a crucial mechanism to include in large scale modeling over vegetation with spectral wave models like SWAN.

6

Conclusion

In this last chapter of the report, the research output is related to the problem that motivated this project. The last section of Chapters 3, 4, and 5 include a broader discussion on the findings and its implications. The key points of the analysis are presented in section 6.1, where the answers to the research sub-questions are provided. Next, recommendations from the present study's insights are included in 6.2 to provide direction for further research.

6.1. Conclusion

The interaction of vegetation with waves is a relevant social, environmental, and scientific topic. Natural-based solutions using vegetation can protect shorelines from erosion and flooding while providing additional benefits such as carbon storage and biodiversity enhancement. Wave attenuation by vegetation is included in spectral models like SWAN. In this model for coastal areas, vegetation can be represented as increased bottom friction (implicit modeling) or the drag force from canopies (explicit modeling). A recent field campaign measured the wave transformation over salt marshes during winter storms, which showed not yet understood differences against models' results. A research question has been formulated to explore for a solution to this problem:

> *"What are the possible missing mechanisms in the dissipation function that could reduce the wave spectral mismatch between SWAN model outputs and (lab and field) measurements over vegetation?"*

The missing mechanisms in the dissipation function have been investigated by implementing a new frequency-dependent explicit model [Jacobsen et al., 2019] in SWAN, and comparing it to implicit (Collins [1972] and Madsen et al., 1988) and explicit (Suzuki et al., 2011) models by using lab and field measurements. The answer to the main research question has been elaborated following the two research sub-questions, as defined in Chapter 1.

The implementation of the new model in SWAN has been evaluated by comparing it to the explicit model from Suzuki et al. [2011]. The regular and irregular waves computational experiments confirmed the correct implementation of the model in SWAN's source code. Besides, differences between the documented ($\widetilde{\sigma}_{m,-10}$) and implemented ($\widetilde{\sigma}_{m,01}$) mean frequency of Suzuki et al. [2011] were found, which change the comparison between models reported in Jacobsen et al. [2019].

1) *"What are the spectral differences between the dissipation functions for vegetation in SWAN?"*

1.a) "What are the performance differences between the explicit and implicit modeling approach if compared to the energy distribution of measurements?"

1.b) "If implemented in SWAN, could the new model [Jacobsen et al., 2019] be an improvement for spectral wave modeling over vegetation?"

The implicit model of Madsen et al. [1988] showed not to be able to reproduce the amount of bulk dissipation for $h_v/d > 0.25$ in the present report. The iterative solution of this model with Jonsson [1966] in SWAN limits the friction factor to 0.3 if $A_b/k_N < 1.57$. The implicit model of Collins [1972] did dissipate the required total amount except for one case of the lab experiments with $h_v/d = 1.17$ and $k_p d = 1.38$, which is largely outside the range of conditions the model was made for (e.g., bottom friction). As a bottom friction model, the model assigns dissipation from low to higher frequencies, matching the measurements for smaller values of h_v/d. This causes the mean period of the implicit model to decrease for all tested cases. If significant dissipation is required, all energy bellow mid-range frequencies vanish, locating the remaining energy at higher frequencies than the measurements. This results in poor bulk and spectral performances of Collins [1972] implicit model for $h_v/d \geq 0.76$. Implicit modeling misses the physical representation of vegetation by only using a friction factor. The large variability of the factors in the calibration shows the chances of model over-tuning with $h_v/d \leq 0.65$ but not for $h_v/d = 0.25$.

Explicit modeling defines the vegetation height, diameter, density, and drag coefficient in the formulation, including better representation of reality. The regime (shallow, intermediate, or deep water), characterized by $k_p d$, will largely indicate each wave component's velocity profile. For the same water depth, high frequencies (low $k_p d$) will experience less dissipation than low frequencies (high $k_p d$). For emergent vegetation, the little energy in short components is also reduced, resulting in a decrease of the mean period as more energy remains in the rest of the spectra. The explicit model of Suzuki et al. [2011] uses $\widetilde{\sigma}_{m01}$ to represent dissipation. This equally distributed approach will over dissipate high frequencies and under dissipate low frequencies for submerged vegetation, but will have only small differences for emergent vegetation.

The newly implemented model reproduced the sign and the magnitude of the mean period evolution accurately, to higher or smaller values depending on the submergence level. The mechanism responsible for the good match is the frequency distributed velocity spectrum and, therefore, dissipation. The orbital velocities of each component are properly modeled in the water column, where they interact with the drag force of canopies that are partially or fully present in the water column (changing the spectral evolution). From this analysis, it is concluded that the newly implemented explicit model of Jacobsen et al. [2019] is an improvement for spectral wave modeling over canopies, by capturing the physics behind the drag dissipation mechanism in all submergences. Good performance with implicit models was only observed for $h_v/d \leq 0.5$, and with the explicit model of Suzuki et al. [2011] for $h_v/d \geq 1.0$.

During the field validation, the newly implemented model, together with Collins [1972], reproduced the amount of dissipation for the wind sea region (0.2-0.5 Hz), which was not achieved by the other models. Madsen et al. [1988] did no match the total dissipation, and Suzuki et al. [2011] did not capture the physics for dissipation with submerged vegetation. No model reproduced the reduced dissipation in low frequencies ($f < 0.2$ Hz). This is caused by additional processes in the field measurements, as discussed in the next subquestion.

2) "If the new model's possible improvements in the dissipation function are not the answer to the wave modeling over vegetation spectral mismatch, which other processes could be responsible, and what are the recommendations for further research?"

Previous studies (e.g., Lowe et al., 2007, Bradley and Houser, 2009, Manca et al., 2012, Beudin et al., 2017, Nowacki et al., 2017) have documented a reduced dissipation for longer components in wave dissipation over vegetation. This has been explained by the change of geometry of the plant due to flexibility and forcing conditions, altering drag and inertial forces. Flexible blades have been reported to be out of phase to the peak frequency while in-phase for low frequencies, causing the stems to bend with long waves but behave as rigid elements for shorter components [Bradley and Houser, 2009]. The in-canopy velocity reduction will then be highly related to this process, as the position of the canopy will change.

This mechanism has been investigated by implementing a frequency-dependent reduction factor in a modified version of the Jacobsen et al. [2019] model. The spectral reduction factor depends on the wavenumber, which will assign a more substantial reduction for longer components. The validation with field measurements has shown that the flexibility spectral reduction factor model can reproduce the distributed energy decay of the measurements, reducing the spectral mismatch between measurements and models. The results confirm that a spectral reduction factor could simulate the reduced dissipation in field measurements over submerged and highly flexible vegetation. The formal representation of the flexibility reduction factor has not been investigated in this time-bounded research. Performing further research on the phase relationship between flexibility and wave components (and its effect on the in-canopy velocity reduction) is necessary to develop a robust and practical model.

Despite the good match of the distributed energy decay with the modified Jacobsen et al. [2019] model, a significant mismatch is already present before the vegetated foreshore. The possible processes involved in this difference have been investigated by looking at the water levels, generation mechanisms, model's settings, and the spectral transformation over the transect. The presence of more and widely distributed energy at frequencies below 0.2 Hz likely indicates that more than one mechanism is involved. The conditions with shallow conditions and steep waves in the Wadden Sea confirm that non-linear interactions can cause low-frequency energy (e.g., Infra-Gravity waves). Besides, horizontal variations in the vegetated foreshores could generate near-shore currents that will interact with the incoming waves. The site conditions have the same submergence as previous studies [Ma et al., 2013]. If present, near-shore currents could cause additional mechanisms that add to the spectral mismatch. The recommendations to perform studies over these mechanisms are included in the next section.

6.2. Recommendations

The model SWAN has numerous capabilities, which have made it a worldwide used wave model. Nevertheless, there is still room for improvement as near-shore currents, and infra-gravity waves generation are not included. Near-shore currents can be given as input from a flow model, but wave generated rip currents, or near-shore processes do not occur within the wave model. Besides, non-linear redistribution of energy has been included in SWAN with the DIA and LTA approximations that simplify the immense number of interactions between frequencies. Extension of triads to generate low-frequency waves by the interactions of the concerning components will reduce the mismatch in low-frequencies.

The model from the *POV Waddenzeedijken* project has shown that exploring specific settings could give some hints in further research. The quadruplet interactions could be computed per iteration instead of per sweep, as recommended in the SWAN user manual [The SWAN team, 2019b]. Also, the first spectral grid in the spectral modeling of SWAN should be empty, while in the measurements, a significant amount of energy is present at 0.03 Hz. Defining a lower limit for the spectral range could be explored if the mismatch at these frequencies is intended to be reduced.

The water surface elevation from the field measurements has shown a considerable increase in energy when tending to zero. This has been related to spectral leakage that can either be created by data processing or measurements. Investigating this carefully and understanding its magnitude could contribute to understanding the phenomena at low frequencies. Time bursts of the measured water levels have been shared, showing the complexity of the field conditions. This would require an in-depth analysis of the obtained pressure information (e.g., bispectral analysis) to study the low-frequency components.

The spectral model SWAN is based on the action balance and uses the relative frequency σ to compute the source terms. To implement the model of Jacobsen et al. [2019] in SWAN, the documented absolute frequency ω has been exchanged for σ. The experimental validation did not include currents, and the velocity of ambient current at the field measurements was very low, expecting non-significant differences. Nevertheless, an ambient current is often present in vegetated systems (e.g., estuaries). The possible effects of this choice could not be found in the literature, and they were not investigated in the present research. Therefore, it is recommended to perform validation of the models with wave-current interaction in a wave flume to understand its effects on the spectral dissipation shape.

The flume experiments have shown that the model is a significant improvement for wave modeling over canopies. It is recommended to perform further studies and validate the new model under different conditions (e.g., sloping bed, flexibility, interaction with other dissipation mechanisms, longer and higher waves). The experimental validation noted that almost no energy is present in low frequencies. During the field validation, this range of frequencies and its effect with flexible vegetation is a main point of discussion in the present research and should be considered in the next experimental validation of the model.

The drag coefficients have proven to not be exchangeable between models. In addition, these depend on the vegetation properties, flow conditions, and length of the canopies field. The ratio between models' drag coefficients (Suzuki et al., 2011 over Jacobsen et al., 2019) was above and under the unity with a threshold ~ 2.5 of the modified Keulegan Carpenter number (Q). A vast number of drag coefficients have been obtained in previous studies (e.g., Asano et al., 1988, Quartel et al., 2007, Cavallaro et al., 2010, Maza et al., 2013, Houser et al., 2014, van Rooijen et al., 2018). Investigating the relation between obtained coefficients could determine a conversion formulation between models' coefficients. This would provide the new SWAN dissipation explicit model with a larger set of values for further applications.

The modified version of Jacobsen et al. [2019] model has shown to match the distributed energy decay of the field measurements. This shows significant improvements for spectral wave modeling over vegetation. Nevertheless, the exact form of the spectral reduction factor a_v has not been investigated in this time bounded thesis. The stem change of geometry caused by flexibility will modify inertial forces related to the in-canopy velocity. It will be crucial to understand the flexibility and in-canopy velocity reduction independently to isolate them in a formulation eventually. Nevertheless, the high complexity of these two interrelated processes could delay developments for practical applications. Previous studies have concluded that the in-canopy reduction factor was relatively frequency-independent, meaning that the drag coefficient calibration could include its effect on rigid canopies. Therefore, it is recommended to investigate the full effect of flexibility on the spectral wave dissipation as one reduction factor to develop further improvements for large-scale applications.

A
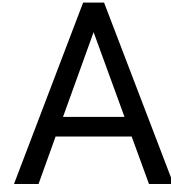
User guide SWAN new model

Here the command to activate the explicit modeling wave damping by vegetation is explained. The vegetation source term was extended with an additional option to choose between the current implementation by Suzuki et al. [2011] and the new subroutine. This user guide applies to versions:

- Jacobsen et al. [2019] original model (equation 3.2)

- Jacobsen et al. [2019] modified model

        i) Constant reduction factor (equation 5.5)

        ii) Spectral reduction factor (equations 5.10 and 5.11)

The dissipation source term can be activated as following:

```
                | -> SUZuki < [height] [diamtr] [nstems] [drag] >
                |
VEGEtation <
                |
                |
                | JACObsen < [height] [diamtr] [nstems] [drag] >
```

The vegetation variables in this command are:

Input	Symbol	Description	Units
height	$h_v = \alpha h$	Vegetation height	m
diameter	b_v	Stem thickness	m
nstems	N_v	Vegetation density	stems / m^2
drag	CD	Drag coefficient *	-

* Drag coefficients are not exchangeable between dissipation models.

No changes have been made to vary the vegetation density horizontally. For this, a grid must be created and loaded in the input file using INPGRID NPLANTS and READINP NPLANTS. For more information, please consult SWAN version 41.31 user manual. Different vegetation properties in the vertical are included in Suzuki et al. [2011] model but not on the new models used for the present project.

B

Numerical Sensitivity Analysis New Implementation

B.1. Integration Points

The required numerical integration on the vertical has been solved with the Simpson rule. The number (odd) of integration points defines the accuracy of the approximation. Jacobsen et al. [2019] investigated the required number of points to achieve an error $\varepsilon_M < 0.001$ by comparing the model outputs with a different number of points against a target with M = 1501 points. The error is defined as:

$$\varepsilon_M = \frac{[d_v]_{z,M}}{[d_v]_{z,1501}} \tag{B.1}$$

The results from this investigation are shown in Figure B.1, where 15 and 21 integration points were sufficient to keep the approximation error below 0.1 % for most of the applications.
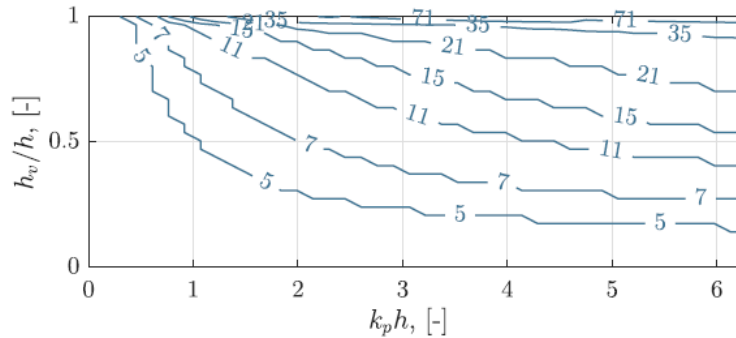
Figure B.1: Required number of Integration Points in Simpson's integration rule for dissipation model of Jacobsen et al. [2019] to keep $\varepsilon_m < 0.001$. (From Jacobsen et al., 2019)

In the new SWAN implementation, the approximation error is investigated by comparing model versions with 5, 11, 21, 31, 51, 71, and 101 integration points. The analysis uses the reference case described in Table 3.1 with h_v/d = 0.50. Computations stopped and communicated a stack overflow with a large number of integration points ($\geq$ 31). Therefore, these results are not included in the present analysis. To study the effect on the total dissipation, $\epsilon_{Bulk,M}$ has been defined by dividing the bulk dissipation from the incoming JONSWAP spectra (first cell) with each M number of points over 21 points:

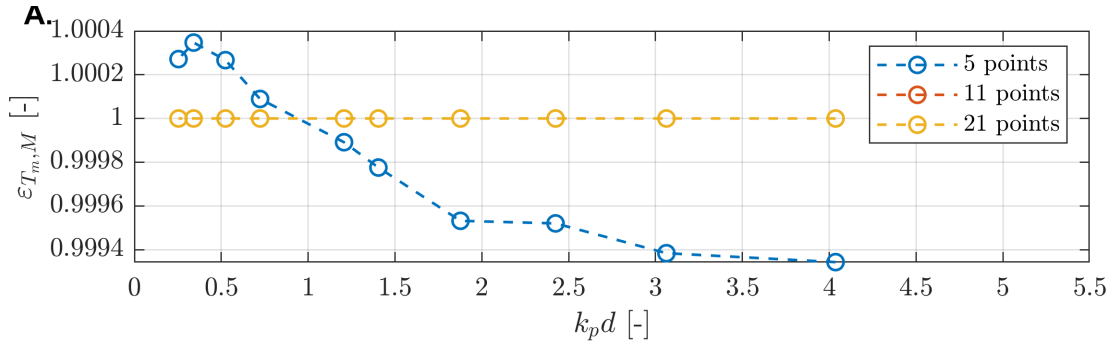$$\epsilon_{Bulk,M} = \frac{[D_{veg,tot}]_{z,M}}{[D_{veg,tot}]_{z,21}} \tag{B.2}$$
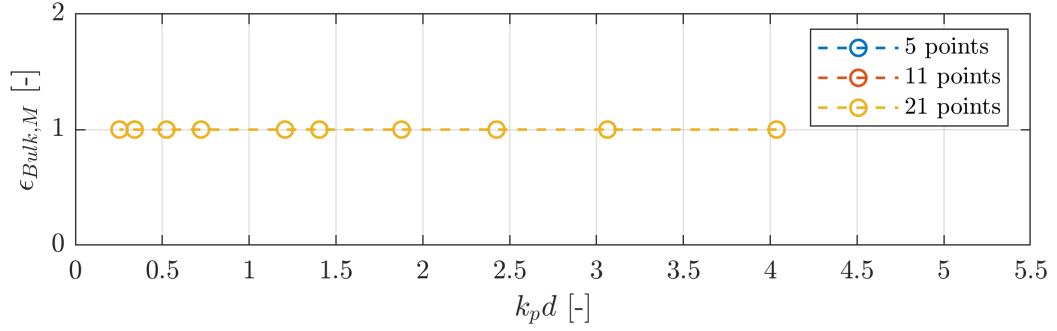
Figure B.2: Investigation over number of integration points over the vertical with Simpson's integration rule for irregular waves. Deviation is defined as the bulk dissipation ratio with M number points over the bulk dissipation with 21 number of points with $\gamma = 3.3$ and $h_v/d = 0.50$.

Figure B.2 shows no visible differences between the bulk dissipation of the models. To analyze the effect of the integration points choice on the spectral evolution, the mean period's ratio at the end of the domain (x = 500 m) is analyzed using 21 points as the reference case.

$$\varepsilon_{T_m,M} = \frac{[T_{m01,500m}]_{z,M}}{[T_{m01,500m}]_{z,21}} \tag{B.3}$$

Figure B.3: Investigation over number of integration points over the vertical with Simpson's integration rule for irregular waves with the ratio of the mean period evolution at the end of the spatial domain (500 m) with M points over 21 points with $\gamma = 3.3$ and $h_v/d = 0.50$.

Differences were only found for a relative submergence of $h_v/d = 0.5$ with 5 integration points. Nevertheless, these differences are still smaller than 0.1 %. These results corroborates the analysis in Figure B.1 where 11 points were sufficient for $k_p d$ values < 4.5 as tested here.

Defining the integral with 31 or more integration points overstacked the computations in SWAN. Therefore, these are not recommended. The upper limit with 21 points showed to be a stable decision that keeps the error to a negligible minimum, as observed in Figure B.1. Therefore, this is selected for the version in the present report.

B.2. Threshold of kd on orbital velocities regime

As described in Chapter 3, the numerical limitation with hyperbolic functions in Fortran has been solved by computing the orbital velocities with the general form under a threshold of kd and with the deep regime form above it. The choice on this threshold is investigated by testing values of 5, 20, and 30. The orbital velocities in the code would read:

$$\hat{u}_x = \omega a \frac{\cosh[k(d+z)]}{\sinh(kd)} \qquad\qquad kd \leq 5 \text{ , 20 or 30} \quad \text{(B.4)}$$

$$\hat{u}_x = \omega a e^{kz} \qquad\qquad kd > 5, \text{ 20 or 30} \quad \text{(B.5)}$$

The bulk dissipation ratio and the statistical indicators of the mean period evolution are used for this purpose. There reference case from Table 3.1 with $h_v/d = 0.50$ is studied, with results shared in Figures B.4 and perfkd.
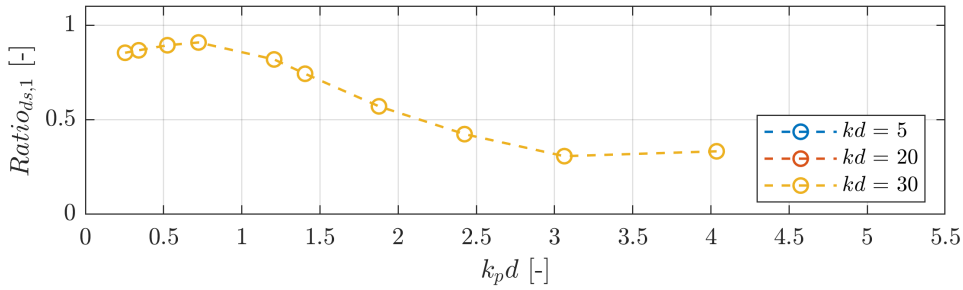
Figure B.4: Investigation kd threshold for orbital velocities computation for irregular waves bulk dissipation ratio of Suzuki et al. [2011] over the new implementation with different values of periods and water depths with $\gamma = 3.3$ and $h_v/d = 0.50$.
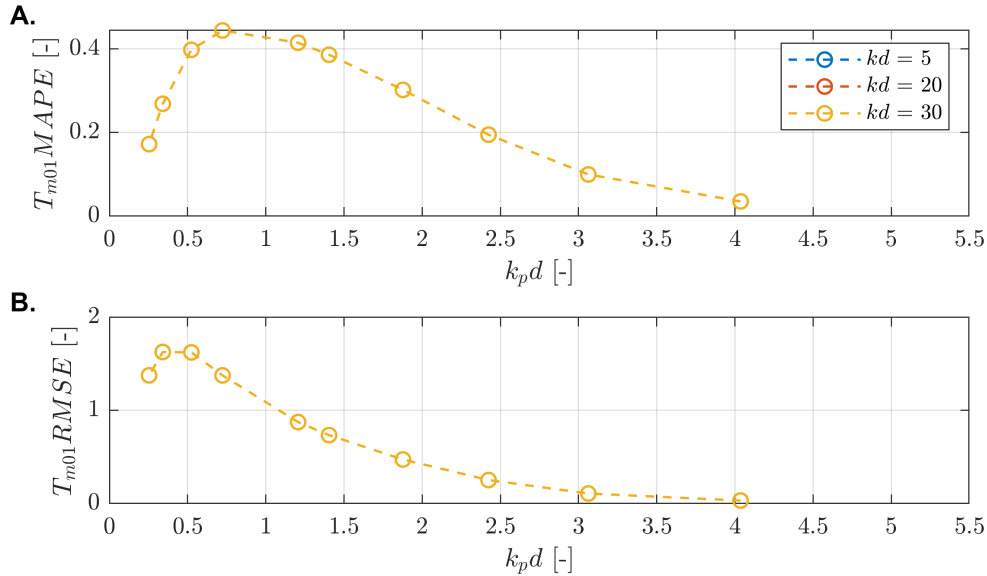
Figure B.5: Investigation over kd threshold for orbital velocities computation for irregular waves statistical indicators (**A.**) *MAPE* and (**B.**) *RMSE* for the mean period evolution through the spatial domain using different values of wave heights and water depths with $\gamma = 3.3$ and $h_v/d = 0.50$.

The results show no differences between any of the tested values. Other subroutines in SWAN use the threshold $kd = 30$ to limit the hyperbolic calculations. The present version defined $kd = 20$ to be sure it would not present numerical limitations. Nevertheless, a smaller value could be implemented without further impact on the results.

B.3. Resolution

Usual scales for modeling waves approaching the coastline would require a few kilometers, depending on the slope, with a resolution of 50 to 100 m. Typical values of the spectral resolution in SWAN are $df/f = 0.1$. These have been used as starting points on the computational experiments of Chapter 3. Nevertheless, the rate of energy change in space and frequencies required a finer resolution to compare the results visually. The discretization based on typical values is compared to the resolution used in Chapter 3. The effect of the spatial resolution is displayed by comparing Figures B.8 and B.6, and the effects of modifying the spectral resolution by comparing Figures B.7 and B.9.
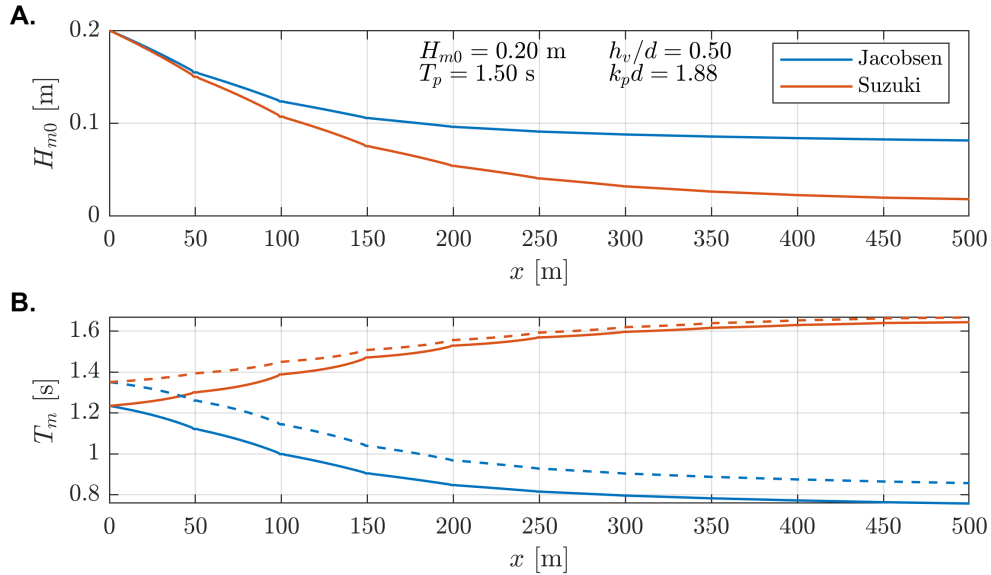
Figure B.6: **A.** Wave height and **B.** Mean period (T_{m01} continuous line and T_{m-10} dashed line) evolution through the spatial domain from model comparison with irregular waves and boundary conditions $\gamma = 3.3$, $T_p = 1.5$ s, $H_{m0} = 0.1$ m, and $h_v/d = 0.50$. Spatial resolution = 50 m per grid. Spectral resolution $df/f = 0.0106$.
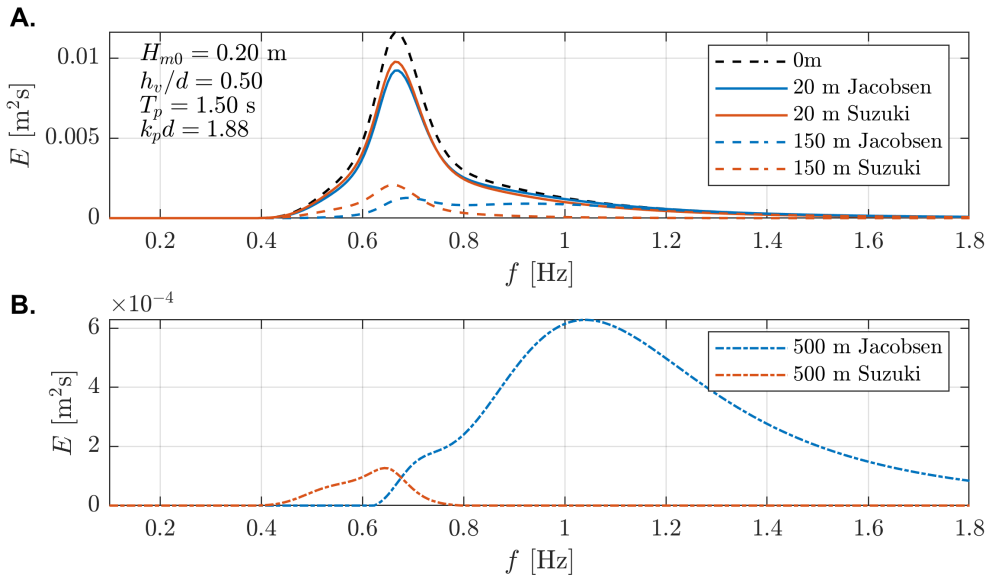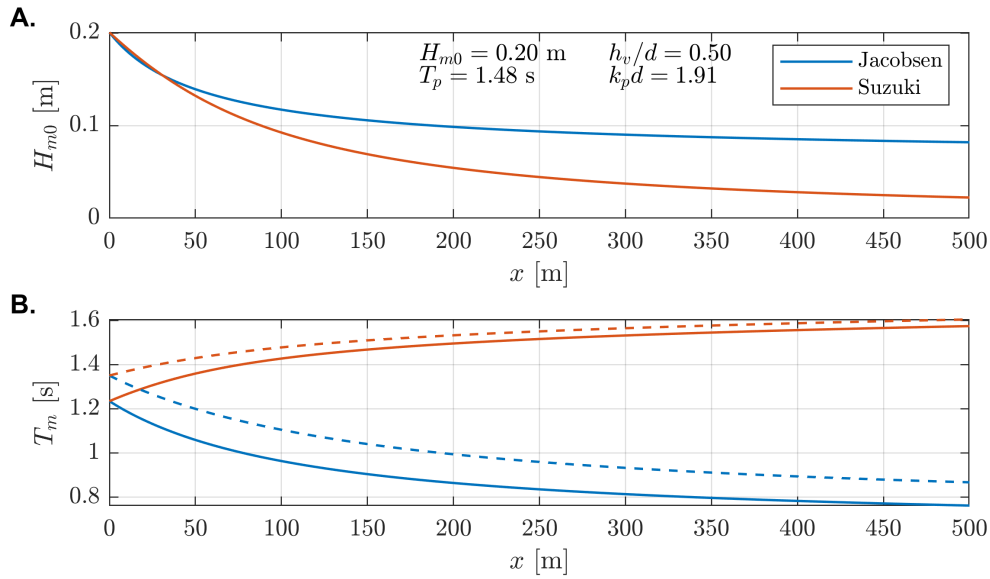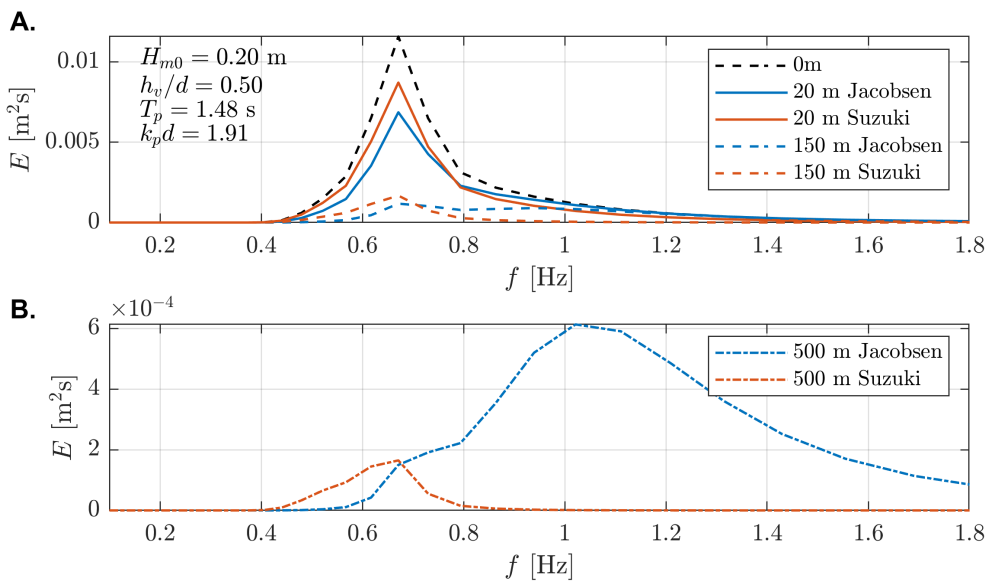

Figure B.7: Spectral comparison at the end of the spatial domain with irregular waves and boundary conditions $\gamma = 3.3$, $T_p = 1.5$ s, H_{m0} = 0.1 m, and $h_v/d = 0.50$. Spatial resolution = 50 m per grid. Spectral resolution $df/f = 0.0106$.

A.

B.

Figure B.8: **A.** Wave height and **B.** Mean period (T_{m01} continuous line and T_{m-10} dashed line) evolution through the spatial domain from model comparison with irregular waves and boundary conditions $\gamma = 3.3$, $T_p = 1.5$ s, $H_{m0} = 0.1$ m, and $h_v/d = 0.50$. Spatial resolution = 1 m per grid. Spectral resolution $df/f = 0.0876$.

A.

B.

Figure B.9: Spectral comparison at the end of the spatial domain with irregular waves and boundary conditions $\gamma = 3.3$, $T_p = 1.5$ s, H_{m0} = 0.1 m, and $h_v/d = 0.50$. Spatial resolution = 1 m per grid. Spectral resolution $df/f = 0.0876$.

As observed in the previous figures, the conditions of the cases from Chapter 3 required a high resolution to analyze the differences in the bulk energy decay and the distribution of energy in frequencies. Even though the spatial resolution could be defined in a point between 1 and 50 m, The SWAN team [2019a] recommends energy should not shift more than one spectral bin when propagating over one spatial grid. Therefore, a balance must be found between spatial and spectral resolution. This lead to the explained discretization in Chapter 3.

C

Boundary Conditions Experimental Validation

The target JONSWAP spectra from the experimental validation in Chapter 4 showed differences than the measured energy before the canopies. An example of the differences between these two are shared in Figures C.1 and C.2. The shape of the incoming spectra determined whether the models could capture the spectral shape evolution in more detail. Even though the qualitative comparison from Figures C.1 already shows the model differences, using the measured spectra as boundary condition confirms these remain. The evolution of small peaks is also observed in Figure C.2. The improvements in using the real measured spectra are also significant by looking at the different values between target and measured characteristics like H_{m0} and T_p in Table 4.2.
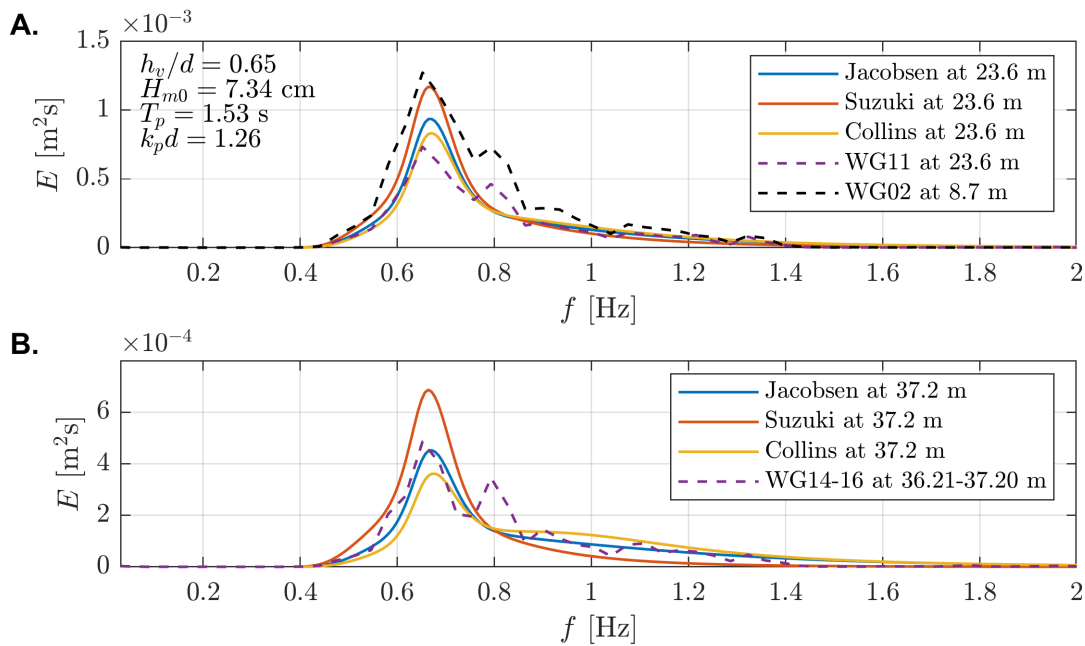
Figure C.1: Variance density spectrum for the measurements and models for IR06 with target boundary conditions T_p = 1.53 s, H_{m0} = 7.34 cm, and h_v/d = 0.65 defined with a JONSWAP spectra. **A.** WG02 compared to WG11 at 23.57 m. **B.** Comparison of mean spectra of measurements after canopies (WG14-16) and experiments.
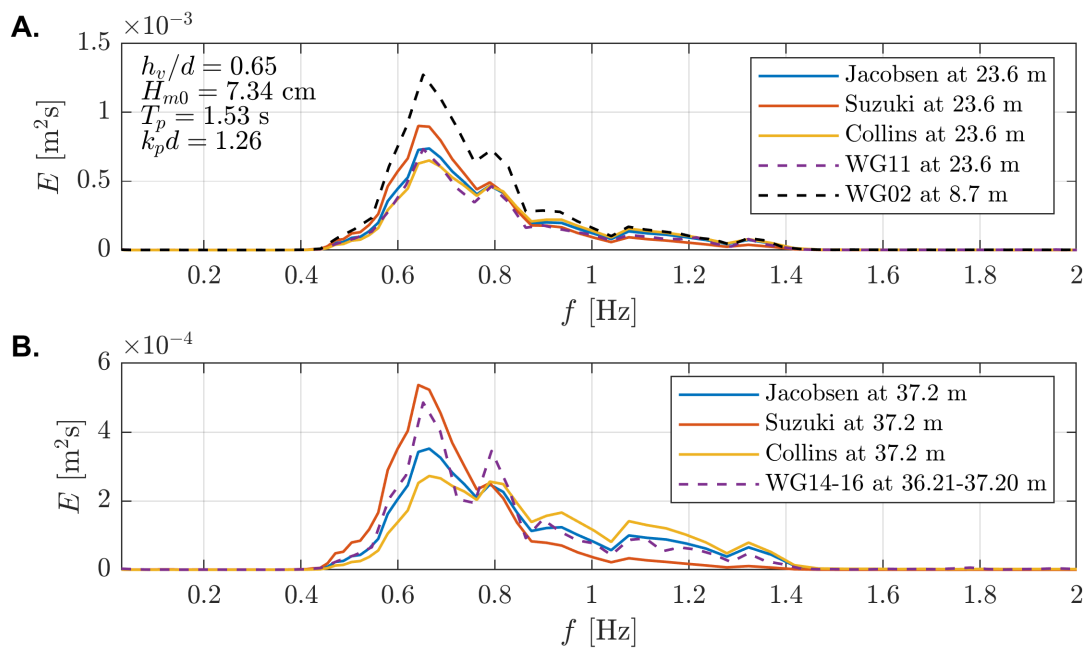
Figure C.2: Variance density spectrum for the measurements and models for IR13 with boundary conditions (by measurements input) T_p = 1.53 s, H_{m0} = 7.34 cm, and h_v/d = 0.65. **A.** Boundary condition (WG02) compared to WG11 at 23.57 m. **B.** Comparison of mean spectra of measurements after canopies (WG14-16) and experiments.

D

Hindcast Groningen

The wind, water levels, currents, and wave conditions were provided as Input in the SWAN grid by weather hindcast predictions. Appendix D displays some values of these conditions as reported in Steetzel et al. [2018]. The hindcast results of wave heights defined the peak of each storm (the moment with the highest H_{m0}), as shared below:

Volgnummer	Hindcast moment	Opmerking
01	2015-01-10 15:00	
02	2015-01-10 23:00	
03	2015-01-11 01:00	Hoogste H_{mo} 2015-storm
04	2015-01-11 03:00	
05	2017-01-13 10:00	
06	2017-01-13 21:00	
07	2017-01-13 22:00	Hoogste H_{mo} 2017-storm
08	2017-01-13 23:00	
09	2017-01-14 10:00	

Figure D.1: Highest significant wave height time burst from the hindcast prediction for the determination of the storms' peak. (From Steetzel et al. [2018])

The water levels and significant wave heights showed a clear correlation, pointing the importance of the water depth in limiting the wave heights by depth breaking in the site of study. Figures D.2 and D.3 show the evolution of the significant wave height overtime during the storm of 2015 and 2017, respectively.
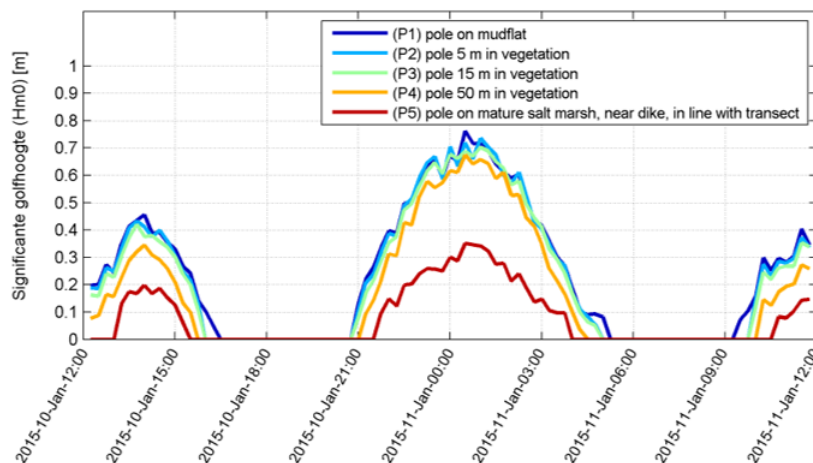

Figure D.2: Modeled significant wave height over time at the research transect on the 10th and 11th of January 2015.(From Steetzel et al. [2018])
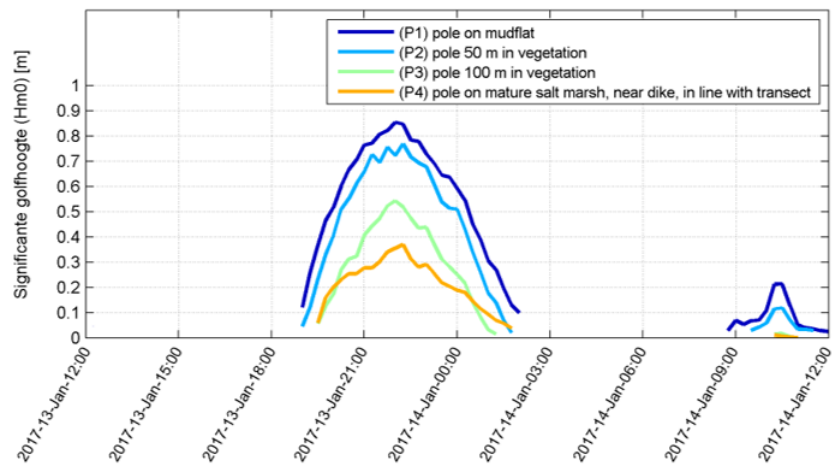
Figure D.3: Modeled significant wave height over time at the research transect on the 13th and 14th of January 2017 at 22:00 h. (From Steetzel et al. [2018])

Nevertheless, if the surface elevation time series at the end of Chapter 5 are observed (Figures 5.27 and 5.28), the wave heights at 23:00 h are higher than the defined peak moment (22:00 h). This is caused by differences between the hindcast results and measurements, as shown in Figure D.4.
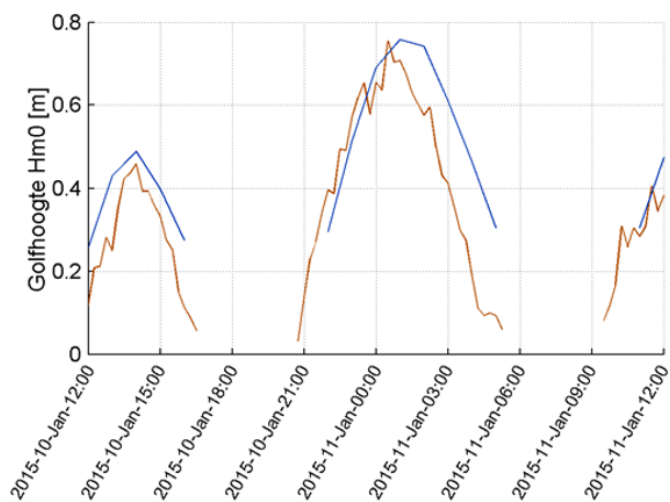

Figure D.4: Significant wave height between measurements and hindcast predictions at the research site on the on the 11th of January 2015. (From Steetzel et al. [2018])

Ambient current is a topic of discussion in the present report, the velocity values from a Delft3D flow model and in the SWAN grid are shared in Figures D.5 and D.6. These show that the SWAN domain values are close to zero and, therefore, not a significant consideration for the vegetated foreshore.
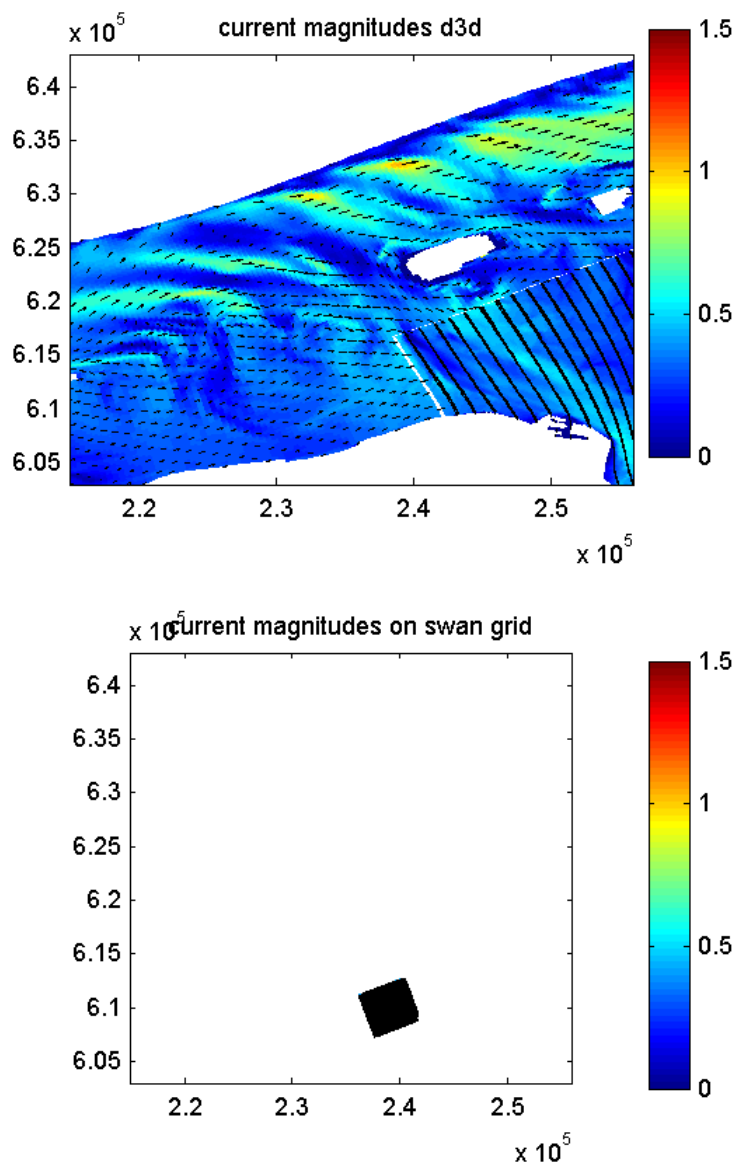
Figure D.5: Current magnitudes at the Wadden Sea from a flow module in Delft3D, and magnitues at the SWAN grid for the storm of the 11th of January 2015 at 01:00 h. (From Steetzel et al. [2018])
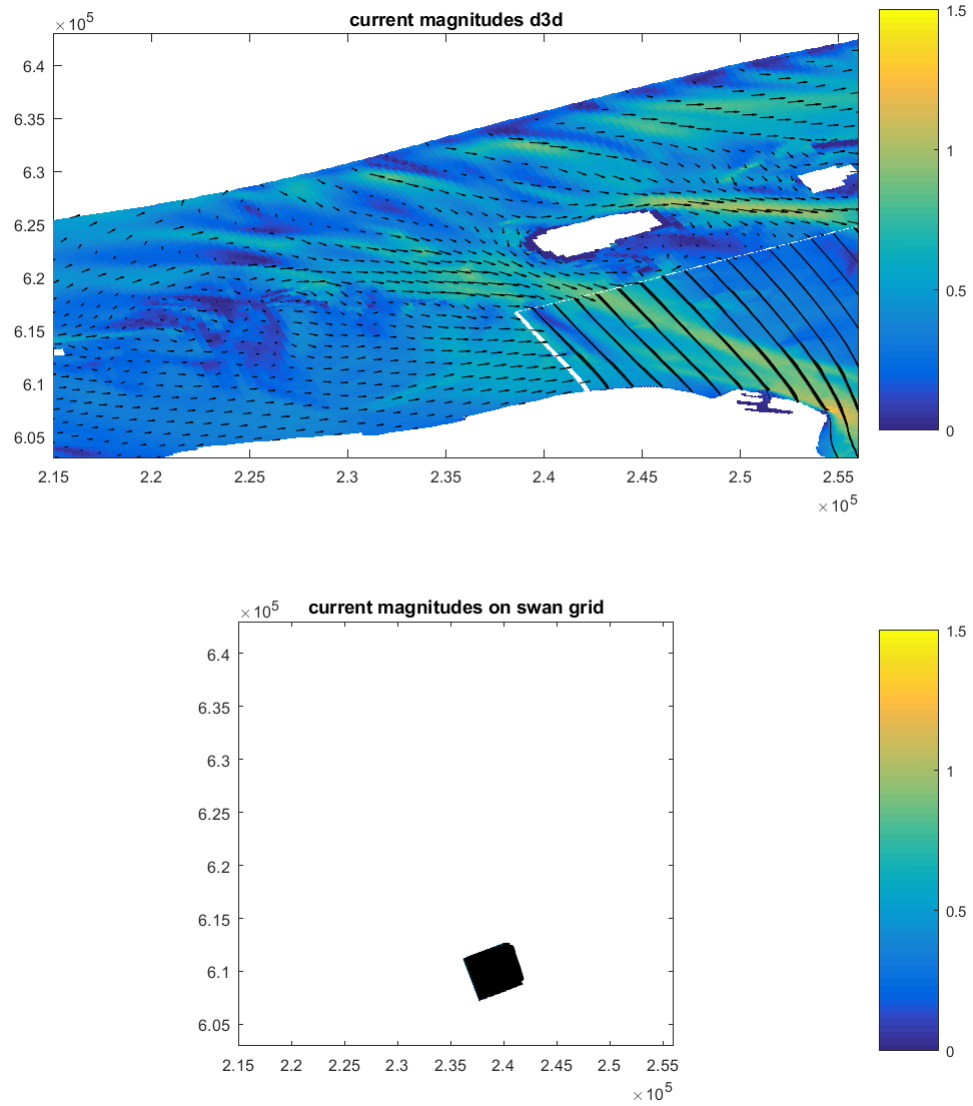
Figure D.6: Current magnitudes at the Wadden Sea from a flow module in Delft3D, and magnitues at the SWAN grid for the storm of the 13th of January 2017 at 22:00 h. (From Steetzel et al. [2018])

E

Frequency-Averaging Field Spectrum

The measured wave spectra were provided as input for the field validation in the report. The measured data resolution resulted in a 'grassy' distribution of energy in frequencies. For visual comparison only, the spectra were frequency averaged following the 5-point moving average. This approach averages the energy over five frequency bins and allocates it to the cell where calculations take place (i), giving the new value:

$$E_i(f_i) = \frac{E_{i-2}(f_{i-2}) + E_{i-1}(f_{i-1}) + E_i(f_i) + E_{i+1}(f_{i+1}) + E_{i+2}(f_{i+2})}{5} \tag{E.1}$$

An example of the visual differences before and after frequency-averaging is provided in Figures E.1 and E.2.
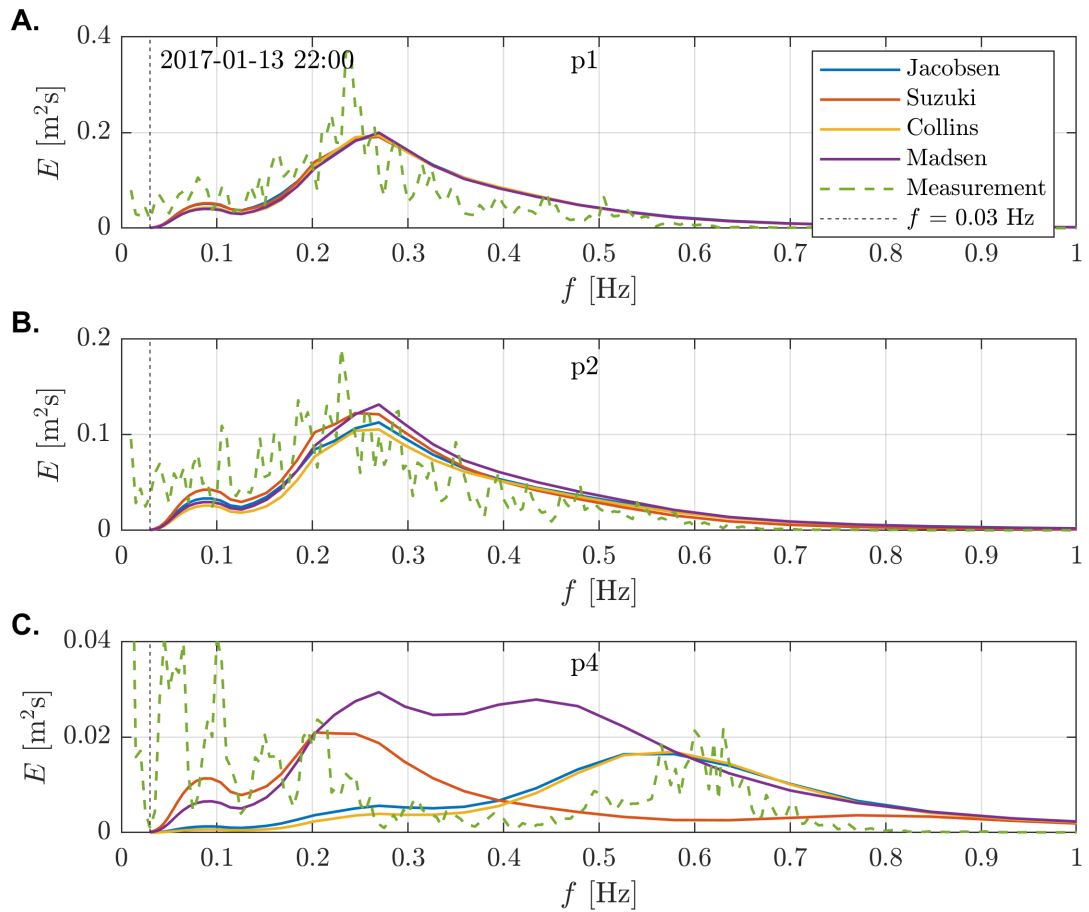
Figure E.1: Measured and processed spectra comparison between models and measurements for **A.** p1 (at marsh edge), **B.** p2 (50 m from marsh edge), and **C.** p4 (near dike, 300 m) for the storm of the 13th of January 2017 at 22:00 h.
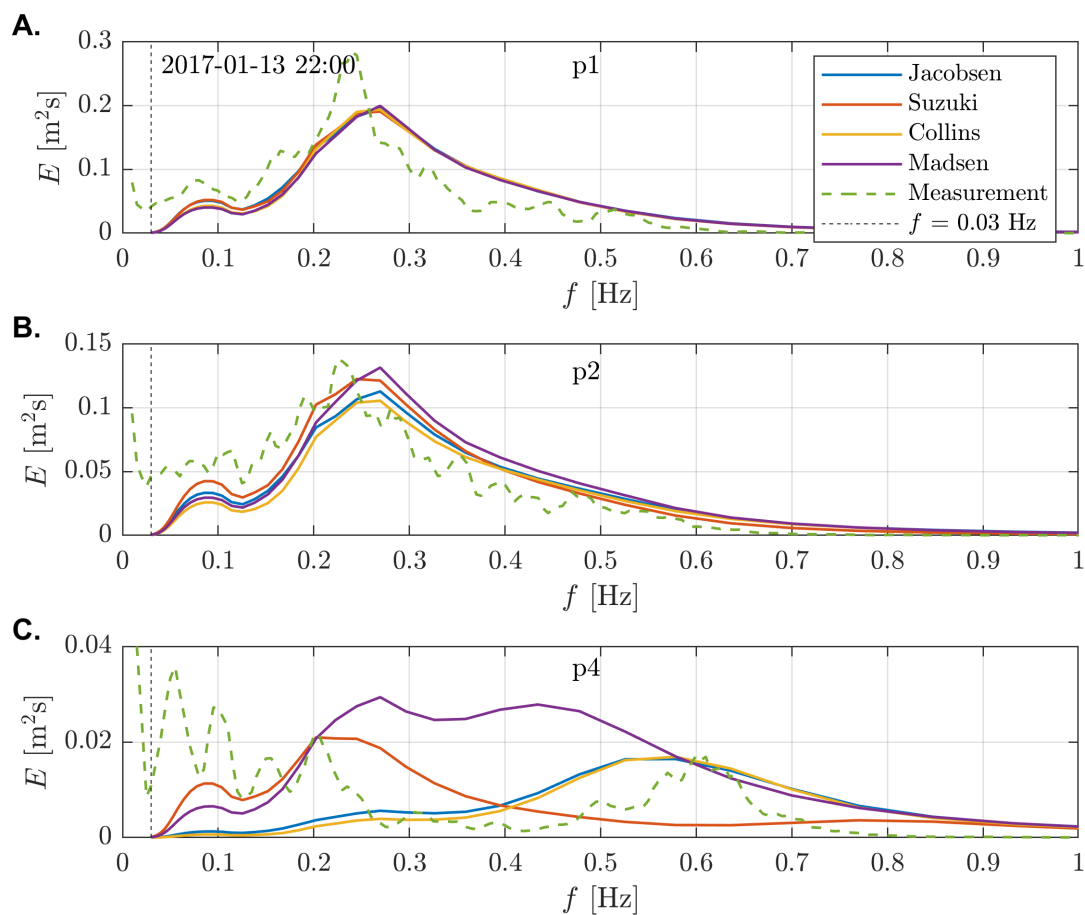
Figure E.2: Frequency averaged spectra comparison between models and measurements for **A.** p1 (at marsh edge), **B.** p2 (50 m from marsh edge), and **C.** p4 (near dike, 300 m) for the storm of the 13th of January 2017 at 22:00 h.

F

Sensitivity Wind Input Field Validation

Wind input has been deactivated from the SWAN models to understand the interaction between this mechanism and the models' spectral transformation at the transect of interest. The same calibration parameters used during Chapter 5 are kept for the present simulations.
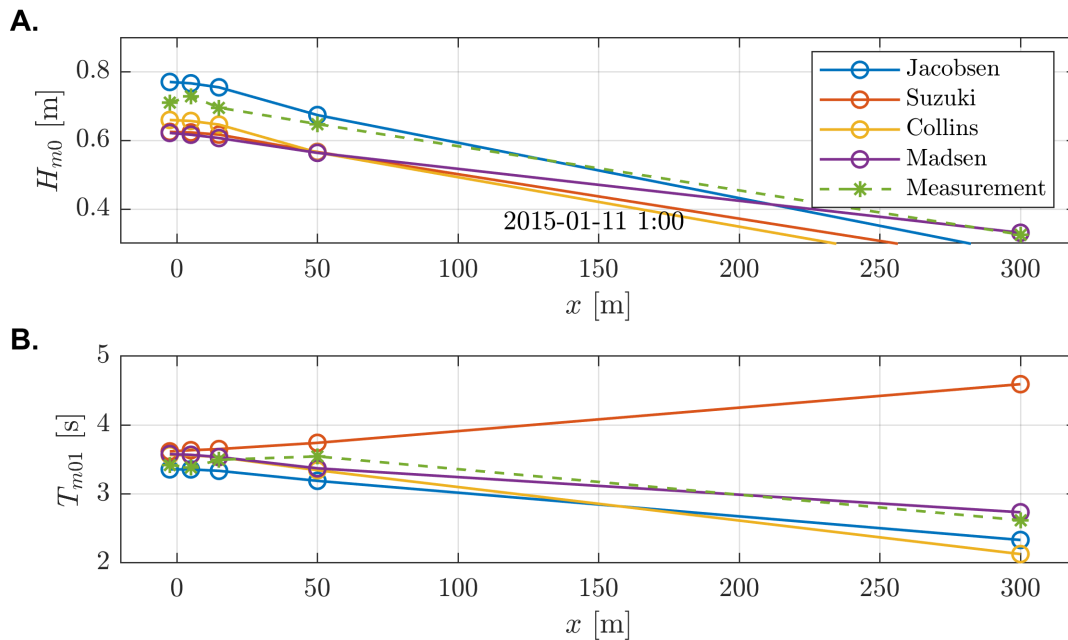
A.

B.

Figure F.1: (Computation without wind input). **A.** Significant wave height and **B.** Mean Period $T_{m,01}$ evolution between transect's stations p1-p5 at -2.5, 5, 15, 50, and 300 m for the storm of the 11th of January 2015 at 01:00 h.

Results show that Suzuki et al. [2011] goes in the wrong direction on the mean period evolution once there is no wind. This is caused by the mean wave parameters used in the formulation, which assign more dissipation to high frequencies than measurements. The results in Chapter 4 corroborate this behavior.
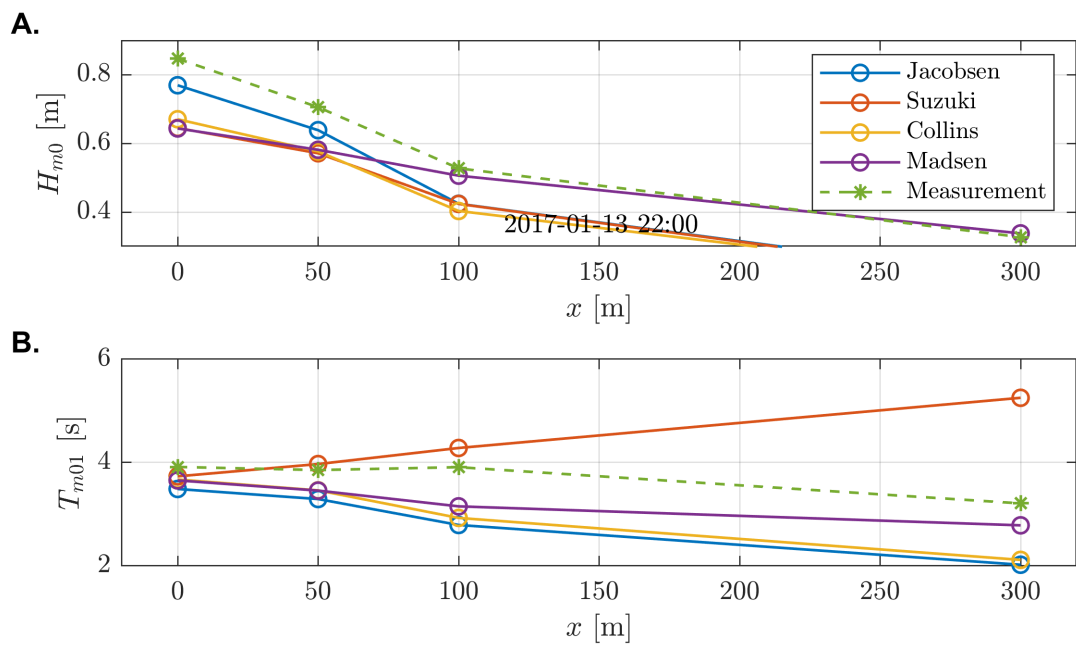
Figure F.2: (Computation without wind input). **A.** Significant wave height and **B.** Mean Period $T_{m,01}$ evolution between transect's stations p1-p4 at 0, 50, 100, and 300 m for the storm of the 13th of January 2017 at 22:00 h.

Figure F.3: (Computation without wind input). Spectrum comparison between models and measurements for **A.** p1 (2.5 m before marsh edge), **B.** p4 (50 m from marsh edge), and **C.** p5 (near dike, 300 m) for the storm of the 11th of January 2015 at 01:00 h.
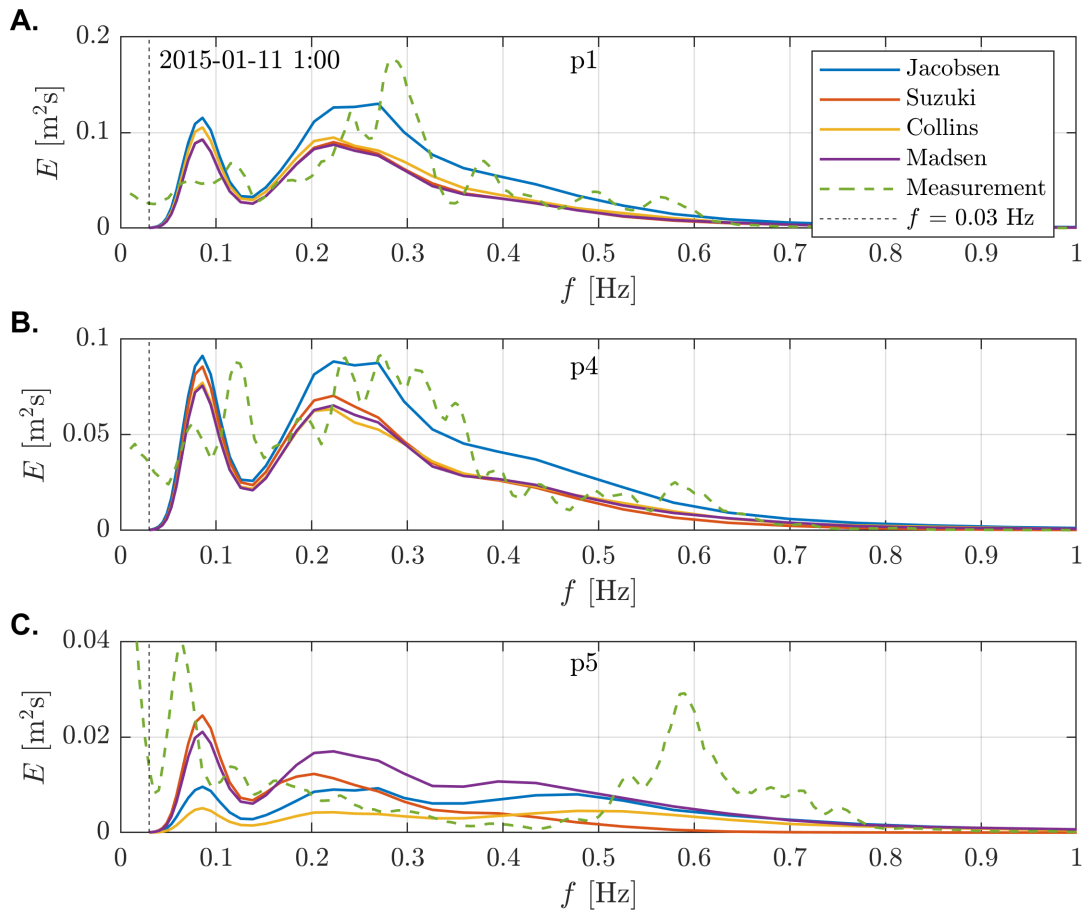
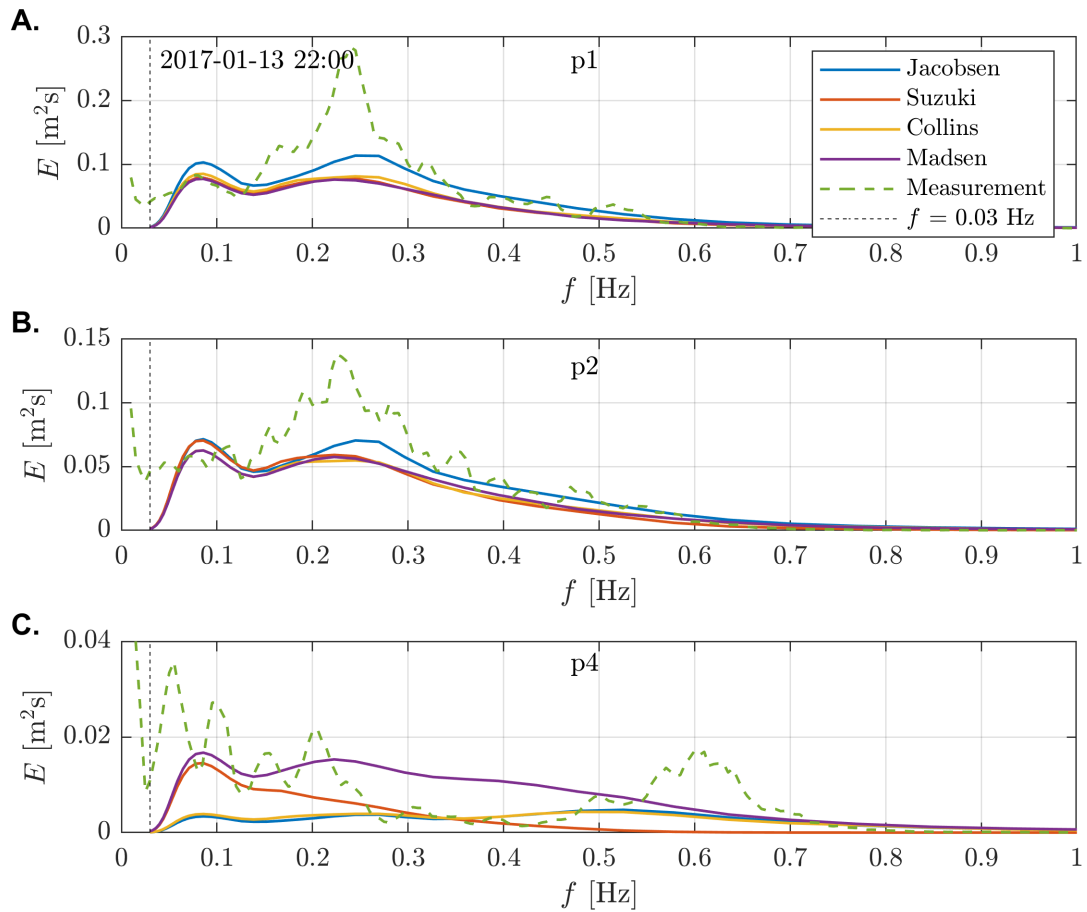Figure F.4: (Computation without wind input). Spectrum comparison between models and measurements for **A.** p1 (at marsh edge), **B.** p2 (50 m from marsh edge), and **C.** p4 (near dike, 300 m) for the storm of the 13th of January 2017 at 22:00 h.

Bibliography

M. E. Anderson and J. M. Smith. Wave attenuation by flexible, idealized salt marsh vegetation. *Coastal Engineering*, 83:82–92, 2014. ISSN 03783839. doi: 10.1016/j.coastaleng.2013.10.004. URL http://dx.doi.org/10.1016/j.coastaleng.2013.10.004.

Me Anderson, Jmk Smith, and Sk McKay. Wave dissipation by vegetation, CHETN-I-82. *US Army Corps of Engineers Engineer Research and Development Center: Vicksburg, MS.*, (September):22 pp, 2011. URL http://repository.tudelft.nl/view/hydro/uuid:17f2915f-bb57-47f9-8e85-67ff0c82510c/.

T.S. Asano, Tsutsui, and T. Sakai. Wave damping characteristics due to seaweed, (in Japanese),. *Thirty-Fifth Coastal Engineering in Japan, Japan Soc. Of Civil Engineering*, (January 1988):138–142, 1988.

Lauren Augustin, Jennifer Irish, and Patrick Lynett. Laboratory and numerical studies of wave damping by emergent and near-emergent wetland vegetation. *Coastal Engineering*, pages 332–340, 2009. doi: 10.1016/j.coastaleng.2008.09.004.

Edward B. Barbier. Pricing Nature. *Annual Review of Resource Economics*, 2011. ISSN 1941-1340. doi: 10.1146/annurev-resource-083110-120115.

Christophe Baron-hyppolite. *Simulation of Nearshore Processes and Testing of Implicit and Explicit Vegetation Representations in SWAN*. PhD thesis, Delft University of Technology, 2018.

Christophe Baron-Hyppolite, Christopher H. Lashley, Juan Garzon, Tyler Miesse, Celso Ferreira, and Jeremy D. Bricker. Comparison of implicit and explicit vegetation representations in SWAN hindcasting wave dissipation by coastal wetlands in chesapeake bay. *Geosciences (Switzerland)*, 9(1), 2019. ISSN 20763263. doi: 10.3390/geosciences9010008.

J. A. Battjes. Shoaling of subharmonic gravity waves. *Journal of Geophysical Research*, 109(C2):C02009, 2004. ISSN 0148-0227. doi: 10.1029/2003JC001863. URL http://doi.wiley.com/10.1029/2003JC001863.

J. A. Battjes and J. P. F. M. Janssen. Energy Loss and Set-Up Due to Breaking of Random Waves. In *Coastal Engineering 1978*, pages 569–587, New York, NY, aug 1978. American Society of Civil Engineers. ISBN 9780872621909. doi: 10.1061/9780872621909.034. URL http://ascelibrary.org/doi/10.1061/9780872621909.034.

Alexis Beudin, Tarandeep S. Kalra, Neil K. Ganju, and John C. Warner. Development of a coupled wave-flow-vegetation interaction model. *Computers and Geosciences*, 100(August 2016):76–86, 2017. ISSN 00983004. doi: 10.1016/j.cageo.2016.12.010. URL http://dx.doi.org/10.1016/j.cageo.2016.12.010.

N. Booij, R. C. Ris, and L. H. Holthuijsen. A third-generation wave model for coastal regions 1. Model description and validation. *Journal of Geophysical Research C: Oceans*, 104:7649–7666, 1999.

Bas W. Borsje, Bregje K. van Wesenbeeck, Frank Dekker, Peter Paalvast, Tjeerd J. Bouma, Marieke M. van Katwijk, and Mindert B. de Vries. How ecological engineering can serve in coastal protection, 2011. ISSN 09258574.

T. J. Bouma, M. B. De Vries, E. Low, G. Peralta, I. C. Tánczos, J. Van De Koppel, and P. M.J. Herman. Trade-offs related to ecosystem engineering: A case study on stiffness of emerging macrophytes. *Ecology*, 86(8): 2187–2199, 2005. ISSN 00129658. doi: 10.1890/04-1588.

Tjeerd J. Bouma, Jim van Belzen, Thorsten Balke, Zhenchang Zhu, Laura Airoldi, Andrew J. Blight, Andrew J. Davies, Cristina Galvan, Steve J. Hawkins, Simon P.G. Hoggart, Javier L. Lara, Inigo J. Losada, Maria Maza, Barbara Ondiviela, Martin W. Skov, Elisabeth M. Strain, Richard C. Thompson, Shilun Yang, Barbara Zanuttigh, Liquan Zhang, and Peter M.J. Herman. Identifying knowledge gaps hampering application of intertidal habitats in coastal protection: Opportunities & steps to take. *Coastal Engineering*, 87:147–157, 2014. ISSN 03783839. doi: 10.1016/j.coastaleng.2013.11.014. URL http://dx.doi.org/10.1016/j.coastaleng.2013.11.014.

Kevin Bradley and Chris Houser. Relative velocity of seagrass blades: Implications for wave attenuation in low-energy environments. *Journal of Geophysical Research: Earth Surface*, 114(1):1–13, 2009. ISSN 21699011. doi: 10.1029/2007JF000951.

Bretschneider, Krock, Nakazaki, and Casciano. Roughness of typical Hawaiian terrain for tsunami run-up calculations: A users manual, JKK Look Lab. Rep. Univ. of Hawaii, Honolulu Hawaii. 1986.

L. Cavaleri and P. M. Rizzoli. Wind wave prediction in shallow water: theory and applications. *Journal of Geophysical Research*, 1981. ISSN 01480227. doi: 10.1029/JC086iC11p10961.

Luca Cavallaro, Carlo Lo Re, Giovanni Paratore, Antonino Viviano, and Enrico Foti. Response of Posidonia Oceanica plants to wave motion in shallow-waters - Preliminary experimental results. In *Proceedings of the Coastal Engineering Conference*, pages 1–10, 2010. doi: 10.9753/icce.v32.waves.49.

Charles Feys. *The effect of a shallow vegetated foreshore on infragravity waves.* PhD thesis, Delft University of Technology, 2018.

Qin Chen and Haihong Zhao. Theoretical Models for Wave Energy Dissipation Caused by Vegetation. *Journal of Engineering Mechanics*, 138(2):221–229, feb 2012. ISSN 0733-9399. doi: 10.1061/(ASCE)EM.1943-7889. 0000318. URL http://ascelibrary.org/doi/10.1061/{%}28ASCE{%}29EM.1943-7889.0000318.

J Ian Collins. Prediction of shallow-water spectra. *Journal of Geophysical Research*, 77(15):2693–2707, 1972. ISSN 0148-0227. doi: 10.1029/jc077i015p02693.

Nicholas J. Cooper. Wave Dissipation Across Intertidal Surfaces in the Wash Tidal Inlet, Eastern England. *Journal of Coastal Research*, 211(211):28–40, 2005. ISSN 0749-0208. doi: 10.2112/01002.1.

Robert Costanza, Octavio Pérez-Maqueo, M. Luisa Martinez, Paul Sutton, Sharolyn J. Anderson, and Kenneth Mulder. The value of coastal wetlands for hurricane protection. *Ambio*, 2008. ISSN 00447447. doi: 10.1579/ 0044-7447(2008)37[241:TVOCWF]2.0.CO;2.

University of California Santa Cruz. Research shows mangrove conservation can pay for itself in flood protection, 2020. URL https://phys.org/news/2020-03-mangrove.html.

Robert A. Dalrymple, James T. Kirby, and Paul A. Hwang. Wave Diffraction Due to Areas of Energy Dissipation. *Journal of Waterway, Port, Coastal, and Ocean Engineering*, 110(1):67–79, feb 1984. ISSN 0733-950X. doi: 10.1061/(ASCE)0733-950X(1984)110:1(67). URL http://ascelibrary.org/doi/10.1061/ {%}28ASCE{%}290733-950X{%}281984{%}29110{%}3A1{%}2867{%}29.

A. T. M. de Bakker, M. F. S. Tissier, and B. G. Ruessink. Beach steepness effects on nonlinear infragravity-wave interactions: A numerical study. *Journal of Geophysical Research: Oceans*, 121(1):554–570, jan 2016. ISSN 2169-9275. doi: 10.1002/2015JC011268. URL https://onlinelibrary.wiley.com/doi/abs/10.1002/ 2015JC011268.

Deltares. Delft3D-WAVE. Simulation of short-crested waves with SWAN. User Manual., 2014.

J T Dijkstra. Measurements and modelling of the effects of seagrass meadows on flow and sediment transport in the Bay of l'Ecluse, Dinard, France. pages 5–8, 2009.

Jasper T. Dijkstra. How to account for flexible aquatic vegetation in large-scale morphodynamic models. *Proceedings of the Coastal Engineering Conference*, pages 2820–2831, 2008. ISSN 01613782. doi: 10.1142/ 9789814277426_0233.

Alfonse Dubi and Alf Tørum. Wave Damping by Kelp Vegetation. In *Coastal Engineering 1994*, volume 11, pages 142–156, New York, NY, aug 1995. American Society of Civil Engineers. ISBN 9780784400890. doi: 10.1061/9780784400890.012. URL http://ascelibrary.org/doi/10.1061/9780784400890.012.

Yasser Eldeberky and Jurjen A. Battjes. Spectral modeling of wave breaking: Application to Boussinesq equations. *Journal of Geophysical Research: Oceans*, 101(C1):1253–1264, jan 1996. ISSN 01480227. doi: 10.1029/95JC03219. URL http://doi.wiley.com/10.1029/95JC03219.

Mark S. Fonseca, , and Jennifer Cahalan. A preliminary evaluation of wave attenuation by four species of seagrass. *Estuarine, Coastal and Shelf Science*, 35(6):565–576, 1992. ISSN 02727714. doi: 10.1016/S0272-7714(05)80039-3.

Keryn B. Gedan, Matthew L. Kirwan, Eric Wolanski, Edward B. Barbier, and Brian R. Silliman. The present and future role of coastal wetland vegetation in protecting shorelines: answering recent challenges to the paradigm. *Climatic Change*, 106(1):7–29, may 2011. ISSN 0165-0009. doi: 10.1007/s10584-010-0003-7. URL http://link.springer.com/10.1007/s10584-010-0003-7.

T. C. Granata, T. Serra, J. Colomer, X. Casamitjana, C. M. Duarte, and E. Gacia. Flow and particle distributions in a nearshore seagrass meadow before and after a storm. *Marine Ecology Progress Series*, 218(May 2014): 95–106, 2001. ISSN 01718630. doi: 10.3354/meps218095.

Jennifer C.R. Hansen and Matthew A. Reidenbach. Wave and tidally driven flows in eelgrass beds and their effect on sediment suspension. *Marine Ecology Progress Series*, 448:271–287, 2012. ISSN 01718630. doi: 10.3354/meps09225.

K Hasselmann. On the non-linear energy transfer in a gravity wave spectrum, part 1: general theory. *J. Fluid Mech.*, 12:481–501, 1962.

K. Hasselmann, T. P. Barnett, E. Bouws, H. Carlson, D. E. Cartwright, K. Eake, J. A. Euring, A. Gicnapp, D. E. Hasselmann, P. Kruseman, A. Meerburg, P. Mullen, D. J. Olbers, K. Richren, W. Sell, and H. Walden. Measurements of wind-wave growth and swell decay during the joint North Sea wave project (JONSWAP)., 1973.

S. Hasselmann, K. Hasselmann, J. H. Allender, and T. P. Barnett. Computations and Parameterizations of the Nonlinear Energy Transfer in a Gravity-Wave Specturm. Part II: Parameterizations of the Nonlinear Energy Transfer for Application in Wave Models. *Journal of Physical Oceanography*, 15(11):1378–1391, nov 1985. ISSN 0022-3670. doi: 10.1175/1520-0485(1985)015<1378:CAPOTN>2.0.CO;2. URL http://journals.ametsoc.org/doi/abs/10.1175/1520-0485{%}281985{%}29015{%}3C1378{%}3ACAPOTN{%}3E2.0.CO{%}3B2.

Fei He, Jie Chen, and Changbo Jiang. Surface wave attenuation by vegetation with the stem, root and canopy. *Coastal Engineering*, 152(May):103509, 2019. ISSN 03783839. doi: 10.1016/j.coastaleng.2019.103509. URL https://doi.org/10.1016/j.coastaleng.2019.103509.

Amber Himes-Cornell, Linwood Pendleton, and Perla Atiyah. Valuing ecosystem services from blue forests: A systematic review of the valuation of salt marshes, sea grass beds and mangrove forests. *Ecosystem Services*, 30:36–48, 2018. ISSN 22120416. doi: 10.1016/j.ecoser.2018.01.006. URL https://doi.org/10.1016/j.ecoser.2018.01.006.

L. H. Holthuijsen and T. H. C. Herbers. Statistics of Breaking Waves Observed as Whitecaps in the Open Sea. *Journal of Physical Oceanography*, 16(2):290–297, feb 1986. ISSN 0022-3670. doi: 10.1175/1520-0485(1986)016<0290:SOBWOA>2.0.CO;2. URL http://dx.doi.org/10.1016/j.jsames.2011.03.003{%}0Ahttps://doi.org/10.1016/j.gr.2017.08.001{%}0Ahttp://dx.doi.org/10.1016/j.precamres.2014.12.018{%}0Ahttp://dx.doi.org/10.1016/j.precamres.2011.08.005{%}0Ahttp://dx.doi.org/10.1080/00206814.2014.902757{%}0Ahttp://dx.

Leo H. Holthuijsen. *Waves in oceanic and coastal waters*. 2007. ISBN 9780511618536. doi: 10.1017/CBO9780511618536.

Chris Houser, Sarah Trimble, and Bradley Morales. Influence of Blade Flexibility on the Drag Coefficient of Aquatic Vegetation. *Estuaries and Coasts*, 38(2):569–577, 2014. ISSN 15592731. doi: 10.1007/s12237-014-9840-3.

Zhan Hu, Tomohiro Suzuki, Tjerk Zitman, Wim Uittewaal, and Marcel Stive. Laboratory study on wave dissipation by vegetation in combined current-wave flow. *Coastal Engineering*, 88:131–142, 2014. ISSN 03783839. doi: 10.1016/j.coastaleng.2014.02.009. URL http://dx.doi.org/10.1016/j.coastaleng.2014.02.009.

Zhenhua Huang, Yu Yao, Shawn Y. Sim, and Yao Yao. Interaction of solitary waves with emergent, rigid vegetation. *Ocean Engineering*, 38(10):1080–1088, 2011. ISSN 00298018. doi: 10.1016/j.oceaneng.2011.03.003.

E. Infantes, A. Orfila, G. Simarro, J. Terrados, M. Luhar, and H. Nepf. Effect of a seagrass (Posidonia oceanica) meadow on wave propagation. *Marine Ecology Progress Series*, 456:63–72, 2012. ISSN 01718630. doi: 10. 3354/meps09754.

N. G. Jacobsen, B. C. McFall, and D. A. van der A. A frequency distributed dissipation model for canopies. *Coastal Engineering*, 150(August 2018):135–146, 2019. ISSN 03783839. doi: 10.1016/j.coastaleng.2019.04. 007. URL https://doi.org/10.1016/j.coastaleng.2019.04.007.

Ranjit S. Jadhav, Qin Chen, and Jane M. Smith. Spectral distribution of wave energy dissipation by salt marsh vegetation. *Coastal Engineering*, 77:99–107, 2013. ISSN 03783839. doi: 10.1016/j.coastaleng.2013.02.013.

P. A.E.M. Janssen. Quasi-linear theory of wind-wave generation applied to wave forecasting. *J. PHYSICAL OCEANOGRAPHY*, 1991. ISSN 00223670. doi: 10.1175/1520-0485(1991)021<1631:QLTOWW>2.0.CO;2.

Beena Mary John, I. Mohit Babu, Kiran G Shirlal, and Subba Rao. Experimental Investigations of Wave Height Attenuation by Submerged Artificial Vegetation. volume 81 of *Water Science and Technology Library*, pages 499–509. Springer Singapore, Singapore, 2018. ISBN 978-981-10-5800-4. doi: 10.1007/978-981-10-5801-1_ 34. URL http://link.springer.com/10.1007/978-981-10-5801-1http://link.springer.com/ 10.1007/978-981-10-5801-1{_}34.

Ivar G. Jonsson. Wave boundary layers and friction factors. *Coastal Engineering Proceedings*, 1(10):9, jan 1966. ISSN 2156-1028. doi: 10.9753/icce.v10.9. URL https://icce-ojs-tamu.tdl.org/icce/index. php/icce/article/view/2423.

G. ; Carpenter L.H. Keulegan. Forces on cylinders and spheres in a sinusoidally oscillating fluid. *Journal of Research of the National Bureau of Standards*, 60, 1958. ISSN 15289036. doi: 10.1115/1.3423549.

Paul L Knutson, Robert A Brochu, William N. Seelig, and Margaret Inskeep. Wave damping in Spartinaalterniflora marshes. *Wetlands*, 2(1):87–104, 1982. ISSN 02775212. doi: 10.1007/BF03160548.

Thomas Knutson, Suzana J. Camargo, Johnny C. L. Chan, Kerry Emanuel, Chang-Hoi Ho, James Kossin, Mrutyunjay Mohapatra, Masaki Satoh, Masato Sugi, Kevin Walsh, and Liguang Wu. Tropical Cyclones and Climate Change Assessment: Part I: Detection and Attribution. *Bulletin of the American Meteorological Society*, 100(10):1987–2007, oct 2019. ISSN 0003-0007. doi: 10.1175/BAMS-D-18-0189.1. URL http://journals.ametsoc.org/doi/10.1175/BAMS-D-18-0189.1.

Nobuhisa Kobayashi, Andrew W. Raichle, and Toshiyuki Asano. Wave Attenuation by Vegetation. *Journal of Waterway, Port, Coastal, and Ocean Engineering*, 119(1):30–48, jan 1993. ISSN 0733-950X. doi: 10.1061/(ASCE)0733-950X(1993)119:1(30). URL http://ascelibrary.org/doi/10.1061/ {%}28ASCE{%}290733-950X{%}281993{%}29119{%}3A1{%}2830{%}29.

Theoharris Koftis, Panayotis Prinos, and Vasiliki Stratigaki. Wave damping over artificial Posidonia oceanica meadow: A large-scale experimental study. *Coastal Engineering*, 73:71–83, 2013. ISSN 03783839. doi: 10.1016/j.coastaleng.2012.10.007. URL http://dx.doi.org/10.1016/j.coastaleng.2012.10.007.

G. J. Komen, K. Hasselmann, and K. Hasselmann. On the Existence of a Fully Developed Wind-Sea Spectrum. *Journal of Physical Oceanography*, 14(8):1271–1285, aug 1984. ISSN 0022-3670. doi: 10.1175/1520-0485(1984)014<1271:OTEOAF>2.0.CO;2. URL http://journals.ametsoc.org/doi/abs/ 10.1175/1520-0485{%}281984{%}29014{%}3C1271{%}3AOTEOAF{%}3E2.0.CO{%}3B2.

G. J. Komen, L. Cavaleri, M. Donelan, K. Hasselmann, S. Hasselmann, and P. A. E. M. Janssen. *Dynamics and Modelling of Ocean Waves*. Cambridge University Press, sep 1994. ISBN 9780521577816. doi: 10.1017/CBO9780511628955. URL https://www.cambridge.org/core/product/identifier/ 9780511628955/type/book.

Pushpam Kumar, editor. *The Economics of Ecosystems and Biodiversity Ecological and Economic Foundations*. Earthscan, London and Washington, 2010.

Jiarui Lei and Heidi Nepf. Wave damping by flexible vegetation: Connecting individual blade dynamics to the meadow scale. *Coastal Engineering*, 147(October 2018):138–148, 2019. ISSN 03783839. doi: 10.1016/j.coastaleng.2019.01.008. URL https://doi.org/10.1016/j.coastaleng.2019.01.008.

Sávio Freire Lima, Claudio Freitas Neves, and Nara Maria Luzzi Rosauro. DAMPING OF GRAVITY WAVES BY FIELDS OF FLEXIBLE VEGETATION. In *Coastal Engineering 2006*, pages 491–503. World Scientific Publishing Company, apr 2007. ISBN 978-981-270-636-2. doi: 10.1142/9789812709554_0043. URL https://www.worldscientific.com/doi/abs/10.1142/9789812709554{_}0043http://www.worldscientific.com/doi/abs/10.1142/9789812709554{_}0043.

Iñigo J. Losada, Maria Maza, and Javier L. Lara. A new formulation for vegetation-induced damping under combined waves and currents. *Coastal Engineering*, 107:1–13, 2016. ISSN 03783839. doi: 10.1016/j.coastaleng.2015.09.011. URL http://dx.doi.org/10.1016/j.coastaleng.2015.09.011.

Stig Magnar Løvås and Alf Tørum. Effect of submerged vegetation upon wave damping and run-up on beaches: A case study on Laminaria Hyperborea. In *Coastal Engineering 2000 - Proceedings of the 27th International Conference on Coastal Engineering, ICCE 2000*, volume 276, pages 851–864, 2000. ISBN 0784405492. doi: 10.1061/40549(276)66. URL https://ascelibrary.org/doi/abs/10.1061/40549{%}28276{%}2966.

Charlotta Borell Lövstedt and Magnus Larson. Wave damping in reed: Field measurements and mathematical modeling. *Journal of Hydraulic Engineering*, 136(4):222–233, apr 2010. ISSN 07339429. doi: 10.1061/(ASCE)HY.1943-7900.0000167.

Ryan J. Lowe, Jeffrey R. Koseff, and Stephen G. Monismith. Oscillatory flow through submerged canopies: 1. Velocity structure. *Journal of Geophysical Research C: Oceans*, 110(10):1–17, 2005. ISSN 01480227. doi: 10.1029/2004JC002788.

Ryan J. Lowe, James L. Falter, Jeffrey R. Koseff, Stephen G. Monismith, and Marlin J. Atkinson. Spectral wave flow attenuation within submerged canopies: Implications for wave energy dissipation. *Journal of Geophysical Research: Oceans*, 112(5):1–14, 2007. ISSN 21699291. doi: 10.1029/2006JC003605.

M. Luhar and H. M. Nepf. Wave-induced dynamics of flexible blades. *Journal of Fluids and Structures*, 61:20–41, 2016. ISSN 10958622. doi: 10.1016/j.jfluidstructs.2015.11.007. URL http://dx.doi.org/10.1016/j.jfluidstructs.2015.11.007.

Mitul Luhar and Heidi M. Nepf. Flow-induced reconfiguration of buoyant and flexible aquatic vegetation. *Limnology and Oceanography*, 56(6):2003–2017, nov 2011. ISSN 00243590. doi: 10.4319/lo.2011.56.6.2003. URL http://doi.wiley.com/10.4319/lo.2011.56.6.2003.

Mitul Luhar, Sylvain Coutu, Eduardo Infantes, Samantha Fox, and Heidi Nepf. Wave-induced velocities inside a model seagrass bed. *Journal of Geophysical Research: Oceans*, 115(12):1–15, 2010. ISSN 21699291. doi: 10.1029/2010JC006345.

Gangfeng Ma, James T. Kirby, Shih Feng Su, Jens Figlus, and Fengyan Shi. Numerical study of turbulence and wave damping induced by vegetation canopies. *Coastal Engineering*, 80:68–78, 2013. ISSN 03783839. doi: 10.1016/j.coastaleng.2013.05.007. URL http://dx.doi.org/10.1016/j.coastaleng.2013.05.007.

Ole Secher Madsen, Ying-Keung Poon, and Hans C. Graber. Spectral wave attenuation by bottom friction: Theory. *Coastal Engineering Proceedings*, 1(21):34, jan 1988. ISSN 2156-1028. doi: 10.9753/icce.v21.34. URL https://journals.tdl.org/icce/index.php/icce/article/view/4241.

E. Manca, I. Cáceres, J.M. Alsina, V. Stratigaki, I. Townend, and C.L. Amos. Wave energy and wave-induced flow reduction by full-scale model Posidonia oceanica seagrass. *Continental Shelf Research*, 50-51:100–116, dec 2012. ISSN 02784343. doi: 10.1016/j.csr.2012.10.008. URL https://linkinghub.elsevier.com/retrieve/pii/S0278434312002841.

M. Maza, J. L. Lara, I. J. Losada, B. Ondiviela, J. Trinogga, and T. J. Bouma. Large-scale 3-D experiments of wave and current interaction with real vegetation. Part 2: Experimental analysis. *Coastal Engineering*, 106:73–86, 2015. ISSN 03783839. doi: 10.1016/j.coastaleng.2015.09.010. URL http://dx.doi.org/10.1016/j.coastaleng.2015.09.010.

Maria Maza, Javier L. Lara, and Inigo J. Losada. A coupled model of submerged vegetation under oscillatory flow using Navier-Stokes equations. *Coastal Engineering*, 80:16–34, 2013. ISSN 03783839. doi: 10.1016/j. coastaleng.2013.04.009. URL http://dx.doi.org/10.1016/j.coastaleng.2013.04.009.

Fernando J. Mendez and Inigo J. Losada. An empirical model to estimate the propagation of random breaking and nonbreaking waves over vegetation fields. *Coastal Engineering*, 51(2):103–118, 2004. ISSN 03783839. doi: 10.1016/j.coastaleng.2003.11.003.

I. Möller. Quantifying saltmarsh vegetation and its effect on wave height dissipation: Results from a UK East coast saltmarsh. *Estuarine, Coastal and Shelf Science*, 69(3-4):337–351, 2006. ISSN 02727714. doi: 10.1016/j.ecss.2006.05.003.

I Möller and T Spencer. Wave dissipation over macro-tidal saltmarshes: Effects of marsh edge typology and vegetation change. *Journal of Coastal Research*, 36(May 2014):506–521, mar 2002. ISSN 0749-0208. doi: 10. 2112/1551-5036-36.sp1.506. URL http://www.bioone.org/doi/10.2112/1551-5036-36.sp1.506.

I. Möller, T. Spencer, J. R. French, D. J. Leggett, and M. Dixon. Wave transformation over salt marshes: A field and numerical modelling study from north Norfolk, England. *Estuarine, Coastal and Shelf Science*, 49(3): 411–426, 1999. ISSN 02727714. doi: 10.1006/ecss.1999.0509.

Iris Möller, Matthias Kudella, Franziska Rupprecht, Tom Spencer, Maike Paul, Bregje K. Van Wesenbeeck, Guido Wolters, Kai Jensen, Tjeerd J. Bouma, Martin Miranda-Lange, and Stefan Schimmels. Wave attenuation over coastal salt marshes under storm surge conditions. *Nature Geoscience*, 7(10):727–731, 2014. ISSN 17520908. doi: 10.1038/NGEO2251.

Julia C Mullarney, Stephen M Henderson, Johan A.H. Reyns, Benjamin K Norris, and Karin R Bryan. Spatially varying drag within a wave-exposed mangrove forest and on the adjacent tidal flat. *Continental Shelf Research*, 147(October 2016):102–113, 2017. ISSN 18736955. doi: 10.1016/j.csr.2017.06.019. URL http://dx.doi.org/10.1016/j.csr.2017.06.019.

Heidi M. Nepf. Flow and Transport in Regions with Aquatic Vegetation. *Annual Review of Fluid Mechanics*, 44(1):123–142, 2012. ISSN 0066-4189. doi: 10.1146/annurev-fluid-120710-101048.

Yan Ni. *Drag forces on vegetation due to waves and currents.* PhD thesis, Delft University of Technology, 2014.

Daniel J. Nowacki, Alexis Beudin, and Neil K. Ganju. Spectral wave dissipation by submerged aquatic vegetation in a back-barrier estuary. *Limnology and Oceanography*, 62(2):736–753, 2017. ISSN 19395590. doi: 10.1002/lno.10456.

Okey Nwogu. Nonlinear Evolution of Directional Wave Spectra in Shallow Water. In *Coastal Engineering 1994*, pages 467–481, New York, NY, aug 1995. American Society of Civil Engineers. ISBN 9780784400890. doi: 10.1061/9780784400890.036. URL http://ascelibrary.org/doi/10.1061/9780784400890.036.

Y. Ozeren, D. G. Wren, and W. Wu. Experimental investigation of wave attenuation through model and live vegetation. *Journal of Waterway, Port, Coastal and Ocean Engineering*, 140(5):1–12, 2014. ISSN 0733950X. doi: 10.1061/(ASCE)WW.1943-5460.0000251.

M. Paul and C. L. Amos. Spatial and seasonal variation in wave attenuation over Zostera noltii. *Journal of Geophysical Research: Oceans*, 116(8):1–16, 2011. ISSN 21699291. doi: 10.1029/2010JC006797.

M. Paul, T. J. Bouma, and C. L. Amos. Wave attenuation by submerged vegetation: Combining the effect of organism traits and tidal current. *Marine Ecology Progress Series*, 444(January):31–41, 2012. ISSN 01718630. doi: 10.3354/meps09489.

Willemijntje E. Penning, Reinout De Oude, and Arthur Mynett. The Effects of Macrophyte Morphology and Patch Density on Wave Attenuation. *7th ISE and 8th HIC*, (January), 2009.

Vo Luong Hong Phuoc and Stanisław R. Massel. Experiments on wave motion and suspended sediment concentration at Nang Hai, Can Gio mangrove forest, Southern Vietnam. *Oceanologia*, 48(1):23–40, 2006. ISSN 00783234.

Timor M.I. Post. *Assessment of wave run-up reduction by salt marshes.* PhD thesis, University of Twente, 2015.

S Quartel, A. Kroon, P. G.E.F. Augustinus, P. Van Santen, and N. H. Tri. Wave attenuation in coastal mangroves in the Red River Delta, Vietnam. *Journal of Asian Earth Sciences*, 29(4):576–584, feb 2007. ISSN 13679120. doi: 10.1016/j.jseaes.2006.05.008. URL https://linkinghub.elsevier.com/retrieve/pii/S1367912006001672.

Kassi C. Riffe, Stephen M. Henderson, and Julia C. Mullarney. Wave dissipation by flexible vegetation. *Geophysical Research Letters*, 38(18):1–5, 2011. ISSN 00948276. doi: 10.1029/2011GL048773.

F. Rupprecht, I. Möller, M. Paul, M. Kudella, T. Spencer, B.K. van Wesenbeeck, G. Wolters, K. Jensen, T.J. Bouma, M. Miranda-Lange, and S. Schimmels. Vegetation-wave interactions in salt marshes under storm surge conditions. *Ecological Engineering*, 100:301–315, mar 2017. ISSN 09258574. doi: 10.1016/j.ecoleng.2016.12.030. URL http://dx.doi.org/10.1016/j.ecoleng.2016.12.030https://linkinghub.elsevier.com/retrieve/pii/S0925857416307443.

Arthur James Samiksha, Vethamony, Bhaskaran, Pednekar, Jishad. Attenuation of Wave Energy Due to Mangrove Vegetation off Mumbai, India. *Energies*, (2019), 2019. doi: 10.3390/en12224286.

José Francisco Sánchez-González, Virginia Sánchez-Rojas, and Constantine Demetrius Memos. Wave attenuation due to Posidonia oceanica meadows. *Journal of Hydraulic Research*, 49(4):503–514, 2011. ISSN 00221686. doi: 10.1080/00221686.2011.552464.

Ana Maria Serrano. *Wave energy dissipation due to posidonia oceanica in the Mediterranean Sea*. PhD thesis, Delft University of Technology, 2016.

Grant Alexander Smith, Alexander V. Babanin, Peter Riedel, I. R. Young, Stephen Oliver, and Graeme Hubbert. Introduction of a new friction routine into the SWAN model that evaluates roughness due to bedform and sediment size changes. *Coastal Engineering*, 58(4):317–326, 2011. ISSN 03783839. doi: 10.1016/j.coastaleng.2010.11.006. URL http://dx.doi.org/10.1016/j.coastaleng.2010.11.006.

Henk Steetzel, Jacco Groeneweg, and Vincent Vuik. Effectiviteit Voorlanden HR Onderzoeksrapportage Fase C. Technical report, POV Waddenzeedijken, 2018.

Vasiliki Stratigaki, Eleonora Manca, Panayotis Prinos, Inigo J. Losada, Javier L. Lara, Mauro Sclavo, Carl L. Amos, Iván Cáceres, and Agustín Sánchez-Arcilla. Large-scale experiments on wave propagation over Posidonia oceanica. *Journal of Hydraulic Research*, 2011. ISSN 00221686. doi: 10.1080/00221686.2011.583388.

Tomohiro Suzuki, Marcel Zijlema, Bastiaan Burger, Martijn C. Meijer, and Siddharth Narayan. Wave dissipation by vegetation with layer schematization in SWAN. *Coastal Engineering*, 59(1):64–71, 2011. ISSN 03783839. doi: 10.1016/j.coastaleng.2011.07.006. URL http://dx.doi.org/10.1016/j.coastaleng.2011.07.006.

S. Temmerman, T. J. Bouma, G. Govers, Z. B. Wang, M. B. De Vries, and P. M J Herman. Impact of vegetation on flow routing and sedimentation patterns: Three-dimensional modeling for a tidal marsh. *Journal of Geophysical Research: Earth Surface*, 110(4):1–18, 2005. ISSN 21699011. doi: 10.1029/2005JF000301.

The SWAN team. SWAN user manual version 41.31. Technical report, Delft University of Technology, Delft, 2019a.

The SWAN team. Implementation Manual SWAN Cycle III version 40.31. Technical report, Delft University of Technology, Delft, 2019b. URL http://swanmodel.sourceforge.net/.

The SWAN team. Programming Rules SWAN Version 40.31. Technical report, Delft University of Technology, Delft, 2019c. URL DelftUniversityofTechnology.

The SWAN team. Scientific and technical documentation version 41.31. Technical report, Delft University of Technology, Delft, 2019d. URL http://swanmodel.sourceforge.net/.

Paul Tschirky, Kevin Hall, and David Turcke. Wave Attenuation by Emergent Wetland Vegetation. In *Coastal Engineering 2000*, volume 276, pages 865–877, Reston, VA, mar 2001. American Society of Civil Engineers. ISBN 9780784405499. doi: 10.1061/40549(276)67. URL http://ascelibrary.org/doi/10.1061/40549{%}28276{%}2967.

A. A. van Rooijen, R. J. Lowe, M. Ghisalberti, J. Hansen, R. T. McCall, and A. R. van Dongeren. Physical and numerical modelling of wave transformation through a coastal canopy. *Proceedings of the 20th Australasian Fluid Mechanics Conference, AFMC 2016*, (December):5–8, 2016a.

A. A. van Rooijen, R. T. McCall, J. S. M. van Thiel de Vries, A. R. van Dongeren, A. J. H. M. Reniers, and J. A. Roelvink. Modeling the effect of wave-vegetation interaction on wave setup. *Journal of Geophysical Research: Oceans*, 121(6):4341–4359, jun 2016b. ISSN 21699275. doi: 10.1002/2015JC011392. URL http://doi.wiley.com/10.1002/2015JC011392.

Arnold van Rooijen, Ryan Lowe, Marco Ghisalberti, Mario Conde-Frias, and Liming Tan. Predicting Current-Induced Drag in Emergent and Submerged Aquatic Vegetation Canopies. *Frontiers in Marine Science*, 5 (DEC):1–14, dec 2018. ISSN 2296-7745. doi: 10.3389/fmars.2018.00449. URL https://www.frontiersin.org/article/10.3389/fmars.2018.00449/full.

Arnold van Rooijen, Ryan Lowe, Dirk P. Rijnsdorp, Marco Ghisalberti, Niels G. Jacobsen, and Robert McCall. Wave-Driven Mean Flow Dynamics in Submerged Canopies. *Journal of Geophysical Research: Oceans*, 125 (3):0–3, mar 2020. ISSN 2169-9275. doi: 10.1029/2019JC015935. URL https://onlinelibrary.wiley.com/doi/abs/10.1029/2019JC015935.

V.T.M. van Zelst. *Global flood hazard reduction by foreshore vegetation.* PhD thesis, Delft University of Technology, 2018.

V. Vuik, S. N. Jonkman, B. W. Borsje, and T. Suzuki. Nature-based flood protection: The efficiency of vegetated foreshores for reducing wave loads on coastal dikes. *Coastal Engineering*, 116:42–56, 2016. ISSN 03783839. doi: 10.1016/j.coastaleng.2016.06.001.

Vincent Vuik, Hannah Y. Suh Heo, Zhenchang Zhu, Bas W. Borsje, and Sebastiaan N. Jonkman. Stem breakage of salt marsh vegetation under wave forcing: A field and model study. *Estuarine, Coastal and Shelf Science*, 200:41–58, 2018a. ISSN 02727714. doi: 10.1016/j.ecss.2017.09.028. URL https://doi.org/10.1016/j.ecss.2017.09.028.

Vincent Vuik, Saskia van Vuren, Bas W. Borsje, Bregje K. van Wesenbeeck, and Sebastiaan N. Jonkman. Assessing safety of nature-based flood defenses: Dealing with extremes and uncertainties. *Coastal Engineering*, 139(April):47–64, 2018b. ISSN 03783839. doi: 10.1016/j.coastaleng.2018.05.002. URL https://doi.org/10.1016/j.coastaleng.2018.05.002.

Vincent Vuik, Bas W. Borsje, Pim W.J.M. Willemsen, and Sebastiaan N. Jonkman. Salt marshes for flood risk reduction: Quantifying long-term effectiveness and life-cycle costs. *Ocean and Coastal Management*, 171 (February):96–110, 2019. ISSN 09645691. doi: 10.1016/j.ocecoaman.2019.01.010. URL https://doi.org/10.1016/j.ocecoaman.2019.01.010.

WAMDI Group. The WAM Model—A Third Generation Ocean Wave Prediction Model. *Journal of Physical Oceanography*, 18(12):1775–1810, dec 1988. ISSN 0022-3670. doi: 10.1175/1520-0485(1988)018<1775:TWMTGO>2.0.CO;2. URL http://journals.ametsoc.org/doi/abs/10.1175/1520-0485{%}281988{%}29018{%}3C1775{%}3ATWMTGO{%}3E2.0.CO{%}3B2.

Ty V. Wamsley, Mary A. Cialone, Jane M. Smith, John H. Atkinson, and Julie D. Rosati. The potential of wetlands in reducing storm surge. *Ocean Engineering*, 37(1):59–68, jan 2010. ISSN 00298018. doi: 10.1016/j.oceaneng.2009.07.018. URL https://linkinghub.elsevier.com/retrieve/pii/S002980180900184X.

M. Waycott, C. M. Duarte, T. J. B. Carruthers, R. J. Orth, W. C. Dennison, S. Olyarnik, A. Calladine, J. W. Fourqurean, K. L. Heck, A. R. Hughes, G. A. Kendrick, W. J. Kenworthy, F. T. Short, and S. L. Williams. Accelerating loss of seagrasses across the globe threatens coastal ecosystems. *Proceedings of the National Academy of Sciences*, 106(30):12377–12381, jul 2009. ISSN 0027-8424. doi: 10.1073/pnas.0905620106. URL http://www.pnas.org/cgi/doi/10.1073/pnas.0905620106.

Christopher J. Wayne. The effects of sea and marsh grass on wave energy. *Coastal Research*, 4(7):6–8, 1976.

Jin Wu. Wind-stress coefficients over sea surface from breeze to hurricane. *Journal of Geophysical Research*, 87(C12):9704, 1982. ISSN 0148-0227. doi: 10.1029/JC087iC12p09704. URL http://doi.wiley.com/10.1029/JC087iC12p09704.

Wei-Cheng Wu and Daniel T. Cox. Effects of wave steepness and relative water depth on wave attenuation by emergent vegetation. *Estuarine, Coastal and Shelf Science*, 164:443–450, oct 2015. ISSN 02727714. doi: 10.1016/j.ecss.2015.08.009. URL http://dx.doi.org/10.1016/j.ecss.2015.08.009https:// linkinghub.elsevier.com/retrieve/pii/S0272771415300664.

Wei Cheng Wu, Gangfeng Ma, and Daniel T. Cox. Modeling wave attenuation induced by the vertical density variations of vegetation. *Coastal Engineering*, 112:17–27, 2016. ISSN 03783839. doi: 10.1016/j.coastaleng. 2016.02.004. URL http://dx.doi.org/10.1016/j.coastaleng.2016.02.004.

WWF. Planting hope: Seagrass. URL https://www.wwf.org.uk/what-we-do/ planting-hope-how-seagrass-can-tackle-climate-change.

S L Yang, B W Shi, T J Bouma, T Ysebaert, and X X Luo. Wave Attenuation at a Salt Marsh Margin: A Case Study of an Exposed Coast on the Yangtze Estuary. *Estuaries and Coasts*, 35(1):169–182, 2012. ISSN 15592723. doi: 10.1007/s12237-011-9424-4.

Zegao Yin, Xiaoyu Yang, Yuanzhao Xu, Meiling Ding, and Haixiang Lu. Experimental wave attenuation study over flexible plants on a submerged slope. *Journal of Ocean University of China*, 16(6):1009–1017, 2017. ISSN 19935021. doi: 10.1007/s11802-017-3298-4.

Ling Zhu and Qin Chen. Attenuation of nonlinear waves by rigid vegetation: Comparison of different wave theories. *Journal of Waterway, Port, Coastal and Ocean Engineering*, 143(5):1–12, 2017. ISSN 0733950X. doi: 10.1061/(ASCE)WW.1943-5460.0000415.

Ling Zhu and Qin Chen. Effects of triad interactions on wave attenuation by vegetation. *Journal of Engineering Mechanics*, 143(9):1–13, 2018. ISSN 07339399. doi: 10.1061/(ASCE)EM.1943-7889.0001328.

Longhuan Zhu, Kimberly Huguenard, Qing-ping Zou, David W. Fredriksson, and Dongmei Xie. Aqua-culture farms as nature-based coastal protection: Random wave attenuation by suspended and sub-merged canopies. *Coastal Engineering*, 160(October 2019):103737, sep 2020a. ISSN 03783839. doi: 10. 1016/j.coastaleng.2020.103737. URL https://doi.org/10.1016/j.coastaleng.2020.103737https: //linkinghub.elsevier.com/retrieve/pii/S0378383919303990.

Zhenchang Zhu, Vincent Vuik, Paul J. Visser, Tim Soens, Bregje van Wesenbeeck, Johan van de Koppel, Se-bastiaan N. Jonkman, Stijn Temmerman, and Tjeerd J. Bouma. Historic storms and the hidden value of coastal wetlands for nature-based flood defence. *Nature Sustainability*, jun 2020b. ISSN 2398-9629. doi: 10.1038/s41893-020-0556-z. URL http://www.nature.com/articles/s41893-020-0556-z.